ABSTRACT

FULTON, CHARLES CLIFTON. Spectroscopic Study of the Interface Chemical and Electronic Properties of High-κ Gate Stacks. (Under the direction of Robert J. Nemanich and Gerald Lucovsky).

X-ray and ultraviolet photoemission spectroscopy has been combined with in-situ deposition to study the interface chemistry and electronic structure of potential high-κ gate stack materials. In addressing the interface stability of ZrO_2 with respect to a Si substrate three issues are considered: 1) the development of the band offsets and electronic structure during the low temperature (T<300°C) growth processes, 2) variations in the band structure as effected by process conditions and annealing (T<700°C) and 3) the interface stability of Zr oxide films at high temperatures (T>700°C). To further explore low temperature effects, titanium, zirconium and hafnium oxides were deposited on ultra-thin (~0.5 nm) SiO_2 buffer layers and metastable states have been identified which give rise to large changes in the band alignments with respect to the Si substrate. Also discussed is the band edge electronic structure of 1) nanocrystalline Zr, Hf and complex oxide high-κ dielectrics, and 2) non-crystalline Zr and Hf silicates and Si oxynitride alloys. Three issues are highlighted: Jahn-Teller term-splittings that remove band edge d-state degeneracies in nanocrystalline films, intrinsic bonding defects in ZrO_2 and HfO_2, and chemical phase separation and crystallinity in Zr and Hf silicate and Si oxynitride alloys. Finally, photoemission spectroscopy has been used to characterize a candidate gate stack including electron affinities and work functions, valence band maxima, band bending in the Si and fields in the oxide layers. The band offsets are constructed and the deviation from the Schottky-Mott (or electron affinity) model at each interface is discussed in terms of interface bonding and the resultant charge transfer.

SPECTROSCOPIC STUDY OF THE INTERFACE CHEMICAL AND ELECTRONIC PROPERTIES OF HIGH-K GATE STACKS

by

CHARLES CLIFTON FULTON

A dissertation submitted to the Graduate Faculty of
North Carolina State University in partial fulfillment of
the requirements for the degree of Doctor of Philosophy

DEPARTMENT OF MATERIALS SCIENCE AND ENGINEERING

Raleigh, NC

2005

APPROVED BY:

R.J. Nemanich, Advisory Committee Chair

J-P. Maria, Co-Chair

G. Lucovsky, Minor Representative

A.I. Kingon

DEDICATION

To the wrench and the bookshelf…

your sacrifices have saved countless lives

BIOGRAPHY

West Philadelphia born and raised, on the playground is where I spent most of my days… no wait, that's someone else. Charles Clifton Fulton was born to April Ray Judy Berry McFarland Fulton Spier and Darrell E. Fulton. A short time thereafter and more importantly, Charlie (as the author will henceforth be referred to) was raised by Dianna Kay Fulton and Darrell in the small, and sometimes trying, town of South Charleston, Ohio. He spent his formative years toying with the omnipresent dimwits that seem to be fill many such towns, particularly in Ohio it seems, but anecdotal evidence suggests they occur in other places as well. Interaction with the small-minded local educators, each on their respective power trips, proved to be the most enlightening experience of all. In one amusing instance, Charlie was accused of being a "133t h4x0r" and was suspended for a few days from high-school. This effectively ended his perfect attendance (3 years and some change of it, no less), and after that time he was known to make liberal use of the so called "mental health" days. Processing of this administrative action utilized the only remaining administrative action form, and Charlie was thus asked to use his newly earned vacation time to format a new one. No one took the event terribly seriously except perhaps the computer instructor/IT person who felt it a blow to her pride that she had been h4x0r3d by a punk kid. In all reality this was not a case of h4x0r1ng at all but was really just a case of an offhanded guess at what turned out to be the world's stupidest password. It was just politics. No on takes politics seriously. It was also a good opportunity to make friends with the superintendent, who is very good at politics.

Off to Ohio University and the Honors Tutorial Program in Physics he went, where all of the core degree classes were taught one-on-one with professors. This was a fruitful environment for learning and bolstered the sense of working *with* professors rather than *for* them. He spent two summers working at the Air Force Research Laboratory, learning much about the ways of the world, or at least about the ways of the bureaucracy – little gems such as putting a government inventory number on hand held equipment. This sounds like a sufficiently mundane action, but the literal implications are that in order to remove a hand held DMM from its assigned room, one must file the appropriate request form and await approval to do one's job.

Later in his undergraduate career, he took a summer position with the National Radio Astronomy Observatory that required him to construct a small, educational radio telescope. While there, he learned of a tradition of summer pranks and of one particular prank wherein a student placed a classified ad claiming that the Very Large Array (Soccoro, NM) was for sale. Not to be outdone, he scaled the 300' Green Bank Telescope (Green Bank, WV) and anointed it with a jolly roger. Arrr, matey, pirate astronomy.

Then it was off to graduate school. On the urging of his undergraduate advisors, he visited NC State and also applied to Princeton. He was accepted at both and there were several reasons for choosing the place he did. The pay was about the same, but it goes a lot further in Raleigh than in Princeton. North Carolina State University offered a very strong engineering program, and besides, it is not possible to make a left turn in New Jersey even though the people often seem to be a bit left of center. Ultimately it was a wise choice, given the poor fit of the graduate physics program and a subsequent defection to the Materials Science and Engineering Department which likely would not have been so simple at

Princeton. He went to Hawaii for a conference, came back married, got a Masters (Aug 2004), is currently penning his dissertation hoping to escape this place for sunnier, though perhaps not greener, pastures in Arizona.

TABLE OF CONTENTS

List of Tables ..... **x**

List of Figures ..... **xi**

1. Introduction to High-κ Gate Stacks: Device Scaling and Material Considerations **1**

1.1 Introduction 2

1.2 Device scaling and leakage current 2

1.3 Issues for advanced gate dielectrics 4

1.3.1 Si – dielectric interface 4

1.3.2 Permittivity, barrier heights and bandgaps 4

1.3.3 Thermodynamic stability 5

1.3.4 CMOS process considerations 5

1.4 Gate electrodes 6

1.5 Thesis approach 7

Chapter 2 8

Chapter 3 8

Chapter 4 9

Chapter 5 9

Chapter 6 10

1.6 References 11

2. Interface Instabilities and Electronic Properties of ZrO_2 on Silicon (100) **12**

2.1 Abstract 13

2.2 Introduction 14

2.3 Experiment 15

2.4 Results 18
2.4.1 Low temperature Zr oxide formation 18
2.4.2 High temperature instability 20
2.4.3 Stability with alternate buffer layers 21
2.4.4 Low temperature instability 24
2.5 Discussion 24
2.5.1 Integrity of the SiO_2 buffer layer 24
2.5.2 High temperature instability 25
2.5.3 Low temperature instability 27
2.6 Conclusions 28
2.7 Acknowledgements 29
2.8 References 30
3. Process Dependent Band Structure Changes of Transition-metal (Ti, Zr, Hf) Oxides on Si (100) 46
3.1 Abstract 47
3.2 Introduction 48
3.3 Experiment 49
3.4 Results 50
3.5 Discussion 51
3.6 Conclusions 53
3.7 Acknowledgements 54
3.8 References 55

4. Band Edge Electronic Structure of Transition Metal / Rare Earth Oxide Dielectrics..... 61

4.1 Abstract 62

4.2 Introduction 63

4.3 Experimental methods 64

4.4 Experimental results and discussion 65

4.4.1 TM elemental oxides 65

4.4.2 TM/RE complex oxides 70

4.4.3 Intrinsic defect states 73

4.4.4 Zr silicate and oxynitride alloys 76

4.5 Conclusions 80

4.6 Acknowledgements 82

4.7 References 83

5. Electronic Properties of the $Zr–ZrO_2–SiO_2–Si(100)$ gate stack structure..... 101

5.1 Abstract 102

5.2 Introduction 103

5.3 Experiment 106

5.4 Results 111

5.4.1 0.5 nm SiO_2 112

5.4.2 1.0 nm ZrO_2 112

5.4.3 1.0 nm Zr metal 113

5.5 Discussion 114

5.5.1 0.5 nm SiO_2 114

5.5.2 1.0 nm ZrO_2 115

5.5.3 1.0 nm Zr metal 116

5.5.4 Interface Dipoles and Band Alignment 118

5.6 Conclusions 122

5.7 Acknowledgements 123

5.8 References 124

6. Summary and Future Work 142

6.1 Summary 143

6.2 Future Work 146

List of Tables

Table 2.1: Tabulated XPS peak positions and UPS valence band data in binding energy relative to the Si E_F for ZrO_2 deposited on a 0.5 nm SiO_2 buffer layer. The valence band offset (VBO) includes band bending and the conduction band offset (CBO) includes the bandgap (9.0 eV for SiO_2 and 5.8 eV for ZrO_2). 32

Table 2.2: Tabulated XPS peak positions and UPS valence band data in binding energy relative to the Si E_F for ZrO_2 deposited on a ~30 nm SiO_2 buffer layer. 33

Table 2.3: Tabulated XPS peak positions and UPS valence band data in binding energy relative to the Si E_F for ZrO_2 deposited on a ~1 nm Si_3N_4 buffer layer. The VBO includes band bending and the CBO is not given as the bandgap values needed to calculate the CBO are not well defined in the presence of excess Si..... 34

Table 2.4: Chemical reduction of $ZrSiO_4$ and ZrO_2 involving $SiO_{(g)}$ and $ZrO_{(g)}$ formation. The equilibrium pressures of $SiO_{(g)}$ and $ZrO_{(g)}$ are set at 0.01 Torr at all temperatures, and that $\Delta G_i^o = \Delta G_f^o + RT \ln P_i$ is used for the gaseous species. Values for ΔG are given in kcal/mol. for ZrO2 and ZrSiO4 decomposition.[5] 35

Table 5.1: Tabulated x-ray and ultraviolet photoemission features after each deposition step. Values are in binding energy (eV) relative to the Si E_F with an error of ±0.1 eV. 126

Table 5.2: Tabulated electronic structure for the Si–SiO_2–ZrO_2–Zr system including band bending, internal potentials, VBOs, electron affinities and interface dipoles. The VBO includes band bending and internal fields. The conduction band offset (CBO) assumes a bandgap (9.0 eV for SiO_2 and 5.7 eV for ZrO_2). 127

Table 5.3: Tabulated values of the bandgap, slope parameter φ_{VBO}, the branch point energy Φ_{bp}, the Miedema electronegativity X, the optical dielectric constant ε_∞, and the calculated slope parameter S_X. 128

Table 5.4: Calculated barrier heights from the IFIGS model, the electron affinity (Schottky–Mott) model and a comparison with measured values. CBO values presume bandgaps as listed in Table 3. 129

List of Figures

Figure 2.1: XPS core level spectra of the O 1s transition for various thicknesses of the Zr oxide film on a 1.0 nm SiO_2 buffer layer. 37

Figure 2.2: XPS core level spectra of the Si 2p transition for various thicknesses of the Zr oxide film on a 1.0 nm SiO_2 buffer layer. 38

Figure 2.3: XPS core level spectra of the Si 2p transition for various thicknesses of the Zr oxide film on a 1.0 nm SiO_2 buffer layer (note the plot order is reversed with respect to Fig 1,2 for clarity). 39

Figure 2.4: UPS valence band spectra for various thicknesses of the Zr oxide film on a 1.0 nm SiO_2 buffer layer. 40

Figure 2.5: UPS valence band spectra for ZrO_2 on a thin SiO_2 buffer layer after different annealing temperatures. The shift from the as-grown 3.5 nm Zr oxide is large (> 2eV) when annealed to 600°C. There is a smaller shift to lover binding energy as the film is annealed to higher temperature (750°C). After the 900°C anneal emission is observed near E_F, indicating the film has a metallic like character. The relative intensity of each spectrum has been normalized for clarity. 41

Figure 2.6: XPS core level spectra of the (a) O 1s and the (b) Si 2p transitions for the as-grown 3.5 nm Zr oxide film and after 600, 750 and 900°C *in-situ* anneal. The O 1s peak has a large shift when annealed at 600°C then disappears after annealing at 900°C. The oxide related Si 2p (~102—103 eV) also shows a sizable shift when annealed to 600°C and also disappears after annealing to 900°C. The Si 2p bulk peak (~99 eV) becomes much more intense after the 900°C anneal. 42

Figure 2.7: XPS core level spectra of the (a) O 1s and the (b) oxide related Si 2p transitions from 3.0 nm Zr oxide deposited on 30 nm SiO_2. 43

Figure 2.8: XPS core level spectra of the (a) O 1s and the (b) Si 2p transitions from 3.0 nm Zr oxide deposited on 30 nm SiO_2 with a 2 nm Si cap. The oxide related features are hardly evident after the 900°C anneal. 44

Figure 2.9: Schematic diagram of the valence and conduction bands for the (a) as-grown and the (b) annealed state of the TM oxide film on a thin SiO_2 buffer layer. The valence band offset (ΔE_V) can change by up to ~2.5 eV with annealing. The depictions are (a) before *in-situ* annealing where excess oxygen near the ZrO_2–SiO_2 interface attracts electrons from the substrate, resulting in a potential across the SiO_2 buffer layer and (b) after *in-situ* annealing where the oxygen has diffused to vacuum, reducing the interface electronic states and the bands become flat. 45

Figure 3.1: UPS valence band spectra for Ti, Zr and Hf oxides with an SiO_2 buffer layer on Si. Solid lines indicate the as-grown state; dotted lines indicate the annealed state. 57

Figure 3.2: UPS spectra of a ZrO_2 film with an SiO_2 buffer layer on Si. The spectra were obtained a) as grown, b) 500°C anneal, c) re-oxidized and d) second 500°C anneal. 58

Figure 3.3: XPS O 1s core level of an as-grown and annealed ZrO_2 film with an SiO_2 buffer on Si. The larger peaks are associated with the ZrO_2 layer and the smaller peaks with the buried SiO_2 buffer layer. The shifts on annealing (arrows) are larger for the ZrO_2 than the SiO_2 buffer layer. 59

Figure 3.4: Schematic diagram of the as-grown (a) and annealed (b) state: (a) excess oxygen near the Tm oxide–SiO_2 interface attracts electrons from the substrate, resulting in a potential across the SiO_2 buffer layer; (b) the oxygen diffuses to vacuum, there are no interface electronic states and the bands become flat. The valence band offset (ΔE_V) can change by up to 2.0 eV with annealing. 60

Figure 4.1: O K_1 edge spectrum and derivative for noncrystalline Zr silicate 30% alloy as-deposited. (b) O K_1 edges for 60% alloy, as-deposited and after a 900°C anneal which results in chemical phase separation into SiO_2 and nano-crystalline ZrO_2. 86

Figure 4.2: X-ray absorption near edge spectra for TiO_2: (a) the Ti $L_{2,3}$ edge, (b) the L_3 edge spectrum, (c) the O K_1 edge spectrum. 87

Figure 4.3: Band edge spectra for TiO_2: (a) the imaginary part of the complex constant, ε_2, where $\varepsilon_c = \varepsilon_1 + i\varepsilon_2$, (b) the absorption constant, α, (c) comparison between the five d-state features in the L_3 edge, and in ε_2, and (d) the photoconductivity response. 88

Figure 4.4: X-ray absorption near edge spectra for ZrO_2: (a) the Zr $M_{2,3}$ spectra, and (b) the O K_1 edge spectrum. 89

Figure 4.5: Band edge spectra for ZrO_2: (a) the imaginary part of the complex constant, ε_2, where $\varepsilon_c = \varepsilon_1 + i\varepsilon_2$, (b) the absorption constant, α, and (c) the photoconductivity response. 90

Figure 4.6: X-ray absorption near edge spectra for HfO_2: (a) the O K_1 edge spectrum, (b) the imaginary part of the complex constant, ε_2, where $\varepsilon_c = \varepsilon_1 + i\varepsilon_2$, (c) the absorption constant, α, and (d) the photoconductivity response. 91

Figure 4.7: O K_1 edge spectra for: (a) ZrO_2, (b) and (c) ZrO_2 alloyed with 18.5 and 27.5% Y_2O_3, and (d) and (e) cubic and bixbyite Y_2O_3. 92

Figure 4.8: $M_{2,3}$ spectra for (a) ZrO_2, (b) and (c) alloys of ZrO_2 with 18.5 and 27.5% Y_2O_3, and (d) bixbyite Y_2O_3. Features marked by dashed lines are transitions to Y and Zr 4s states. All other features terminate in 3d states. 93

Figure 4.9: X-ray absorption near edge spectra for Zr and Hf titanate alloys: O K_1 edge spectra of (a) a $(HfO_2)_{0.5}(TiO_2)_{0.5}$ alloy and (b) the stoichiometric compound $ZrTiO_4$ or equivalently $(ZrO_2)_{0.5}(TiO_2)_{0.5}$. 94

Figure 4.10: O K_1 spectra: (a) $LaAlO_3$, and $LaScO_3$: (b) O K_1 as-deposited and (b) OK_1 annealed at 1000°C, (d) Sc L_3 spectra as-deposited, and (e) Sc L_3 spectra annealed at 1000°C. 95

Figure 4.11: Photoconductive response spectra for: (a) $LaAlO_3$, and (b) $LaScO_3$. 96

Figure 4.12: O K_1 spectra, with expanded view of the leading edge of these spectra: (a) ZrO_2 and (b) an alloy of ZrO_2 with 18.5 Y_2O_3, and (c) the absorption edge spectrum, α, for a bulk cubic zirconia crystal $[(ZrO_2)_{0.905}(Y_2O_3)_{0.095}]$. 97

Figure 4.13: An energy level diagram that includes a Si substrate, a thin SiO_2 interfacial oxide, and a thicker film of either ZrO_2 and HfO_2. Defect state energies within the band gap of ZrO_2 are indicated for a grain boundary defect, an O-atom vacancy, and a H-defect. 98

Figure 4.14: Fourier transform infra red absorbance spectra for Zr silicate alloys with ZrO_2 fractions, x, equal to (a) 0.23 and (b) 0.5. 99

Figure 4.15: FTIR results for two pseudo-ternary $Zr(Hf)O_2$-SiO_2-Si_3N_4 alloys in (a) and (c), and include derivative XPS O 1s core level spectra for the same alloys in (b) and (d). 100

Figure 5.1: The Si 2p XPS core level spectra of 0.5 nm SiO_2 on n-Si (100). The feature at 99.6 eV shows Si-Si bonding that is attributed to Si in the substrate and the feature at 103.3 eV is attributed to Si-O bonding in SiO_2. 132

Figure 5.2: The UPS valence band spectrum of 0.5 nm SiO_2 on n-Si. The VBM (5.2 eV) and the cut-off due to the vacuum level (16.6 eV) are indicated. 133

Figure 5.3: The Si 2p XPS core level spectra before (grey) and after (black) deposition of 1.0 nm ZrO_2. After deposition the substrate related peak is unchanged and the oxide related peak is shifted 0.2 eV lower in binding energy. 134

Figure 5.4: The UPS valence band spectrum of 1.0 nm ZrO2. The VBM (4.2 eV) and the vacuum level (17.7 eV) are indicated. 135

Figure 5.5: The Si 2p XPS core level spectra before (grey) and after (black) deposition of 1.0 nm of Zr. After deposition the substrate related peak is shifted 0.2 eV higher in binding energy and the oxide related peak is shifted 0.5 eV lower in binding energy. 136

Figure 5.6: The Zr 3d XPS core level spectra before (grey) and after (black) deposition of 1.0 nm Zr metal. After deposition the oxide related 3d 5/2 peak is shifted 0.3 eV higher in binding energy. 137

Figure 5.7: The UPS valence band spectrum after deposition of 1.0 nm of Zr on ZrO_2. The emission extends to the Fermi level indicating metallic character and the vacuum cut-off is observed at 17.1 eV. 138

Figure 5.8: A schematic band diagram for 0.5nm SiO_2 on n-Si. The band offsets and electron affinities are indicated and an interface dipole of $\Delta = 0.2$ eV is deduced. 139

Figure 5.9: A schematic band diagram for 1.0 nm ZrO_2 on 0.5nm SiO_2 on n-Si. The band offsets and electron affinities are indicated as are interface dipoles and a field in the SiO_2 layer..... 140

Figure 5.10: A schematic band diagram for 1.0 nm Zr metal on 1.0 nm ZrO_2 on 0.5nm SiO_2 on n-Si. The Zr work function of 4.1 eV, the oxide electron affinities and the dipoles at each interface are indicated. Below is the balanced equation for the difference in the Si and Zr work functions including the dipole contribution from each interface and the potential across the dielectric layers. 141

1. Introduction to High-κ Gate Stacks: Device Scaling and Material Considerations

C.C. Fulton
Department of Materials Science and Engineering
North Carolina State University
Raleigh, North Carolina 27695-7907

1. Introduction to High-κ Gate Stacks: Device Scaling and Material Considerations

1.1 Introduction

Thermally grown silicon oxide, SiO_2, has enabled much of the metal–oxide–semiconductor (MOS) technology that is ubiquitous in today's world. This amorphous oxide has been a staple of the semiconductor industry for many years, and while the devices have become orders of magnitude smaller and faster over the last four decades, the materials used to make those devices are relatively unchanged. With its low interface state density of ~10^{10} cm^{-2} its thermodynamically stable interface with Si, and its large breakdown field of 10 MV cm^{-1} the standard is set very high for any alternative gate dielectric.

1.2 Device scaling and leakage current

The typical method to improve performance is to reduce the dimensions or scale the logic devices. Drive current is an important metric for transistor performance which indicates the time required for a device to change from the off to the on state.[1] Higher drive currents mean lower switching time of a device thus the advantages of scaling can be seen using a simple model of the field effect transistor (FET) drive current I_D:

$$I_D = \frac{W}{L}\mu C_{inv}\left(V_G - V_T - \frac{V_D}{2}\right)V_D \tag{1.1}$$

where W is the width of the transistor channel, L is the channel length, μ is the mobility, C_{inv} is the inversion capacitance, V_G is the voltage applied to the transistor gate, V_D is the voltage applied to the drain and V_T is the threshold voltage.[2,3] To increase the drive current and thus device performance, the inversion capacitance (C_{inv}) must be increased. If we regard the gate

dielectric of a metal-oxide-semiconductor field effect transistor (MOSFET) as a parallel plate capacitor then the capacitance is given by:

$$C = \frac{\kappa \varepsilon_0 A}{t} \tag{1.2}$$

where κ is the dielectric constant, ε_0 is the permittivity of free space (8.85 x 10^{-12} F m^{-1}), A is the area of the capacitor plate and t is the thickness of the dielectric. The capacitance can be increased either by reducing the thickness of the gate dielectric as in traditional device scaling or by increasing its dielectric constant.

Also of concern in modern integrated circuits is power consumption. As the thickness of the gate dielectric is reduced, quantum mechanical tunneling of electrons through the dielectric can become significant. The tunneling current through a trapezoidal barrier is given by:

$$J_{DT} = \frac{A}{t_{ox}^2} e^{(-Bt_{ox})} \left[\left\{ \Phi_B - \frac{V_{ox}}{2} \right\} e^{\left(\sqrt{\Phi_B - \frac{V_{ox}}{2}} \right)} - \left\{ \Phi_B + \frac{V_{ox}}{2} \right\} e^{\left(\sqrt{\Phi_B + \frac{V_{ox}}{2}} \right)} \right] \tag{1.3}$$

where A is a constant, $B = 4\pi / h\sqrt{2m^* q}$, Φ_B is the potential barrier height, t_{ox} is the physical thickness of the oxide, V_{ox} is the voltage drop across the oxide and m^* is the effective mass of a tunneling electron. Equation (3) shows that the leakage current increases exponentially with decreasing oxide thickness, and with gate dielectric dimensions approaching 1.0 nm the leakage current will become the dominant mechanism for device power consumption.

Equation (2) shows that as an alternative to the usual decrease in gate dielectric thickness the same performance increase could be achieved by an increase in the oxide dielectric constant. Achieving an increase in performance without an increase in quantum mechanical leakage current essentially defines the need for high-κ alternative gate dielectrics.

1.3 Issues for advanced gate dielectrics

There are a number of material qualities that a replacement gate dielectric must possess in order to achieve the desired electrical characteristics for high performance logic circuits.

1.3.1 Si – dielectric interface

After fifty years of research and industrial experience, SiO_2 is a relatively well understood material. For example, in an SiO_2 film created using a state of the art process the defect density at the Si-SiO_2 interface is of the order 10^{10} cm^{-3} or one defect in ten thousand interface atoms. Most of the candidate high-κ dielectric materials, however, are transition metal oxides that are vastly different in their chemistry compared to SiO_2. These oxides tend to have higher interface state densities than does SiO_2 and because of their different chemistry may undergo silicide formation or other undesirable interface reactions.[4,5,6] To reduce the defect density and the interfacial reactions an ultra thin buffer layer (~0.5nm) of high quality SiO_2 is often employed. This buffer layer can yield low defect densities approaching that of thermally grown SiO_2 but the thickness must be controlled as the low-κ buffer layer can dominate the overall gate capacitance.

1.3.2 Permittivity, barrier heights and bandgaps

Equations 1-3 indicate that to increase capacitance and reduce tunneling current a material must be found that has a large permittivity when compared to SiO_2 (κ=3.9) and also has large barrier heights with respect to Si in both the conduction and valence bands. Unfortunately, the general trend is that with increasing dielectric constant, bandgaps and therefore barrier heights decrease. Thus, for a high-κ dielectric to be technologically viable we must find a material with a reasonable bandgap and a sufficiently large dielectric constant

such that it can be integrated into the complimentary metal oxide semiconductor (CMOS) process. The transition metal oxides, in particular zirconium and hafnium oxides and silicates, have received particular attention because of their relatively large bandgaps (~5.7 eV) and their dielectric constants of 15-25.[2,7,8,9] Moreover, their band offsets have been predicted to be favorable for blocking both holes and electrons.[10]

1.3.3 Thermodynamic stability

A modern CMOS process includes a 900-1000°C dopant activation anneal during which the gate dielectric must resist significant chemical changes or interfacial reactions. Previous studies of Zr oxides and silicates on Si have noted several instabilities. The interface between Zr oxides and Si have been reported to be chemically unstable at high temperatures by Chang *et al*.,[4] Copel *et al*.[5] and Stemmer *et al*.[6] among others. Results indicate that the temperature at which the interface decomposes during vacuum annealing is in the range of 880 - 1000°C. Chang *et al*. have suggested possible reaction paths for converting ZrO_2 and $ZrSiO_4$ into gaseous SiO and have also calculated the free energies for these reactions at different temperatures and equilibrium pressures. The results show that at low overpressures of SiO and ZrO the decomposition reaction is energetically favorable.[4] Silicate compositions must also be chosen carefully as phase separation of some compositions of mixed $(ZrO_2)_x(SiO_2)_{1-x}$ into regions of ZrO_2 and SiO_2 has been reported for annealing temperatures of 900° C.[11] These results suggest that care must be taken to choose the material composition and annealing conditions to be used in a high-κ process.

1.3.4 CMOS process considerations

Industry experience has shown that the growth conditions of an SiO_2 gate dielectric can significantly affect the material properties including density, index of refraction and

dielectric constant. All of the processes used to deposit alternative dielectrics utilize non-equilibrium growth conditions that can result in significant variation in the film properties. To choose the successor to SiO_2 as a gate dielectric, we must have an understanding of how changes in the growth parameters alter the high-κ material properties including that barrier heights and electronic structure. For example, Fissel *et al.* have deposited PrO_2 on Si and observed changes in the electronic structure for different growth and annealing parameters.[12] The origin of these variations must be understood and controled during the CMOS process for a dielectric to be manufacturable.

1.4 Gate electrodes

Polycrystalline silicon is the dominant gate electrode material in modern CMOS technology primarily because precise control of the Si doping can tune the threshold voltage for both nMOS and pMOS transistors. In the long term the ITRS roadmap predicts that poly-Si gates will be replaced beyond the 70 nm technology node. The need for this replacement is driven primarily by carrier depletion effects near the dielectric – gate interface where the depletion width in the gate material contributes significantly to the total capacitance of the gate stack.

The alternative to heavily doped poly-Si is to integrate a metal layer and there are generally two approaches to integrating metal gate materials; they are: 1) to choose a single material with a work function that falls near the center of the Si bandgap or 2) to choose two different materials that have appropriate work functions for pMOS and nMOS devices respectively. The first approach could prove difficult in practice due to the scaling of voltage supplies to less than 1.0 V. This precludes mid-gap metal gates as they would give a V_T of ~0.5 V making it difficult to turn on a device. A threshold voltage of 0.2 to 0.3 V is desired

for these devices leaving the "dual metal" approach as the preferred alternative. Generally, elemental, low work function metals are reactive and have been shown in some cases to reduce the gate oxide during annealing.[13] High work function elemental metals tend not to be reactive with respect to the gate oxide but often have large diffusivity in the dielectric materials and do not adhere well.[2] With these considerations alloys of metals, silicides or nitrides may be more manufacturable choices but their work functions and interface properties are generally uncharacterized, in particular with respect to the transition metal oxides that are leading candidates as replacement gate dielectrics.

1.5 Thesis approach

The gate stack structures considered for future devices will become significantly more complex than today's structures of poly-Si gates, SiO_2 dielectrics and Si (100) substrates. These structures will have multiple interfaces and include more complex materials including, metal gates, high-κ dielectrics, ultra-thin SiO_2 buffer layers and Si-Ge alloy substrates.

What follows is a spectroscopic study of high-κ gate stacks, in particular their interface chemistry and electronic structure. These have studies predominantly utilized the integrated process and characterization system which allows deposition and study of layered high-κ structures under UHV conditions. In addition, collaborative studies, in conjunction with the National Synchrotron Light Source and the Stanford Synchrotron Radiation Laboratory, have been undertaken to study the conduction band states by x-ray absorption spectroscopy.

Chapter 2

Photoemission spectroscopy has been used to address the interface stability of ZrO_2 with respect to a Si substrate. This chapter addresses three issues: 1) the development of the band offsets and electronic structure during the low temperature (T<300°C) growth processes, 2) variations in the band structure as effected by process conditions and annealing (T<700°C) and 3) the interface stability of Zr oxide films at high temperatures (T>700°C). Annealing the as-grown films to 600°C results in a ~2 eV shift of the ZrO_2–Si band alignment, giving a band offset that is favorable to devices and in agreement with predictions and with other experiments. We propose that the as-grown films contain excess oxygen resulting in a charge transfer from the Si substrate to the internal (ZrO_2–SiO_2) interface and that annealing to 600°C is sufficient to drive off this oxygen. Further annealing to 900°C, in the presence of excess Si at the surface, results in decomposition of the oxide to form $ZrSi_2$.

Chapter 3

In this study we expand on the low temperature instability noted in Chapter 2. Titanium, zirconium and hafnium oxides have been deposited on ultra-thin (~0.5 nm) SiO_2 buffer layers and metastable states have been identified which give rise to large changes in their band alignments with respect to the Si substrate. This results in a potential across the interfacial SiO_2 layer, significant band bending and large shifts of the high-κ valence band. The magnitude of the shift differs for the three materials and is dependant on both the SiO_2 buffer layer thickness and annealing temperature. A model has been proposed where the magnitude of the observed shift is related to the oxygen solubility in the high-κ materials and where excess oxygen accumulates near the high-κ–SiO_2 interface providing electronic states that are available to electrons that tunnel from the substrate.

Chapter 4

This chapter discusses band edge electronic structure of 1) nanocrystalline elemental and complex oxide high-κ dielectrics, and 2) non-crystalline Zr and Hf silicates and Si oxynitride alloys. Experimental approaches include X-ray absorption spectroscopy, photoconductivity, and visible/vacuum ultra-violet and spectroscopic ellipsomentry (SE). These measurements are complemented by Fourier transform infra-red absorption, x-ray photoelectron spectroscopy, high resolution transmission electron microscopy, and x-ray diffraction. Three issues are highlighted: Jahn-Teller term-splittings that remove band edge d-state degeneracies in nanocrystalline films, intrinsic bonding defects in ZrO_2 and HfO_2, and chemical phase separation and crystallinity in Zr and Hf silicate and Si oxyntride alloys.

Chapter 5

Chapter 5 discusses a study of the electronic properties including electron affinities and work functions, valence band maxima, band bending in the Si and internal fields in a layered high-κ gate stack. With this information the band offsets can be reconstructed and also the deviation from the Schottky-Mott (or electron affinity) model at each interface can be determined. These models presume that aligning the vacuum levels of two materials will give electronic barrier height for a heterojunction. Interface bonding and defect states can contribute to charge transfer across the interface, forming a dipole and altering the barrier heights. The band offsets and vacuum levels are independently measured thereby determining the deviation from these vacuum level models. That deviation is presented as an additional constant, Δ, the interface dipole, and discussed in terms of an interface induced gap states model and likely interface bonding.

Chapter 6

This chapter serves as a summary of the dissertation and suggests future research directions based on the findings.

1.6 References

[1] Wong, H -S P, IBM J. Res. Dev. **46**, 133 (2002)

[2] R. M. Wallace, G. D. Wilk, Crit. Rev. Sol. St. Mat. Sci. **28**, 231 (2003)

[3] D.K. Schroder, *Semiconductor Material and Device Characterization* (Wiley-Interscience Publishers, New York, 1998)

[4] J. P. Chang, Y.-S. Lin, Appl. Phys. Lett. **23**, 3824 (2001)

[5] M. Copel, M. Gribelyuk, E. Gusev, Appl. Phys. Lett. **76**, 436 (2000)

[6] S. Stemmer, Z. Chen, R. Kedling, J.-P. Maria, D. Wicaksana, A. I. Kingon, J. Appl. Phys. **92**, 82 (2002)

[7] G. D. Wilk, R. M. Wallace, J.M. Anthony, J. Appl. Phys. **89**, 5243 (2001)

[8] J. P. Chang, Y.-S. Lin, S. Berger, A. Kepten, R. Bloom, S. Levy, J. Vac. Sci. Technol. B **19**, 2137 (2001)

[9] E. P. Gusev, E. Cartier, D. A. Buchanan, M. Gribelyuk, M. Copel, H. Okorn-Schmidt, C. D'Emic, Microelec. Eng. **59**, 341 (2001)

[10] J. Robertson, J. Vac. Sci. Technol. B **18**,1785, (2000)

[11] D.A. Neumeyer, E. Cartier, J. Appl. Phys. **90**, 1801 (2001)

[12] A. Fissel, J. Dabrowski, and H.J. Osten, J. Appl. Phys. **91**, 8986, (2002)

[13] V. Misra, G.P. Heuss, H. Zhong, Appl. Phys. Lett. **78**, 4166 (2001)

2. Interface Instabilities and Electronic Properties of ZrO_2 on Silicon (100)

C.C. Fulton and T.E. Cook Jr.
Department of Materials Science and Engineering
North Carolina State University
Raleigh, North Carolina 27695-7907

G. Lucovsky and R.J. Nemanich
Department of Physics
North Carolina State University
Raleigh, North Carolina 27695-8202

These results published in:

Journal of applied Physics
Vol. 96, No. 5, p2665 (2004).

2. Interface instabilities and electronic properties of ZrO_2 on silicon (100)

2.1 Abstract

The interface stability of Zr-based high-k dielectrics with an oxide buffer layer was explored with x-ray (hυ=1254eV) and ultraviolet (hυ=21.2eV) photoemission spectroscopy. Zirconium oxide films were grown and characterized *in-situ* in a stepwise sequence to explore their chemical stability and electronic properties as a function of film thickness and processing conditions. The buffer layers serve to lower the interface state density and to address the high temperature instabilities of ZrO_2 in direct contact with Si. This research addresses three issues: 1) the development of the band offsets and electronic structure during the low temperature (T < 300°C) growth processes, 2) variations in the band structure as effected by process conditions and annealing (T < 700°C) and 3) the interface stability of Zr oxide films at high temperatures (T > 700°C). Annealing the as-grown films to 600°C results in a ~2 eV shift of the ZrO_2 – Si band alignment, giving a band offset that is, favorable to devices, in agreement with predictions and in agreement with other experiments. We propose that the as-grown films contain excess oxygen resulting in a charge transfer from the Si substrate to the internal (ZrO_2 – SiO_2) interface and that annealing to 600°C is sufficient to drive off this oxygen. Further annealing to 900°C, in the presence of excess Si at the surface, results in decomposition of the oxide to form $ZrSi_2$.

2.2 Introduction

The planned scaling of integrated circuit devices involves a reduction of the gate insulator thickness to obtain the targeted capacitance and sheet charge density in the channel. As the gate dielectric thickness is reduced below 2 nm, direct tunneling between the gate and channel becomes significant, leading to increased power consumption and device failures. As an alternative to reducing the physical thickness of the gate oxide the dielectric constant could be increased. This would allow the desired increase in capacitance with a physically thicker layer, resulting in both a reduced tunneling current and an increase in sheet charge density. With conventional thermal oxides and oxynitrides approaching their physical limits, the exploration of alternative materials has gained significant momentum.[1]

The fundamental criteria for a gate dielectric include band offsets that will block both electrons and holes, chemical stability in contact with both the silicon substrate and the gate material, and a low density of interface electronic states. Zirconium oxides and silicates, with their large bandgap of ~5.8 eV and dielectric constants of 15-25, are of particular interest.[7,2,3] Moreover, the ZrO_2–Si band offsets have been predicted to be favorable for blocking both holes and electrons.[4]

A typical complimentary metal oxide semiconductor (CMOS) process includes a 900-1000°C dopant activation anneal during which the gate dielectric must not undergo significant chemical changes or interfacial reactions. Previous studies of Zr oxides and silicates on Si have noted several instabilities. Under certain conditions, the interface between Zr oxides and Si have been reported to be chemically unstable at high temperatures by Chang *et al*., Copel *et al*. and Stemmer *et al*. among others.[5,6,7] Results indicate that the temperature at which the interface decomposes during vacuum annealing is in the range of

880 - 1000°C. Chang *et al*. noted the instability and suggested possible reaction paths for converting ZrO_2 and $ZrSiO_4$ into gaseous SiO.[5] They have also calculated free energies for these reactions at different temperatures and equilibrium pressures, showing, that at low overpressures of SiO and ZrO that the decomposition reaction is energetically favorable.

Stemmer *et al*. showed that annealing in an oxygen partial pressure < 10^{-7} Torr yielded $ZrSi_2$ precipitates and that greater partial pressures of oxygen can suppress the decomposition reaction.[7] They also found that at high oxygen partial pressures, SiO_2 formation occurs at the dielectric – Si interface.

Other studies have explored the electronic structure of Zr dielectrics on Si. Miyazaki *et al*. found a bandgap of 5.5 eV and a valence band offset (VBO) of 3.15 eV for evaporated ZrO_2 on Si(100). Their results also indicated that annealing these films to 500°C in 10^{-5} Torr dry O_2 does not significantly effect either the bandgap or the VBO.[8,9]

In this study, we have spectroscopically explored the chemical and electronic instabilities of Zr – oxide on a Si substrate with SiO_2 and Si_3N_4 buffer layers. Using UHV transfer between processing and characterization chambers we were able to perform measurements at various points during film processing and explore the evolution of the Zr oxide films from both a chemical and an electronic perspective.

2.3 Experiment

All experiments were performed on 25mm diameter, *n*-type, 0.05-1 ohm-cm (1×10^{18} to 5×10^{15} cm^{-3} phosphorous), Si (100) wafers. Prior to loading into ultra high vacuum (UHV) the wafers were cleaned with a wet chemical dip in JT Baker 100 for 15 minutes at room temperature, a one minute rinse in deionized water, and a 10:1 $HF:H_2O$ spin etch.

After chemical cleaning the wafer was loaded into a UHV integrated growth and analysis system which includes a linear UHV transfer system interconnecting 13 different process and characterization chambers. Five of these chambers were employed in this study, including: plasma oxidation, electron beam deposition of zirconium, solid source molecular beam epitaxy (MBE) deposition of Si, X-ray photoemission spectroscopy (XPS), and ultra violet photoemission spectroscopy (UPS).

An initial oxygen plasma exposure was employed to remove residual hydrocarbon contamination and to form the thin (0.5 nm) oxide buffer layer. Zirconium oxide thin film growth involved successive steps of zirconium metal deposition followed by plasma oxidation with annealing steps to relax the oxide structure and to explore film stability. After each process step the films were analyzed with XPS and UPS to observe trends in chemical and electronic properties.

The initial O_2 plasma clean/buffer layer formation and subsequent oxidations were performed in a remote plasma-enhanced chemical vapor deposition (RPECVD) chamber with a base pressure of $3 \cdot 10^{-9}$ Torr. Plasma exposures took place with a wafer surface temperature of 300°C, a gas flow of 10 standard cubic centimeters per minute (sccm) O_2 and 50 sccm He and an operating pressure of 60 mTorr He/O_2. Twenty watts of inductively coupled RF power were used to excite the plasma.

Zirconium metal depositions were completed with the substrate at room temperature in a UHV chamber with a base pressure of $5 \cdot 10^{-10}$ Torr. The deposited Zr thicknesses of 0.2, 0.4 and 0.8 nm were obtained at rates of 0.04 nm/s where the deposition rate and thickness were measured with a quartz crystal oscillator.

Annealing steps were performed in UHV, with wafers radiatively heated by a coiled tungsten filament and temperatures measured by a thermocouple held behind the center of the wafer. For temperatures of 600°C and above, the wafer surface temperature was measured with an optical pyrometer; for lower temperatures, the thermocouple reading has been calibrated based on a linear extrapolation from higher temperatures where the pyrometer can be used. A Eurotherm temperature control was employed to regulate the annealing process, utilizing ramp rates of 40°C/min with maximum sample temperatures held for either five or ten minutes.

XPS characterization takes place at a pressure of $2 \cdot 10^{-9}$ Torr using the 1253.6eV Mg *K*α line from a Fisons XR3 dual anode source and a Fisons Clam II electron analyzer. The resolution of the analyzer was determined from the full width half maximum (FWHM) of a gold 4f 7/2 spectral peak to be approximately 1.0 eV; however, through curve fitting, the centroid of spectral peaks can be resolved to ±0.1 eV. Observation "windows" were set around the Si 2p, O 1s and Zr 3d binding energies to record core level shifts. Ultraviolet photoemission spectra were obtained using a He discharge lamp primarily generating the He I line at 21.2 eV in a chamber with a base pressure of $3 \cdot 10^{-10}$ Torr. A VSW 50mm mean radius hemispherical analyzer and VSW HAC300 were operated with a pass energy of 10 eV resulting in an electron energy resolution of 0.1 eV. A negative 4.00 V bias was applied to overcome the analyzer work function. All photoemission spectra measured binding energy relative to the Si Fermi level and the electron spectrometers have been calibrated with an *in-situ* deposited Au film.

The approximate oxide film thickness can be calculated from the thickness of the deposited metal layer using the molar densities and the molar masses of Zr metal and ZrO_2.

This analysis gives a ratio of 1.5 : 1 for the thickness of a ZrO_2 film formed from Zr metal. The estimated film thicknesses discussed here are calculated in this way and assume complete oxidation of the deposited Zr layer. This approach has been corroborated by the relative intensity changes of the Si bulk peak from the Si 2p core level spectra, as a function of film thickness.

In addition to the thin (~0.5 nm) SiO_2 buffer layer, separate experiments were conducted where a thick (30 nm) deposited SiO_2 buffer and a 1.0 nm Si_3N_4 buffer were employed to further explore the stability of the Zr oxide. The thick, 30 nm, SiO_2 buffer was deposited by RPECVD using 10 sccm of 1% SiH_4 in He, 10 sccm of O_2 and 50 sccm of He gasses, for 120 minutes. The nitride buffer was formed by exposing a clean Si wafer to an electron cyclotron resonance (ECR) plasma at 600°C and $7.5 \cdot 10^{-4}$ Torr N_2 for 5 minutes. After buffer layer formation, ZrO_2 growth proceeds in the same stepwise deposition, annealing and spectroscopy procedure as was employed with the 0.5 nm SiO_2 buffer. A solid source MBE system was used to deposit 2.0 nm of Si on top of the high-k layer to explore stability in the presence of excess Si.

2.4 Results

2.4.1 Low temperature Zr oxide formation

With the stepwise growth and characterization techniques the evolution of the interface chemistry and valence band electronic states can be measured as a function of film thickness. Metal films were deposited in steps of 0.2, 0.2, 0.4, 0.8 and 0.8 nm which, after oxidation, gave cumulative oxide thicknesses of 0.3, 0.6, 1.2, 2.4, 3.5 nm, respectively, where these values have been determined using the density-ratio approximation discussed above.

In an effort to determine the band bending of the initial oxidized surface we had previously measured the VBM and Si 2p core level of a clean, hydrogen terminated Si(100) surface.[10] For a wafer of the same specification as those used in this study we find the Si VBM to be 0.85eV below the Fermi level, and the Si 2p core level at 99.65eV. This gives an energy difference between the Si 2p core level and the VBM of ΔE=98.8± 0.1eV. The result is similar to that of other reports.[11] The small difference may arise due to different calibrations of the XPS and UPS electron spectrometers. The Si 2p core level for the initial thin SiO_2 film (observed at 99.65eV), in conjunction with this ΔE place the Si fermi level at 0.85±0.1eV above the VBM. The resistivity range of the substrate also gives the bulk Fermi level at ~0.9± 0.1eV above the VBM. These results are consistent with flat band conditions after the initial oxidation.

The XPS of the initial plasma oxidized Si (100) surface displayed the bulk Si 2p core level at 99.65 eV binding energy and an oxide related peak at 103.3 eV (Table 1). These results were essentially identical to our prior report which indicated flat bands at the interface of the SiO_2 buffer layer and the Si.[10] Analysis of the UPS data obtained after the formation of the SiO_2 buffer indicated a valence band offset (VBO) of 4.3 eV, in agreement with our previous results and other reports.[10,12]

After the first 0.2 nm Zr deposition and oxidation, the O 1s core level spectrum, shown in Fig. 1, indicated a large shift in binding energy. We found that the core level from the as-prepared SiO_2 buffer layer was at 532.5 eV and that after the formation of 0.3 nm of ZrO_2, the strongest peak was then observed at 531.6 eV, with a noticeable shoulder at 529.9 eV. Further growth resulted in the ~529 eV peak becoming more intense, while the peak in the 531 eV range became relatively less intense. Both peaks tended to shift to lower

binding energy during the process. At 1.2 nm film thickness, the peaks were of approximately equal intensity and were centered at 531.4 and 529.5 eV respectively. After the final growth step (3.5 nm film thickness), the more intense peak was at 529.1 eV with a shoulder at 531.3 eV.

The oxide-related Si 2p core level, shown in Fig. 2, displayed similar trends, shifting from 103.3 to 102.2 eV after the formation of 0.3 nm ZrO_2. After the deposition of 1.2 and 3.5 nm films, the oxide related Si 2p peak was observed at 101.7 and 101.5 eV, respectively. Shifts in the Si 2p substrate peak were much smaller, with the peak initially observed at 99.65 eV for the SiO_2 buffer layer, shifting to 99.45 eV for the 0.3 nm film, and finally to 99.30 eV after 3.5 nm had been deposited. We ascribe the shifts in the ~99 eV peak to changes in band bending of the Si substrate.

The Zr 3d core level (Fig. 3) displayed an increase in intensity with film thickness, and, like the O 1s core level, shifted to lower binding energy with each processing step. The peak position shifted from 182.4 eV for the 0.3 nm Zr oxide to 181.4 eV for the 3.5 nm film.

The UPS spectra of the oxidized films indicated the valence band maximum (VBM) to be at 3.4 eV binding energy (relative to the bulk Fermi level), after the first 0.3 nm of oxide growth. The VBM shifted progressively toward 1.9 eV with each additional deposition step (Fig. 4). Table 1 contains a summary of the XPS core level binding energies and the UPS VBM observed during low temperature growth.

2.4.2 High temperature instability

To explore thermal stability, the stepwise grown film was annealed to 600, 750 and 900°C. The 600°C annealing resulted in a large shift in the oxide valence band (Fig. 5), shifting from a binding energy (BE) of 1.9 eV for the as-grown 3.5 nm film to a BE of 4.6 eV

for the post annealed film. Further annealing to 750°C resulted in a 0.2 eV shift of the VBM back toward the Fermi level to a BE of 4.4 eV (Table 1).

The core level spectra underwent similar large shifts after annealing to 600°C (Fig. 6). The O 1s spectrum of the as-grown film initially displayed a 529.1 eV peak with a 531.3 eV shoulder, that, after annealing, had shifted to 531.2 eV with a shoulder at 532.5 eV. The Zr 3d peak shifted from 181.4 to 183.8 eV. The oxide related Si 2p shifted from 101.5 to 103.1 eV, and the bulk related Si 2p shifted from 99.30 to 99.50 eV. After annealing, the oxide related Si 2p core level showed an increase in intensity and a decrease in peak width compared to the as-deposited state. Similar to the changes in the VBM the core level spectra indicated small changes with further annealing to 750°C. The Zr 3d core level was shifted 0.1 eV lower in binding energy, the O 1s core levels were unchanged and the Si 2p core levels were both higher in binding energy by 0.2 and 0.05 eV for the oxide and bulk related features, respectively.

After annealing to 900°C the O 1s core level was reduced to an almost undetectable level, the Zr 3d peak was shifted to 179.1 eV, a position representative of Zr metal or Zr silicide. The oxide related Si 2p was not observable and the bulk related Si 2p was observed at 99.45 eV, having become much more intense. The UPS spectrum showed emission extending to the Fermi level, indicating a film with a metallic character and atomic force microscopy (AFM) revealed a high density of islands with radii of ~500 nm.

2.4.3 Stability with alternate buffer layers

To explore the conditions of high temperature stability ZrO_2 films were prepared with both a 30 nm SiO_2 buffer layer, and a 1 nm Si_3N_4 buffer layer. The 3 nm Zr oxide film was characterized in the as-grown state, annealed, and then characterized again.

After formation of the Zr oxide on the 30 nm SiO_2 buffer, the O 1s spectrum displayed peaks at 533.5 and 531.6 eV (Table 2). Annealing in UHV to 600°C resulted in a shift of the 533.5 eV peak to 533.2 eV while the other peak remained unchanged at 531.6 eV (Fig 7). Annealing to 750°C found the O 1s peaks were at 533.1 eV and 531.5 eV, respectively, and a subsequent 900°C anneal had shifted them to 533.2 and 531.3 eV. After annealing to 900°C, the 533.2 eV peak was slightly increased in intensity relative to the peak at 531.3 eV. The oxide related Si 2p core level remained fixed at 104.0 eV through the annealing steps (Fig 7), and the Zr 3d core levels showed small shifts similar to the O 1s spectra.

A 2.0 nm thick Si layer was deposited by MBE on the annealed Zr oxide film to explore the effect of excess Si on the decomposition process. After Si deposition the Si 2p core level showed a Si bulk peak at 99.55 eV as well as the oxide related peak at 103.6 eV (Fig 8). The SiO_2 related O 1s peak was unchanged at 533.2 eV, but the ZrO_2 related peak was shifted slightly to 531.5 eV. The Zr 3d core level was reduced in intensity due to the Si layer and was shifted to 183.8 eV.

Annealing to 600 and subsequently 750°C (Fig. 8) resulted in a decreased intensity of the Si 2p bulk related core level, and the oxide related peak shifted back to 104.0 eV. The two peaks of the O 1s spectra were at 533.2 and 531.6 eV after both the 600 and 750°C annealing steps. These peaks also changed in relative intensity with annealing, with the 533.2 eV peak increasing with respect to the 531.6 eV peak.

When annealed to 900°C the film underwent significant changes. The intensity of the O 1s core level was reduced to a level only slightly above the system noise, the oxide related

Si 2p core level was not observed, and the Zr 3d peak was shifted to a position characteristic of Zr metal or Zr silicide.

To further evaluate the effect of the buffer layer on high temperature stability we deposited a 1 nm Si_3N_4 buffer layer, 3 nm of ZrO_2 and then repeated the annealing experiment, with and without excess Si. The as-grown film as characterized by XPS, displayed core level positions of: 99.55V for the Si 2p bulk peak, 101.5 for the Si 2p nitride related peak, 529.2 for the O 1s peak, and 181.5 eV for the Zr 3d core level (Table 3). On annealing to 600°C all of the core level spectra shifted to higher binding energy. The Si 2p core levels shifted to 99.70 and 102.3 eV, respectively, the O 1s shifted to 530.9, and the Zr 3d shifted to 183.2. The films was further annealed to 750 and 900°C after which the bulk Si 2p was observed at 99.80 eV, the nitride bonded Si 2p shifted slightly to 102.4 eV, and the O 1s and Zr 3d were unchanged at 530.9 and 183.2 eV, respectively.

After a 2 nm thick Si layer was deposited via MBE, the bulk Si 2p core level was found to be at 99.50 eV, the nitride bonded Si 2p was no longer visible, and the O1s and Zr 3d core levels had shifted to 531.3 and 183.5 eV, respectively. After annealing to 600°C the nitride bonded Si 2p was once again visible at 102.8 eV, along side the bulk peak at 99.60 eV. Annealing to 750 and finally 900°C resulted in the emergence of a metallic or silicide like Zr 3d core level at 179.6 eV and a reduction in the oxide related component at 182.9 eV. After 900°C the VB spectra was of metallic character, with intensity extending to the Fermi level. The nitride bonded Si 2p was detected at 102.2 eV, a position similar to the original Si_3N_4 buffer layer. Tables 2 and 3 contain a summary of the date for ZrO_2 films on alternate buffer layers.

2.4.4 Low temperature instability

The large shifts of the VBM and core levels, observed after annealing to 600°C, was explored thoroughly in another study that also measured a similar effect observed in Ti, and Hf oxides.[13] Our observations of ZrO_2 thin films indicated that when annealed at low temperatures, (T < 600°C) the VBM and core levels shift up to 2 eV. Shifts in the valence band and core levels were observed for annealing temperatures as low as 200°C. Exposing the annealed film to an oxygen plasma was found to shift the VBM and core levels back to their respective as-grown binding energy positions. Subsequent annealing and oxidation steps consistently shift the band structure and, to within experimental error, give identical results.

These shifts were observed for ZrO_2 deposited on the 0.5 nm SiO_2 and the 1 nm Si_3N_4 buffer layers but not the 30 nm SiO_2 buffer. To explore this, a series of 3 nm ZrO_2 films were deposited on SiO_2 buffer layers of different thickness (0.5, 2.0 and 3.5 nm) and the shifts in the electronic structure were measured. Findings from this series of films indicate that the magnitude of the VB and core level shifts decreases with increasing buffer layer thickness, approaching zero as the buffer layer thickness increases beyond 3.5 nm.

2.5 Discussion

We divide this section into three parts detailing: A) the integrity of the SiO_2 buffer layer during low temperature ZrO_2 deposition, B) the high temperature instability and oxide decomposition, and C) the low temperature instability and changes in electronic structure.

2.5.1 Integrity of the SiO_2 buffer layer

The relative intensity of the bulk and oxide bonded Si 2p core level remained unchanged during film growth, indicating that, to our detection sensitivity, there was no

diffusion of Si into the ZrO_2 layer. Nor were any core level shifts observed that would indicate the formation of a Zr silicate. It was also observed that, with annealing to 600°C, the positions of the Si 2p and the SiO_2 related component of the O 1s core level return to that of the as-prepared buffer layer. This further suggests that there has been no chemical change of the SiO_2 in the buffer layer. Stemmer *et al*. and Ramanathan *et al*. have shown that the formation of a silicate is thermodynamically unfavorable and that over a wide range of compositions the films will spontaneously phase separate in the amorphous phase.[14,15,16] Based on this analysis we suggest that the low temperature growth process allows us to deposit ZrO_2 on an ultra-thin SiO_2 buffer layer while maintaining the integrity of the two layers.

2.5.2 High temperature instability

Previous work on Zr oxides has found them to be stable on Si, but only in the limit of temperatures less than ~850°C.[5,6,17,18] There has, however, been some disagreement about the particular temperature where this instability appears. Copel *et al*. find that 900°C annealing for two minutes does not lead to decomposition of their ZrO_2 films but that a 30 sec flash to 1000°C does result in decomposition.[6] Chang *et al*. find that 880°C is sufficient to drive the decomposition reaction at low oxygen partial pressures, and they also propose likely reaction paths, all of which involve excess Si as a reactant (Table 4).[5]

Our results indicate that during vacuum annealing ZrO_2 films on thin (0.5 nm) SiO_2 buffer layers are unstable at ~900°C, decomposing into a metallic film, which is most likely $ZrSi_2$. Atomic force microscopy images of the decomposed films display a high density of ~500 nm diameter islands. Stemmer *et al*. have also reported the formation of $ZrSi_2$ islands during vacuum annealing of Zr oxide films on Si.[7]

In contrast to the results for the thin buffer layer, we find that two different buffer layers, a 30 nm SiO_2 layer and a 1 nm Si_3N_4 layer, can both suppress the decomposition reaction during annealing at up to ~900°C. Moreover, the deposition of a top, 2nm, Si layer and a second annealing to 900°C, results in the decomposition of the ZrO_2 film and the formations of Zr silicide. These results indicate that the availability of excess Si leads to the decomposition of the ZrO_2. We suggest that the 0.5 nm SiO_2 layer allows Si to diffuse from the substrate to the high-k interface leading to the decomposition reaction. We further suggest that the 30 nm SiO_2 and the 1 nm Si_3N_4 buffer layers inhibit this diffusion and thus prevent the decomposition of the ZrO_2.

Reaction probabilities from a free energy perspective have been calculated by Chang *et al*. and a summary of that work is contained in Table 4.[5] Ramanathan *et al*. have reported that Hf and Zr-silicate films tend to phase separate into zirconia and silica during high-temperature anneals, indicating that the first three reaction paths in Table 4 are unlikely to occur.[16] Consequently, we expect that the most likely reaction path for the decomposition of our films is the last reaction path given in Table 4, $2ZrO_2 + 5Si \rightarrow ZrO_{(g)} + 3SiO_{(g)} + ZrSi_2$.

Stemmer *et al*. have demonstrated that annealing films in an oxygen ambient rather than in vacuum can improve stability at 900°C, but these annealing conditions will likely result in SiO_2 growth at the Si interface.[7] With respect to thermal stability, a thin silicon nitride buffer layer is a better alternative than thick SiO_2 as it: provides an improved thermal stability even for very thin layers and inhibits the generation of parasitic SiO_2 at the Si interface.

2.5.3 Low temperature instability

The large shifts in electronic structure observed with annealing have been explored in another publication, which also includes findings for other transition metal oxides (TiO_2 and HfO_2).[13] The following presents a summary of those results as they apply to ZrO_2.

We suggest that exposure to a remote oxygen plasma (and a high concentration of atomic oxygen) introduces excess oxygen into the ZrO_2 film. We further suggest that this excess oxygen is a source of electronic states near the buffer layer – high-k interface. Electrons tunnel from the substrate to populate these states, giving rise to a potential across the SiO_2 buffer layer. Annealing removes the excess oxygen and the associated electronic states, leading to flat bands with no potential across the SiO_2 buffer layer. Figure 9 schematically shows the band structure of the as-grown and annealed ZrO_2 films.

As discussed in Ref 13, the magnitude of the band structure shift decreases as the buffer layer thickness is increased. With our model, the probability of an electron tunneling through the buffer layer would be expected to decrease as the buffer layer thickness increased. This tunneling dependence would explain the lack of band structure shifts in the ZrO_2 film prepared on a 30 nm SiO_2 buffer layer.

To estimate the charge needed to produce the measured shifts we can treat the buffer layer as a simple dielectric filled capacitor with thickness of d = 1.0 nm, a dielectric constant of k = 3.9 for SiO_2 and a voltage of V = 1.0 V. From this we determine a charge density of $\sim 2 \cdot 10^{13}$ cm^{-2}. We can likewise estimate the positive charge in the Si from the change in band bending at the Si substrate. We use $N_s = \sqrt{2k\varepsilon_0 N_D V / q}$ to calculate the charge density, where N_s is the surface charge density, $N_D = \sim 1 \cdot 10^{18}$ cm^{-3} is the bulk doping density of the Si, q is the charge of an electron, ε_0 is the permittivity of free space, k = 12 is the dielectric

constant of Si, and $V = 0.3$ V is the change in band bending. This gives a charge density of $N_s = 2 \cdot 10^{12}$ cm^{-2} and, thus, the two calculations are in relative agreement. The excess charge may not be completely localized at the high-k–SiO_2 interface or other conditions may exist to explain the discrepancy in the two different charge density estimates.

Other studies have reported relatively high values of negative fixed charge, ~10^{12} cm^{-2}, at internal interfaces between SiO_2 and ZrO_2[19,20,21]. There have also been reports of positive fixed charge at approximately the same density.[19] Annealing has also been shown to reduce the fixed charge density in films that exhibit either positive or negative fixed charge.[19] The magnitude of the fixed charge density agrees relatively well among the published studies, even for films that have been prepared by different techniques. The sign of the fixed charge, on the other hand, is not well understood, and the conflicting results may suggest that multiple processes are involved. It is evident that further study is needed to correlate processing conditions with the electronic properties of these interfaces.

2.6 Conclusions

We have used x-ray and ultraviolet electron spectroscopy to study the chemistry and interface electronic states during the stepwise growth and annealing of ZrO_2 on Si. An interfacial buffer layer of SiO_2 or Si_3N_4 was formed to reduce the number of interface states and improve interface stability. The low temperature deposition technique allowed the formation of ZrO_2 on the buffer layer without mixing, and the two layers remain distinct. Annealing the films to 600°C resulted in large changes in the band alignment that are attributed to the presence of excess oxygen in the as grown films. These large shifts of up to 2 eV are consistent and repeatable for multiple oxidation and annealing steps. Annealing at

900°C resulted in film decomposition into $ZrSi_2$, and a high density of silicide islands was observed with AFM.

The stability of the film at 900°C was improved by both a thick (30 nm) SiO_2 buffer layer and a 1 nm Si_3N_4 buffer layer. Zirconium oxide films grown on these alternate buffer layers showed little change with annealing at high temperatures. However, a similar 900°C annealing step after the addition of a 2 nm Si cap led to decomposition of the ZrO_2. These results demonstrate that the presence of excess Si leads to a decomposition reaction of the ZrO_2 thin films and that a thin Si_3N_4 buffer layer may improve thermal stability.

2.7 Acknowledgements

This work is supported through Semiconductor Research Corporation, Office of Naval Research and the Air Force Office of Scientific Research.

2.8 References

[1] G. D. Wilk, R. M. Wallace, J.M. Anthony, J. Appl. Phys. **89**, 5243 (2001)

[2] J. P. Chang, Y.-S. Lin, S. Berger, A. Kepten, R. Bloom, S. Levy, J. Vac. Sci. Technol. B **19**, 2137 (2001)

[3] E. P. Gusev, E. Cartier, D. A. Buchanan, M. Gribelyuk, M. Copel, H. Okorn-Schmidt, C. D'Emic, Microelec. Eng. **59**, 341 (2001)

[4] J. Robertson, J. Vac. Sci. Technol. B **18**,1785, (2000)
1
[5] J. P. Chang, Y.-S. Lin, Appl. Phys. Lett. **23**, 3824 (2001)

[6] M. Copel, M. Gribelyuk, E. Gusev, Appl. Phys. Lett. **76**, 436 (2000)

[7] S. Stemmer, Z. Chen, R. Kedling, J.-P. Maria, D. Wicaksana, A. I. Kingon, J. Appl. Phys. **92**, 82 (2002)

[8] S. Miyazaki, M. Narasaki, M. Ogasawara, M. Hirose, Microelec. Eng. **59**, 373 (2001)

[9] S. Miyazaki, M. Narasaki, M. Ogasawara, M. Hirose, Solid State Elec. **46**, 1679 (2002)

[10] C. Fulton, G. Lucovsky, R. J. Nemanich, J. Vac. Sci. Technol. B. **20**, 1726 (2002)

[11] A. C. Tuan, T. C. Kaspar, T. Droubay, J. W. Rogers Jr., S. A. Chambers, Appl. Phys. Lett. **83**, 3734 (2003)

[12] J. W. Kiester, J. E. Rowe, J. J. Kolodziej, H. Niimi, T. E. Madey, G. Lucovsky, J. Vac. Sci. Technol. B **17**, 1831 (1999)

[13] C. C. Fulton, G. Lucovsky, and R. J. Nemanich, Appl. Phys. Lett. **84**, 1 (2003)

[14] S. Stemmer, Z. Q. Chen, C. G. Levi, P. S. Lysaght, B. Foran, J. A. Gisby, J. R. Taylor, Jpn. J. Appl. Phys. Part 1 **42**, 3593 (2I 003)

[15] S. Stemmer, Z. Y. Li, B. Foran, P. S. Lysaght, S. K. Streiffer, P. Fuoss, S. Seifert, Appl. Phys. Lett. **83**, 3141 (2003)

[16] S. Ramanathan, P. C. McIntyre, J. Luning, P. S. Lysaght, Y. Yang, Z. Chen, S. Stemmer, J. Electrochem. Soc., **150**(10) F173 (2003)

[17] J.-P. Maria, D. Wicaksanam, A. I. Kingon, B. Busch, H. Schulte, E. Garfunkel, T. Gustafsson, J. Appl. Phys. **90**, 3476 (2001)

[18] C. M. Perkins, B. B. Triplett, P. C. McIntyre, K. C. Saraswat, E. Shero, Appl. Phys. Lett. **81**, 1417 (2002)

[19] G. Lucovsky, J.C. Phillips and M.F. Thorpe, in *Characterization and Metrology for ULSI Technology: 1998 International Conference*, ed. by D.G. Seiler, A.C. Diebold, W.M. Bullis, T.J. Shaffner, R. McDonald and E.J. Walters (The American Institute of Physics, Woodbury, NY 1998), p. 273.

[20] J. P. Chang, Y.-S. Lin, J. Appl. Phys. **90**, 2964 (2001).

[21] J.P. Chang, Y-S. Lin and C.K. Chu, J. Vac. Sci. Technol. B **19**, 1782 (2001).

Table 2.1: Tabulated XPS peak positions and UPS valence band data in binding energy relative to the Si E_F for ZrO_2 deposited on a 0.5 nm SiO_2 buffer layer. The valence band offset (VBO) includes band bending and the conduction band offset (CBO) includes the bandgap (9.0 eV for SiO_2 and 5.8 eV for ZrO_2).

Process Step	***Si 2p (Bulk)***	***Si 2p (SiO_2)***	***O 1s (SiO_2)***	***O 1s (ZrO_2)***	***Zr 3d (oxide)***	***Zr 3d (metallic)***	***VBM***	***BB***	***VBO***	***CBO***
SiO_2	99.65	103.3	532.5	n/a	n/a	n/a	5.2	0.0	4.3	3.7
0.3 nm	99.45	102.2	531.6	529.9	182.4	n/a	3.4	-0.2	2.3	2.4
0.6 nm	99.45	102.0	531.5	529.7	182.1	n/a	2.7	-0.2	1.6	3.1
1.2 nm	99.40	101.7	531.4	529.5	181.8	n/a	2.2	-0.3	1.1	3.6
2.4 nm	99.40	101.8	531.4	529.4	181.7	n/a	2.1	-0.3	0.9	3.8
3.5 nm	99.30	101.5	531.3	529.1	181.4	n/a	1.9	-0.4	0.7	4.0
600°C	99.50	103.1	532.5	531.2	183.8	n/a	4.6	-0.2	3.6	1.1
750°C	99.55	103.3	532.5	531.2	183.7	n/a	4.4	-0.1	3.4	1.3
900°C	99.45	n/a	n/a	n/a	n/a	179.1	0.0	-0.2	n/a	n/a

Table 2.2: Tabulated XPS peak positions and UPS valence band data in binding energy relative to the Si E_F for ZrO_2 deposited on a ~30 nm SiO_2 buffer layer.

Process Step	***Si 2p (Bulk)***	***Si 2p (SiO_2)***	***O 1s (SiO_2)***	***O 1s (ZrO_2)***	***Zr 3d (oxide)***	***Zr 3d (metallic)***
SiO_2	n/a	104.8	533.9	n/a	n/a	n/a
ZrO_2	n/a	104.3	533.5	531.6	183.9	n/a
600°C	n/a	104.0	533.2	531.6	183.8	n/a
750°C	n/a	104.0	533.1	531.5	183.7	n/a
900°C	n/a	104.0	533.2	531.3	184.0	n/a
Si	95.55	103.6	533.2	531.5	183.8	n/a
600°C	99.45	104.0	533.2	531.6	184.0	n/a
750°C	99.60	104.1	533.2	531.6	183.9	n/a
900°C	99.35	n/a	533.5	n/a	n/a	179.2

Table 2.3: Tabulated XPS peak positions and UPS valence band data in binding energy relative to the Si E_F for ZrO_2 deposited on a ~1 nm Si_3N_4 buffer layer. The VBO includes band bending and the CBO is not given as the bandgap values needed to calculate the CBO are not well defined in the presence of excess Si.

Process Step	***Si 2p (Bulk)***	***Si 2p (Si_3N_4)***	***O 1s (SiO_2)***	***O 1s (ZrO_2)***	***Zr 3d (oxide)***	***Zr 3d (metallic)***	***N 1s***	***BB***	***VBM***	***VBO***
Si_3N_4	99.75	102.3	532.2	n/a	n/a	n/a	397.8	0.1	n/a	n/a
ZrO_2	99.55	101.5	531.4	529.2	181.5	n/a	397.2	-0.1	2.1	1.1
600°C	99.70	102.3	n/a	530.9	183.2	n/a	397.6	0.0	4.0	3.1
750°C	99.85	102.4	n/a	530.9	183.2	n/a	397.8	0.2	4.1	3.3
900°C	99.80	102.4	n/a	530.9	183.2	n/a	397.5	0.1	4.0	3.2
Si	99.50	n/a	n/a	531.3	183.5	n/a	n/a	-0.2	0.4	n/a
600°C	99.60	102.8	n/a	531.4	183.6	n/a	397.7	-0.1	3.9	2.9
750°C	99.65	102.4	n/a	531.2	183.1	179.3	397.5	0.0	2.8	1.9
900°C	99.65	102.2	n/a	531.9	182.9	179.6	397.6	0.0	0.0	n/a

Table 2.4: Chemical reduction of $ZrSiO_4$ and ZrO_2 involving $SiO_{(g)}$ and $ZrO_{(g)}$ formation. The equilibrium pressures of $SiO_{(g)}$ and $ZrO_{(g)}$ are set at 0.01 Torr at all temperatures, and that $\Delta G_i^o = \Delta G_f^o + RT \ln P_i$ is used for the gaseous species. Values for ΔG are given in kcal/mol. for ZrO2 and ZrSiO4 decomposition.[5]

Reactions	**25°C**	**527°C**	**727°C**	**927°C**	**1127°C**
$ZrSiO_4 + 5Si \rightarrow 4SiO + ZrSi_2$	272	141	90	39	-10
$2ZrSiO_4 + 7Si \rightarrow ZrO + 7SiO + ZrSi_2$	620	358	256	155	54
$ZrSiO_4 \rightarrow SiO_2 + ZrO_2$	5	4	3	3	2
$SiO_2 + Si \rightarrow 2SiO$	130	65	40	15	-9
$2ZrO_2 + 5Si \rightarrow ZrO + 3SiO + ZrSi_2$	349	219	168	118	69

Figure Captions

Figure 2.1: XPS core level spectra of the O 1s transition for various thicknesses of the Zr oxide film on a 1.0 nm SiO_2 buffer layer.

Figure 2.2: XPS core level spectra of the Si 2p transition for various thicknesses of the Zr oxide film on a 1.0 nm SiO_2 buffer layer.

Figure 2.3: XPS core level spectra of the Si 2p transition for various thicknesses of the Zr oxide film on a 1.0 nm SiO_2 buffer layer (note the plot order is reversed with respect to Fig 1,2 for clarity).

Figure 2.4: The UPS valence band spectra for various thicknesses of the Zr oxide film on a 1.0 nm SiO_2 buffer layer.

Figure 2.5: The UPS valence band spectra for ZrO_2 on a thin SiO_2 buffer layer after different annealing temperatures. The shift from the as-grown 3.5 nm Zr oxide is large (> 2eV) when annealed to 600°C. There is a smaller shift to lover binding energy as the film is annealed to higher temperature (750°C). After the 900°C anneal emission is observed near E_F, indicating the film has a metallic like character. The relative intensity of each spectrum has been normalized for clarity.

Figure 2.6: XPS core level spectra of the (a) O 1s and the (b) Si 2p transitions for the as-grown 3.5 nm Zr oxide film and after 600, 750 and 900°C *in-situ* anneal. The O 1s peak has a large shift when annealed at 600°C then disappears after annealing at 900°C. The oxide related Si 2p (~102—103 eV) also shows a sizable shift when annealed to 600°C and also disappears after annealing to 900°C. The Si 2p bulk peak (~99 eV) becomes much more intense after the 900°C anneal.

Figure 2.7: XPS core level spectra of the (a) O 1s and the (b) oxide related Si 2p transitions from 3.0 nm Zr oxide deposited on 30 nm SiO_2.

Figure 2.8: XPS core level spectra of the (a) O 1s and the (b) Si 2p transitions from 3.0 nm Zr oxide deposited on 30 nm SiO_2 with a 2 nm Si cap. The oxide related features are hardly evident after the 900°C anneal.

Figure 2.9: Schematic diagram of the valence and conduction bands for the (a) as-grown and the (b) annealed state of the TM oxide film on a thin SiO_2 buffer layer. The valence band offset (ΔE_V) can change by up to ~2.5 eV with annealing. The depictions are (a) before *in-situ* annealing where excess oxygen near the ZrO_2–SiO_2 interface attracts electrons from the substrate, resulting in a potential across the SiO_2 buffer layer and (b) after *in-situ* annealing where the oxygen has diffused to vacuum, reducing the interface electronic states and the bands become flat.

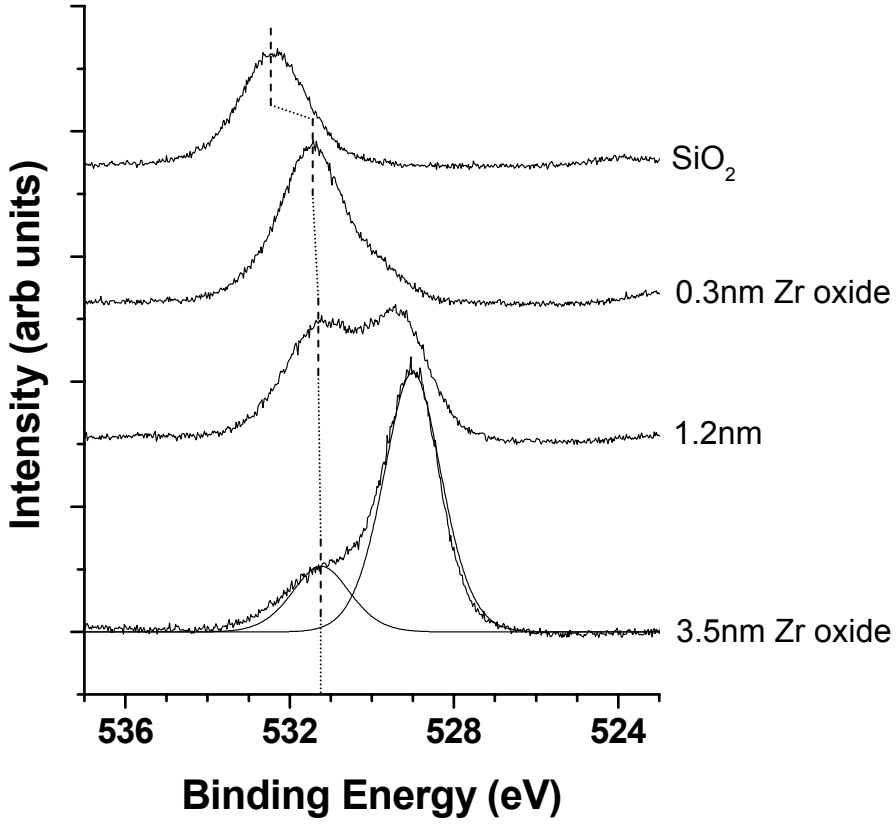

Figure 2.1: XPS core level spectra of the O 1s transition for various thicknesses of the Zr oxide film on a 1.0 nm SiO_2 buffer layer.

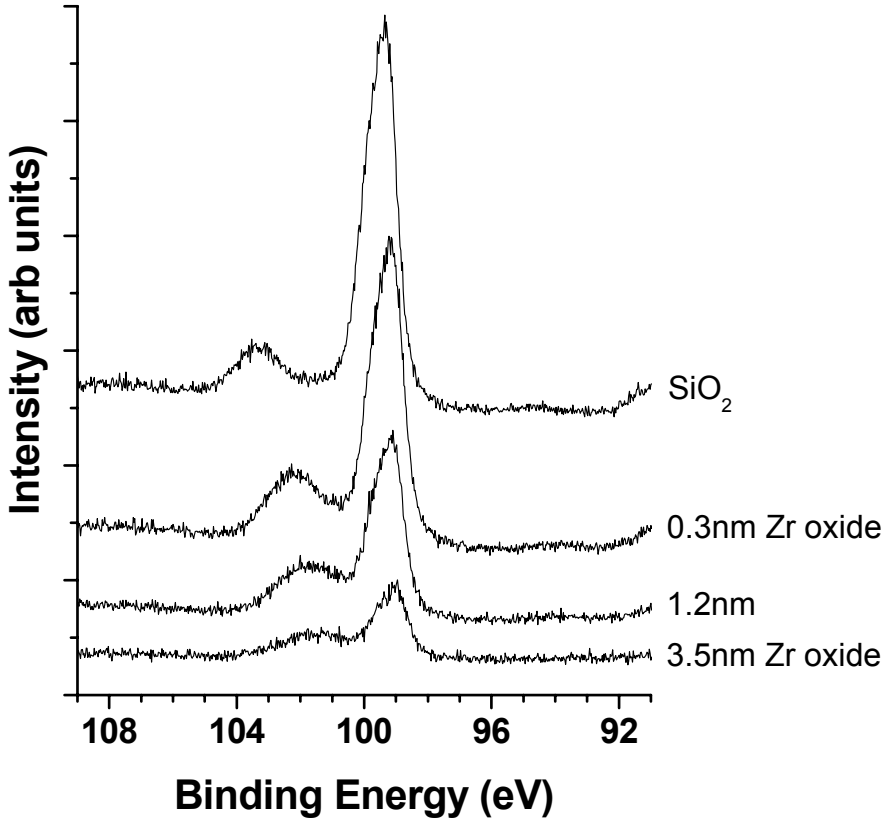

Figure 2.2: XPS core level spectra of the Si 2p transition for various thicknesses of the Zr oxide film on a 1.0 nm SiO_2 buffer layer.

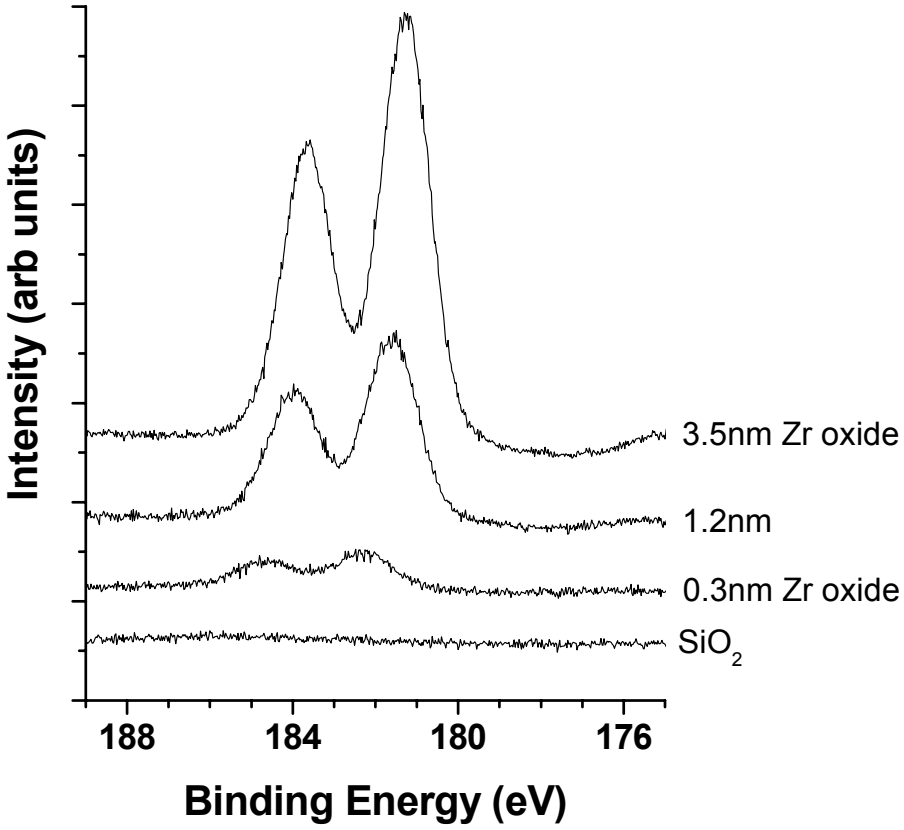

Figure 2.3: XPS core level spectra of the Si 2p transition for various thicknesses of the Zr oxide film on a 1.0 nm SiO_2 buffer layer (note the plot order is reversed with respect to Fig 1,2 for clarity).

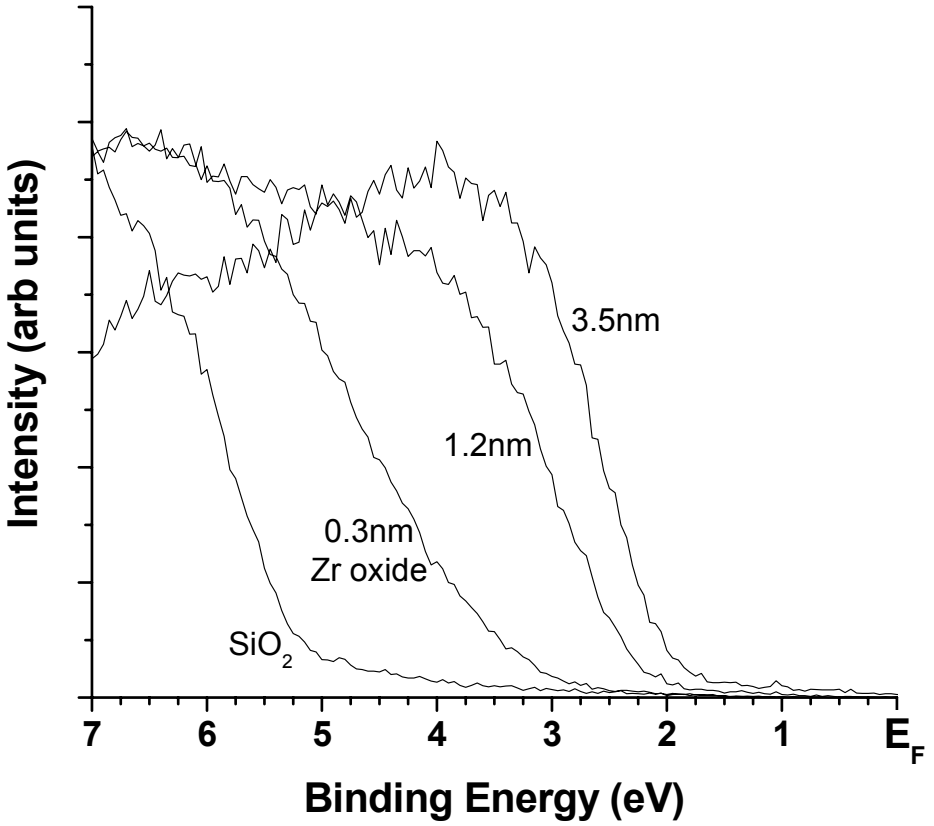

Figure 2.4: UPS valence band spectra for various thicknesses of the Zr oxide film on a 1.0 nm SiO_2 buffer layer.

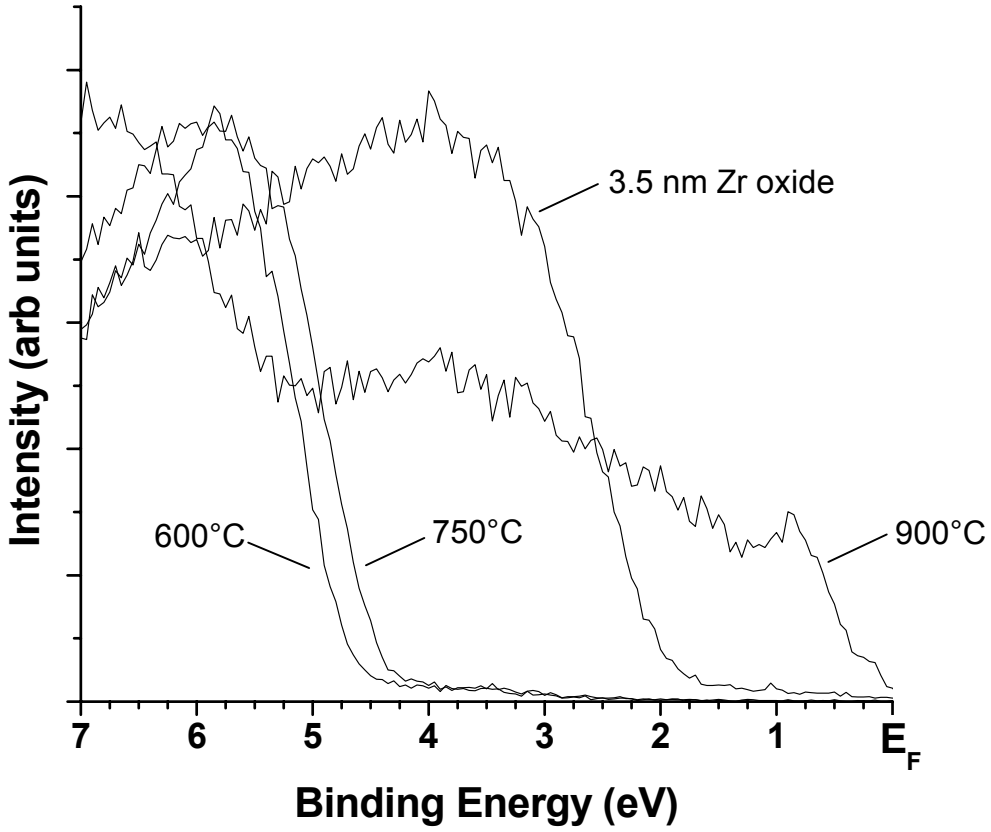

Figure 2.5: UPS valence band spectra for ZrO_2 on a thin SiO_2 buffer layer after different annealing temperatures. The shift from the as-grown 3.5 nm Zr oxide is large (> 2eV) when annealed to 600°C. There is a smaller shift to lover binding energy as the film is annealed to higher temperature (750°C). After the 900°C anneal emission is observed near E_F, indicating the film has a metallic like character. The relative intensity of each spectrum has been normalized for clarity.

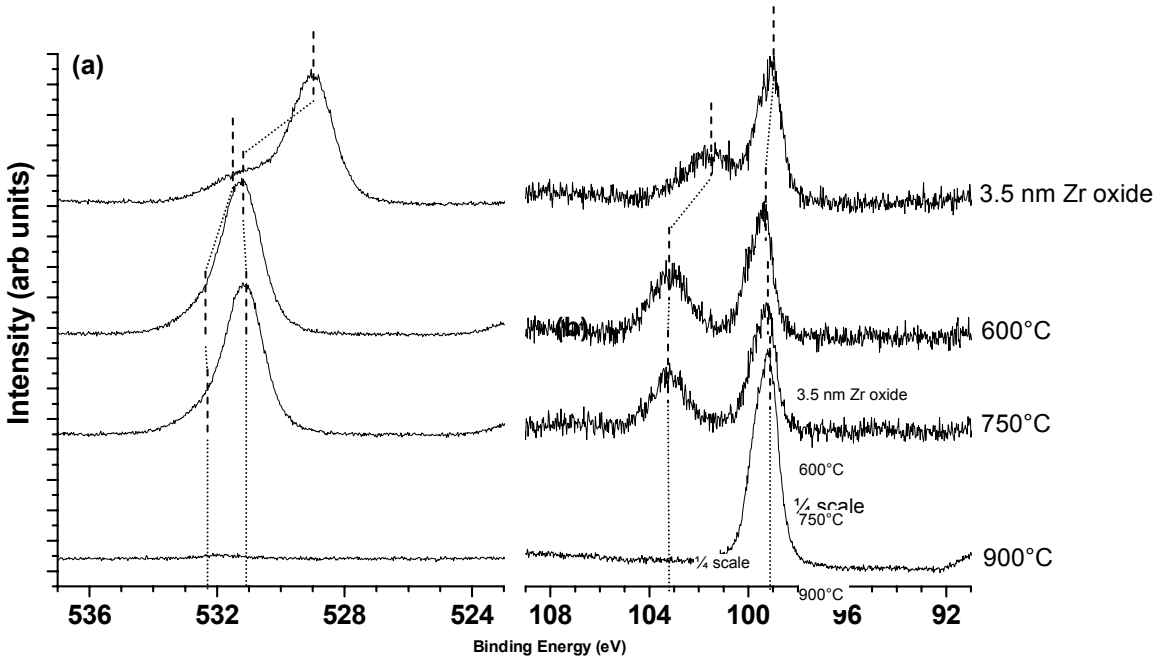

Figure 2.6: XPS core level spectra of the (a) O 1s and the (b) Si 2p transitions for the as-grown 3.5 nm Zr oxide film and after 600, 750 and 900°C *in-situ* anneal. The O 1s peak has a large shift when annealed at 600°C then disappears after annealing at 900°C. The oxide related Si 2p (~102—103 eV) also shows a sizable shift when annealed to 600°C and also disappears after annealing to 900°C. The Si 2p bulk peak (~99 eV) becomes much more intense after the 900°C anneal.

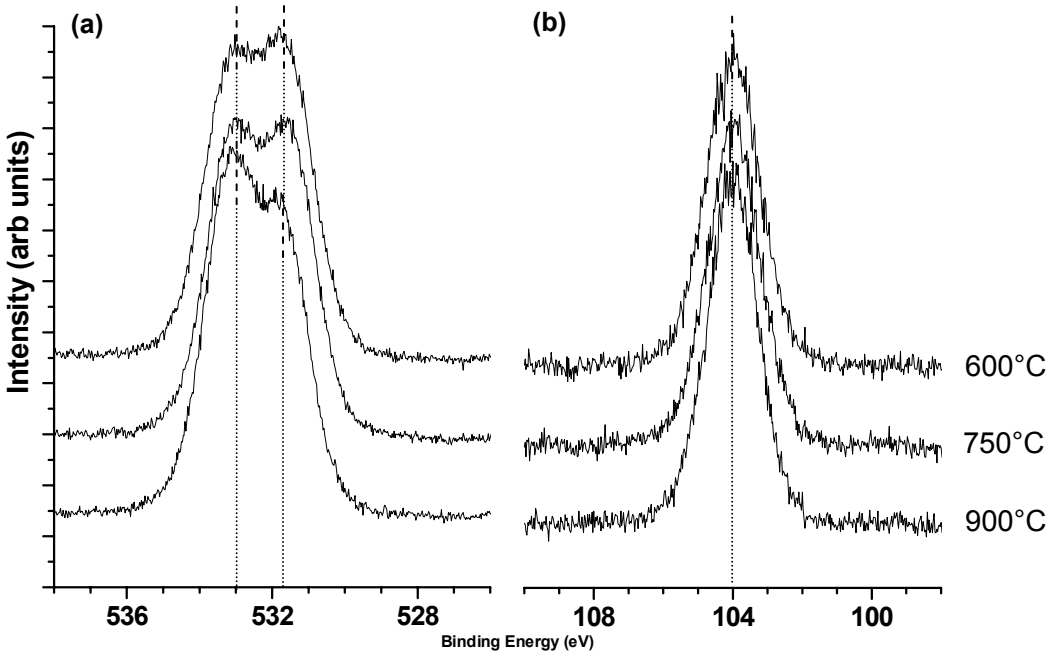

Figure 2.7: XPS core level spectra of the (a) O 1s and the (b) oxide related Si 2p transitions from 3.0 nm Zr oxide deposited on 30 nm SiO_2.

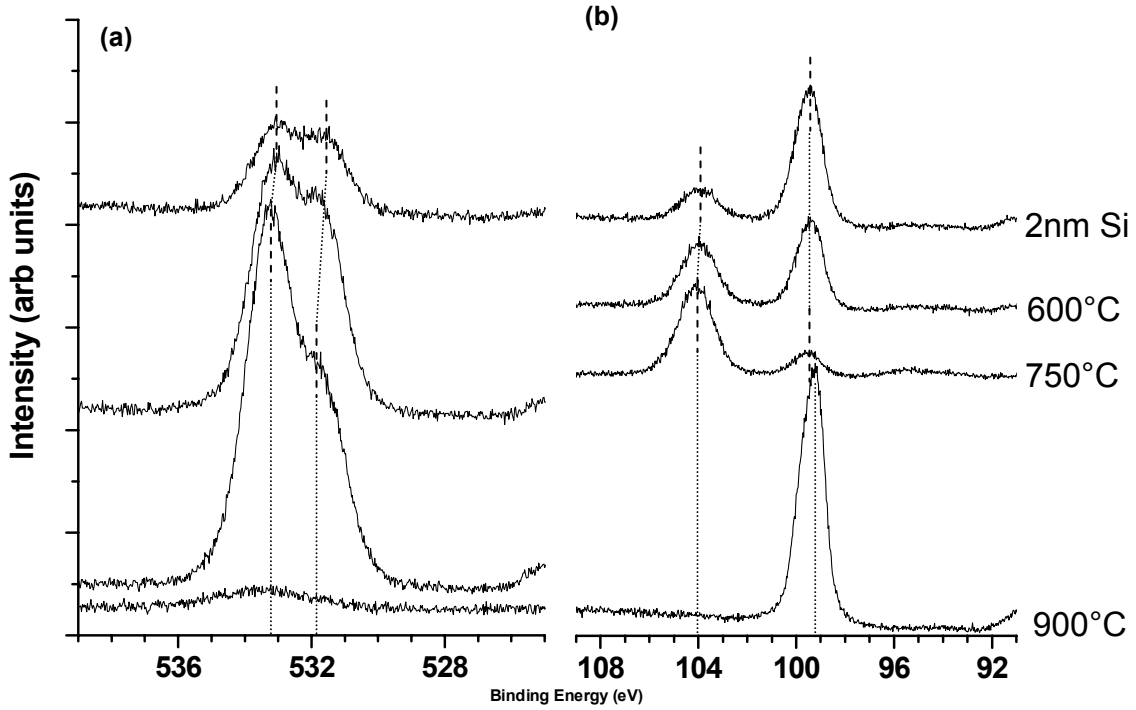

Figure 2.8: XPS core level spectra of the (a) O 1s and the (b) Si 2p transitions from 3.0 nm Zr oxide deposited on 30 nm SiO_2 with a 2 nm Si cap. The oxide related features are hardly evident after the 900°C anneal.

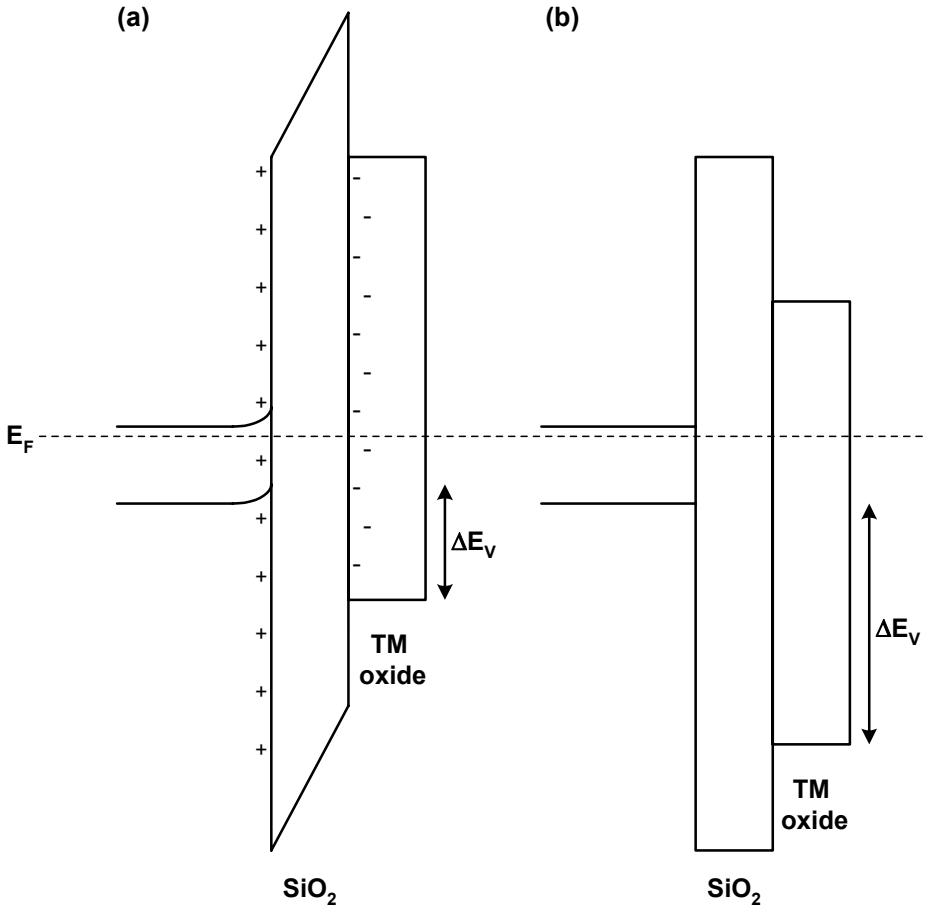

Figure 2.9: Schematic diagram of the valence and conduction bands for the (a) as-grown and the (b) annealed state of the TM oxide film on a thin SiO_2 buffer layer. The valence band offset (ΔE_V) can change by up to ~2.5 eV with annealing. The depictions are (a) before *in-situ* annealing where excess oxygen near the ZrO_2–SiO_2 interface attracts electrons from the substrate, resulting in a potential across the SiO_2 buffer layer and (b) after *in-situ* annealing where the oxygen has diffused to vacuum, reducing the interface electronic states and the bands become flat.

3. Process Dependent Band Structure Changes of Transition-metal (Ti, Zr, Hf) Oxides on Si (100)

C.C. Fulton
Department of Materials Science and Engineering
North Carolina State University
Raleigh, North Carolina 27695-7907

G. Lucovsky and R.J. Nemanich
Department of Physics
North Carolina State University
Raleigh, North Carolina 27695-8202

These results published in:

Applied Physics Letters
Vol. 84, No. 4, p580 (2004).

3. Process Dependent Band Structure Changes of Transition-metal (Ti, Zr, Hf) Oxides on Si (100)

3.1 Abstract

In this study we have deposited Ti, Zr and Hf oxides on ultra-thin (~0.5 nm) SiO_2 buffer layers and have identified metastable states which give rise to large changes in their band alignments with respect to the Si substrate. This results in a potential across the interfacial SiO_2 layer, significant band bending and large shifts of the high-k valence band. The magnitude of the shift differs for the three materials and is dependant on both the SiO_2 buffer layer thickness and annealing temperature. We propose a model where excess oxygen accumulates near the high-k–SiO_2 interface providing electronic states, which are available to electrons that tunnel from the substrate.

3.2 Introduction

The task of identifying a suitable replacement dielectric for high-performance, low-power devices is complex with many difficulties. Transition-metal (Tm) oxides have received much attention for their large dielectric constants and relatively large bandgaps. Zirconium and hafnium oxides, in particular, have been considered. Titanium oxides have also received attention but, due to their smaller bandgap, they have generally not received the same consideration as potential replacement dielectrics for field effect transistors (FETs).

The primary goal in choosing a replacement for SiO_2 is to reduce the tunneling current through the gate oxide of a FET while maintaining the channel charge density. There are two main parameters that effect tunneling current: 1) the physical thickness of the dielectric and 2) the barrier height or band offset with respect to Si. Choosing a high-k material with a large dielectric constant can solve the tunneling problem by increasing the dielectric thickness, but these materials often have barrier heights smaller than the traditional SiO_2 on Si, sometimes very much smaller. For instance, TiO_2 has essentially no barrier with respect to the Si conduction band, and electrons would be free to move from channel to gate, through the oxide.[1]

Understanding barrier heights and how they can be altered by different process conditions is a critical part of choosing a replacement dielectric material. In this letter we report an effect that can alter barrier heights by as much as 2.0 eV. We determine the circumstances where the effect occurs and propose a model to explain these large shifts in band structure.

3.3 Experiment

All experiments employed n-type 25mm diameter Si (100) wafers with phosphorous doping of ~$4x10^{18}$ cm^{-3}. The doping density is calculated from the lowest value in the resistivity range quoted from the manufacturer. All processing and characterization occurred in ultra-high vacuum (UHV) conditions. The Si wafers were prepared with an SiO_2 buffer layer by either remote plasma oxidation (RPO) or remote plasma enhanced chemical vapor deposition (REPCVD). In this study, Tm oxides were formed by electron beam evaporation of a metal (Ti, Zr or Hf) onto the SiO_2 buffer layer followed by remote plasma oxidation. The electronic states were then characterized with x-ray and ultraviolet photoelectron spectroscopy (XPS, UPS). A more detailed description of this approach has been presented previously.[1]

In characterizing the band offsets of the Tm as-deposited oxides on an SiO_2 buffer, we observed a large shift in the valence band turn-on and all of the oxide core levels when the films were annealed to 500°C. This effect was found to occur in Ti, Zr and Hf oxides, with ZrO_2 demonstrating the largest shift. Figure 1 shows UPS spectra for all three oxides in their as-grown state (solid lines) and in their annealed state (dotted). With annealing, the ZrO_2 VBM was shown to shift up to ~2.0 eV, while the HfO_2 and TiO_2 shifted by ~0.8 eV, depending on process conditions. Accounting for changes in band bending, we deduce the Si-high-k valence band offset (VBO) to be 1.65, 0.95 and 2.05 eV for the as-grown Ti, Zr and Hf oxides, respectively, and after annealing, the VBO increase to 2.55, 3.0 and 2.75 eV for the respective Ti, Zr and Hf oxides.

3.4 Results

We previously reported VBO of 2.2 eV for TiO_2 which falls between the shifted and annealed values we observe in this study,[1] and Campbell *et al*. found a VBO of 1.0 eV which is near the value of the as-deposited.[2,3] In a study of ZrO_2 on Si (100), Miyazaki *et al*., utilizing XPS, found a valence band offset of 3.2 eV,[4,5,6] which is in reasonable agreement with our measurements of the annealed film. Predictions made by Robertson using the charge neutrality model obtain a VBO of 2.0 and 3.3 eV for TiO_2 and ZrO_2, respectively.[7] For HfO_2 Robertson has noted that the charge neutrality model predicts VBO of 3.4 eV. Sayan *et al.* have used photoemission to measure the VBO of HfO_2 with respect to Si and found values between 3.03 and 3.63 eV,[8] which is in relative agreement with the predictions and our measurements. However, Yu *et al.* have found that their as-grown HfO_2 films showed a VBO of 2.22 eV,[9] which is similar to our observations of the as-grown state.

We have explored the origin of this effect through a process of re-exposing the annealed films to the remote plasma oxidation. As shown in Fig. 2 the VBM of the as-grown and re-oxidized spectra are essentially identical, as are the two annealed spectra. The core level spectra of the Tm oxide shifted in a similarly consistent way suggesting that the shifts are of electronic, not chemical, origin. Similar films were annealed and characterized in a stepwise fashion at temperatures of 200, 300, 400 and 500°C. The photoelectron spectra shifted gradually at low temperatures and shifted to a greater extent at higher temperatures.

The core levels of the Tm and the Tm oxide-related O 1s core level spectra showed similar shifts to the valence band. An interesting aspect was evident on examination of the SiO_2 related O 1s and Si 2p core levels. The core level spectra associated with the buffer layer shifted to a lesser degree than the Tm oxide core levels and the valence band spectra.

Figure 3 shows the O 1s spectra for an as-grown and annealed ZrO_2 film. The strongest spectral feature (at lower binding energy) is associated with the ZrO_2 which, upon annealing, shifted by a magnitude equal to that of the valence band maxima. The weaker feature, at slightly higher binding energy, is associated with the SiO_2 buffer layer, which shifted less than the ZrO_2 component.

We also explored how variations in the thickness of the SiO_2 buffer layer affect the changes in band structure. Buffer layers were prepared with thicknesses of 0.5, 2.0 and 3.5 nm followed by the deposition of 1.2 nm of HfO_2. Valence band and core level spectra were recorded, and the shift between the as-grown and annealed states was measured. For the 0.5 nm buffer layer a VB shift of 1.50 eV was measured. The shifts in the core levels and valence band decreases as the buffer layer thickness is increased. Increasing the thickness of the buffer to 2.0 nm resulted in a 1.35 eV shift. A further increase in buffer layer thickness to 3.5 nm resulted in a VB shift of 0.20 eV.

3.5 Discussion

We suggest that the exposure to a remote oxygen plasma (and a high concentration of atomic oxygen) introduces excess oxygen into the high-k material and that this oxygen is in a metastable state where annealing can apparently drive out the excess.

On first examination one might suggest that an interface dipole has formed at the Si–buffer layer interface. However, such a dipole would shift the entire band structure equally, meaning that the SiO_2 and ZrO_2 electronic states would shift by the same magnitude and direction. This was not the observed case; instead the spectra associated with the SiO_2 buffer layer and Tm oxide shifted in the same direction but by a different magnitude, suggesting that there is a potential drop across the buffer layer. We propose that excess negative charge

is present near the high-k–SiO_2 interface and that there is consequently a potential across the buffer oxide, between the substrate and the charge layer in the high-k material. Fig. 4 (a) displays a schematic of the bands of the as-grown film with excess charge at the high-k interface and a potential across the buffer layer, and Fig. 4(b) shows the annealed state with flat bands, no excess charge and no potential over the buffer layer.

Fissel *et al.* have noted similar core level shifts for PrO_2 on Si and have suggested a model, which assumes no interfacial layer of SiO_2 and an epitaxial oxide on the Si substrate.[10] In our case, with the purposeful formation of an interfacial oxide, it is unlikely that our Tm oxides are epitaxial nor is our growth method conducive to forming single crystal oxides. As such, we must explore other possibilities in explaining our observations.

Our results indicate that the total electronic shift falls off as a function of increasing buffer layer thickness; approaching zero as the buffer layer grows past 3.5 nm. If the charge were constant near the interface then the potential difference across the buffer layer would increase with buffer layer thickness. This is not the observed case, and, in fact, the decreasing potential suggests that the amount of charge decreases with increasing buffer layer thickness. We propose that the charge layer is controlled by a tunneling process from the substrate.

The tunneling probability of an electron through SiO_2 falls off exponentially, with the probability becoming small after 3 to 4 nm thickness. We suggest that electrons tunnel from the substrate, though the buffer layer, to satisfy the electronic properties of the excess oxygen in the high-k material. The Tm oxides, ZrO_2 in particular, are known to be ionic conductors where the majority ion (oxygen) may move with relative ease[11]. We suggest the following as a possible scenario: oxygen diffuses into the high-k dielectric and electrons tunnel from the

substrate, through the SiO_2 buffer layer to satisfy the electronic states of the excess oxygen. This results in a potential across the buffer oxide and a shift in the band structure of the high-k material. When the source of oxygen is removed, the oxygen diffuses from the interface and escapes to vacuum. This diffusion of oxygen can be accelerated with annealing.

To estimate the charge needed to produce the measured shifts we treat the buffer layer as a simple dielectric filled capacitor with thickness of d = 2.0 nm, a dielectric constant of k = 3.9 for SiO_2 and a voltage of V = 1.0 V. From this we determine a charge density of $\sim 1 \cdot 10^{13}$ cm^{-2}. We can likewise estimate the positive charge in the Si from the change in band bending at the Si substrate. We use $N_s = \sqrt{2k\varepsilon_0 N_D V / q}$ to calculate the charge density, where N_s is the surface charge density, $N_D = \sim 4 \cdot 10^{18}$ cm^{-3} is the bulk doping density of the Si, q is the charge of an electron, ε_0 is the permittivity of free space, k = 12 is the dielectric constant of Si, and V = 0.3 V is the change in band bending. This gives a charge density of $N_s = 4 \cdot 10^{12}$ cm^{-2}. The charge may not be completely localized at the high-k–SiO_2 interface or other conditions may exist to explain the discrepancy in the two calculations.

3.6 Conclusions

This study has demonstrated that the electronic structure of the Tm oxide – SiO_2 interfaces can be significantly influenced by process conditions. The excess oxygen state of this interface is metastable would certainly lead to time dependent device characteristics. It remains to be seen whether processing approaches could be employed to improve device characteristics. Correlated interface and device studies may be able to quantify the effect of the charge layers and internal fields.

3.7 Acknowledgements

This work is supported through Semiconductor Research Corporation, Office of Naval Research and Air Force Office of Scientific Research.

3.8 References

[1] C.C. Fulton, G. Lucovsky, and R.J. Nemanich, J. Vac. Sci. Technol. B **20**, 1726(2002).

[2] S. A. Campbell, D. C. Gilmer, X. Wang, M. T. Hsich, H. S. Kim, W. L.Gladfelter, and J. H. Yan, IEEE Trans. Electron Devices **44**, 104(1997).

[3] S.A. Campbell, H.S. Kim, D.C. Gilmer, B. He, T. Ma, and W.L. Gladfelter, IBM J. Res. Develop. **43**, 383 (1999).

[4] S. Miyazaki, J. Vac. Sci. Technol. B **19**, 1071(2001).

[5] S. Miyazaki, M. Narasaki, M. Ogasawaga, and M. Hirose, Solid State Elect. **46**, 1679 (2002).

[6] S. Miyazaki, M. Narasaki, M. Ogasawaga, and M. Hirose, Microelect. Eng. **59**, 373 (2001).

[7] J. Robertson, J. Vac. Sci. Technol. B **18**,1785, (2000).

[8] S. Sayan, E. Garfunkel, and S. Suzer, Appl. Phys. Lett. **80**, 2135, (2002).

[9] H.Y. Yu, M.F. Li, B.J. Cho, C.C Yeo, M.S. Joo, D.-L. Kwong, J.S. Pan, C.H Ang, J.Z. Zheng, and S. Ramanathan, Appl. Phys. Lett. **81**, 376, (2002).

[10] A. Fissel, J. Dabrowski, and H.J. Osten, J. Appl. Phys. **91**, 8986, (2002).

[11] RV.S. Stubican, G.S. Corman, J.R. Hellmann, and G. Senft, Science and Technology of Zirconia II, Edited by N. Claussen, M. Rühle and A.H. Heuer, Advances in Ceramics **Vol. 12**, (Am. Ceram. Soc., Columbus, OH, 1984), p. 96–106.

Figure Captions

Figure 3.1: UPS valence band spectra for Ti, Zr and Hf oxides with an SiO_2 buffer layer on Si. Solid lines indicate the as-grown state; dotted lines indicate the annealed state.

Figure 3.2: UPS spectra of a ZrO_2 film with an SiO_2 buffer layer on Si. The spectra were obtained a) as grown, b) 500°C anneal, c) re-oxidized and d) second 500°C anneal.

Figure 3.3: XPS O 1s core level of an as-grown and annealed ZrO_2 film with an SiO_2 buffer on Si. The larger peaks are associated with the ZrO_2 layer and the smaller peaks with the buried SiO_2 buffer layer. The shifts on annealing (arrows) are larger for the ZrO_2 than the SiO_2 buffer layer.

Figure 3.4: Schematic diagram of the as-grown (a) and annealed (b) state: (a) excess oxygen near the Tm oxide–SiO_2 interface attracts electrons from the substrate, resulting in a potential across the SiO_2 buffer layer; (b) the oxygen diffuses to vacuum, there are no interface electronic states and the bands become flat. The valence band offset (ΔE_V) can change by up to 2.0 eV with annealing.

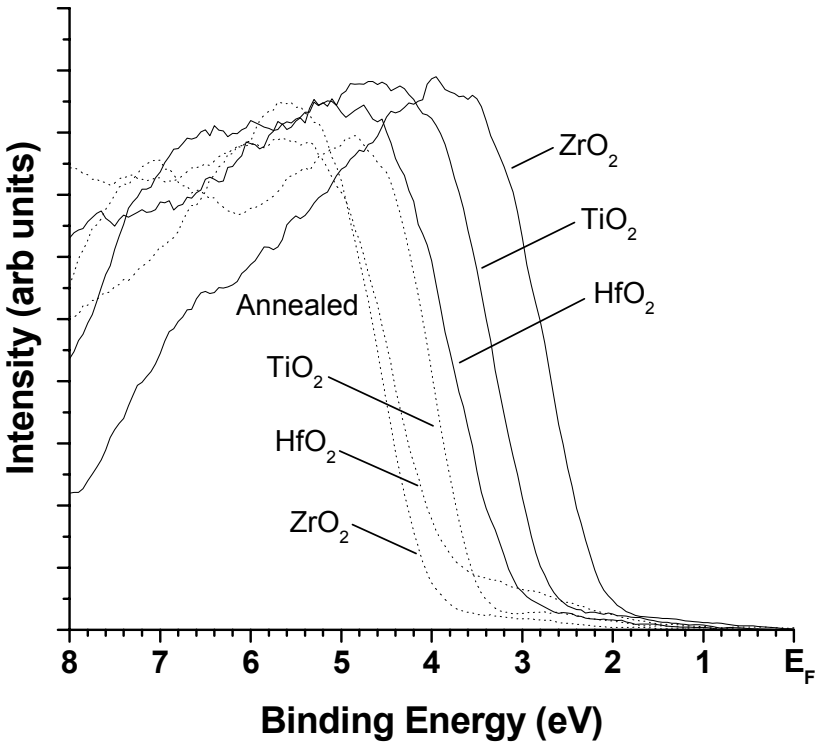

Figure 3.1: UPS valence band spectra for Ti, Zr and Hf oxides with an SiO_2 buffer layer on Si. Solid lines indicate the as-grown state; dotted lines indicate the annealed state.

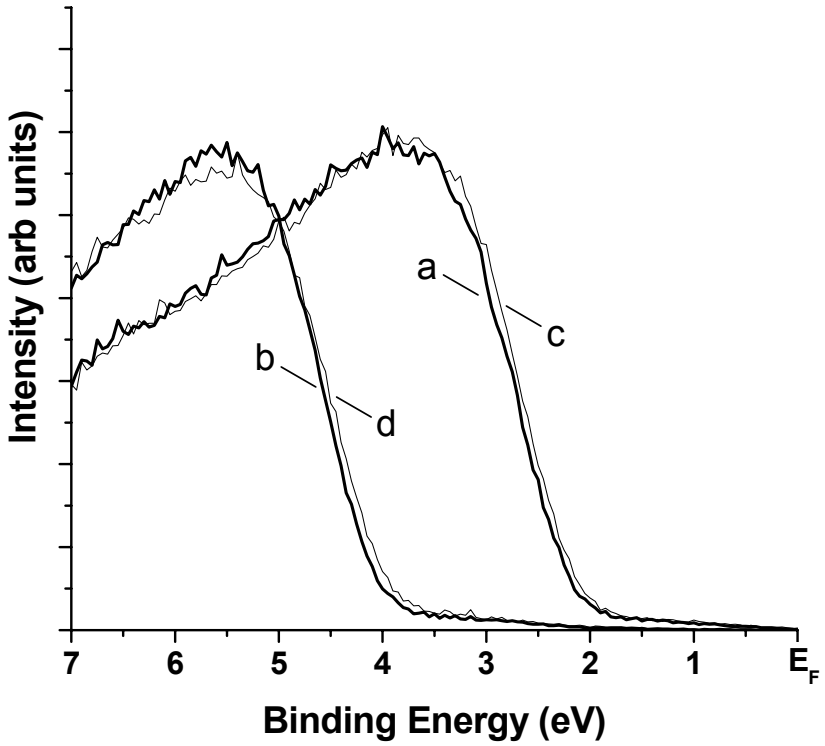

Figure 3.2: UPS spectra of a ZrO_2 film with an SiO_2 buffer layer on Si. The spectra were obtained a) as grown, b) 500°C anneal, c) re-oxidized and d) second 500°C anneal.

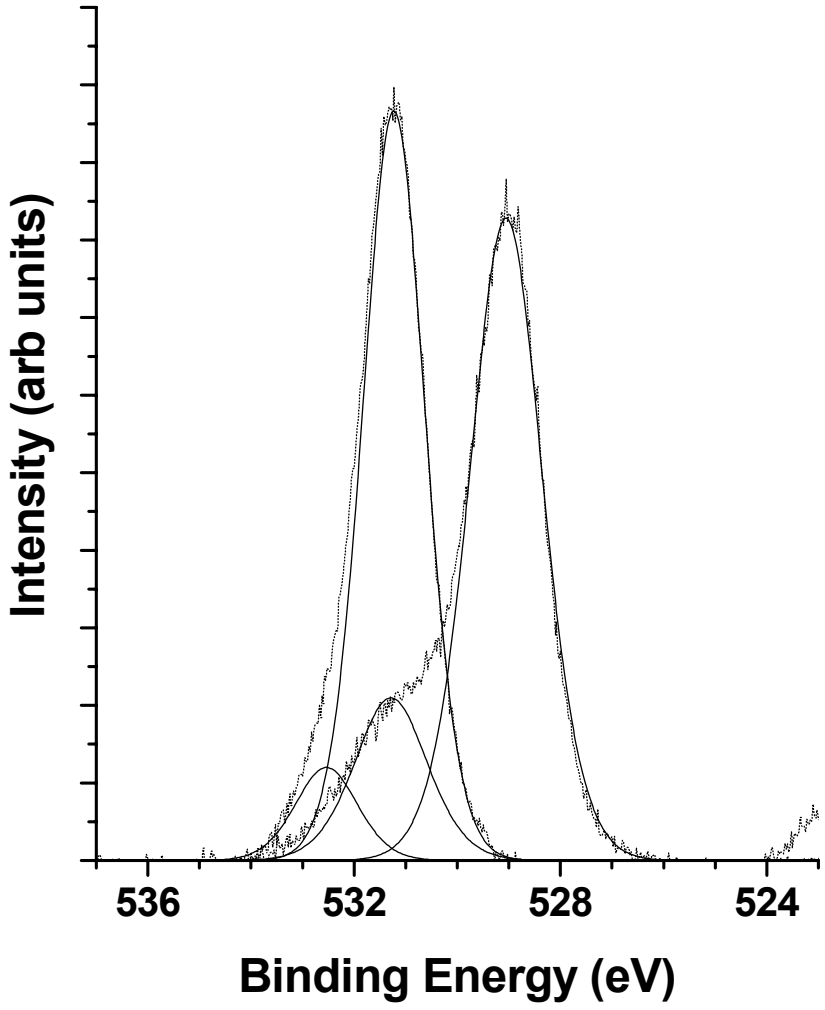

Figure 3.3: XPS O 1s core level of an as-grown and annealed ZrO_2 film with an SiO_2 buffer on Si. The larger peaks are associated with the ZrO_2 layer and the smaller peaks with the buried SiO_2 buffer layer. The shifts on annealing (arrows) are larger for the ZrO_2 than the SiO_2 buffer layer.

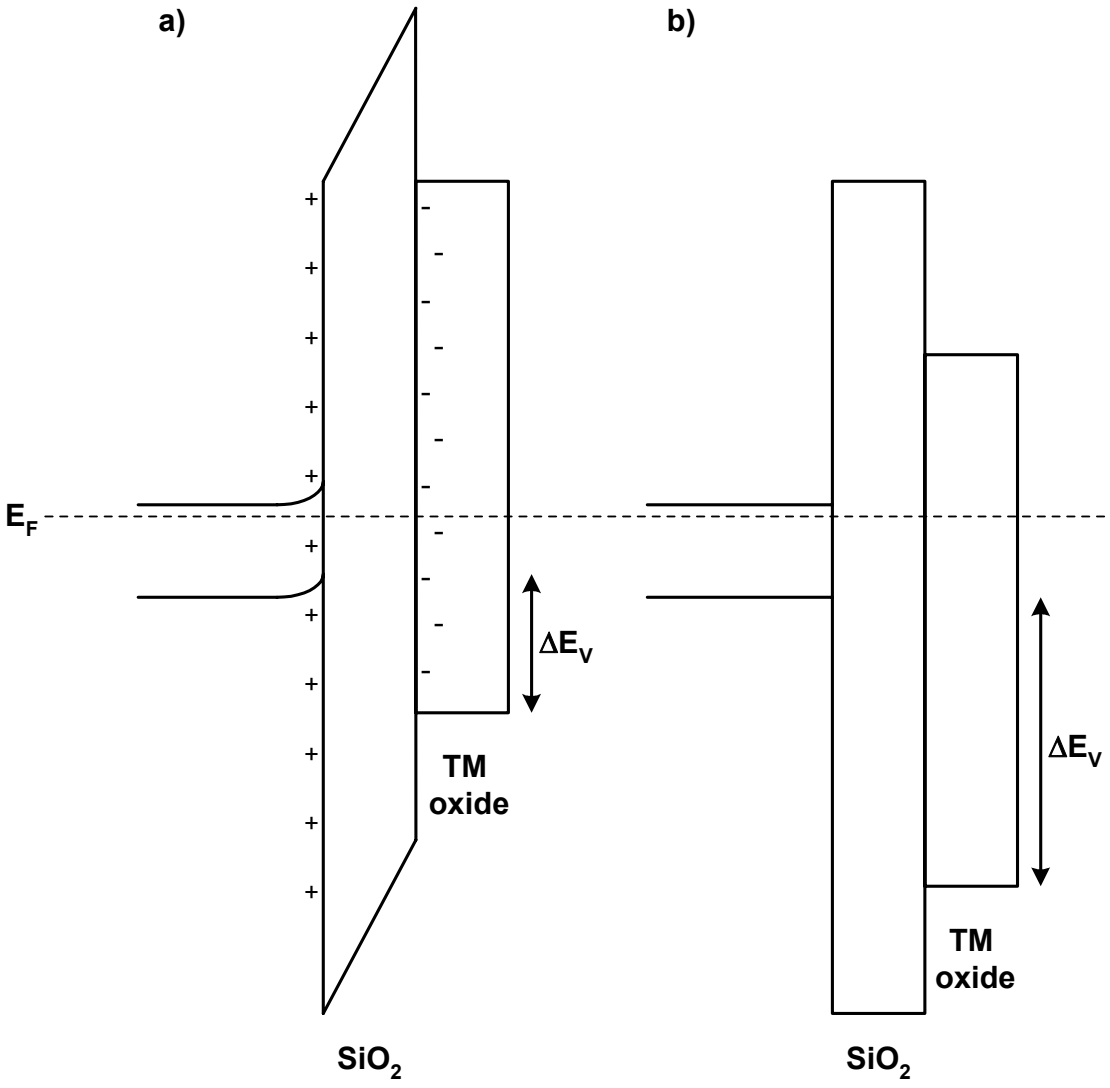

Figure 3.4: Schematic diagram of the as-grown (a) and annealed (b) state: (a) excess oxygen near the Tm oxide–SiO_2 interface attracts electrons from the substrate, resulting in a potential across the SiO_2 buffer layer; (b) the oxygen diffuses to vacuum, there are no interface electronic states and the bands become flat. The valence band offset (ΔE_V) can change by up to 2.0 eV with annealing.

4. Band Edge Electronic Structure of Transition Metal / Rare Earth Oxide Dielectrics

C.C. Fulton
Department of Materials Science and Engineering
North Carolina State University
Raleigh, North Carolina 27695-7907

C.L. Hinkle, N. Stoute, B.-S. Ju, C. Krug, H. Ade, D.E. Aspnes G. Lucovsky and R.J. Nemanich
Department of Physics
North Carolina State University
Raleigh, North Carolina 27695-8202

Y. Zhang, J. Whitten
Department of Chemistry
North Carolina State University
Raleigh, North Carolina 27695-5079

B.R. Rogers
Department of Chemical Engineering
Vanderbilt University
Nashville, Tennessee 37235-1604

J. Lüning
Stanford Synchrotron Research Laboratory
Menlo Park, California, 94025

S. Zollner, D. Tyrioso
Freescale Semiconductor, Inc
Austin, Texas, 78721

These results published in:

Rare Earth Oxide Thin Films: Growth, Characterization and Application
Ed. Marco Fanciulli and Giovanna Scarel
Springer-Verlag, Berlin (2005)

4. Band Edge Electronic Structure of Transition Metal/Rare Earth Oxide Dielectrics

4.1 Abstract

This chapter discusses band edge electronic structure of i) nanocrystalline elemental and complex oxide high-k dielectrics, and ii) non-crystalline Zr and Hf silicates, and Si oxynitride alloys. Experimental approaches include X-ray absorption spectroscopy, photoconductivity, and visible/vacuum ultra-violet and spectroscopic ellipsomentry (SE). These measurements are complemented by Fourier transform infra-red absorption, x-ray photoelectron spectroscopy, high resolution transmission electron microscopy, and x-ray diffraction. Three issues are highlighted: Jahn-Teller term-splittings that remove band edge d-state degeneracies in nanocrystalline films, intrinsic bonding defects in ZrO_2 and HfO_2, and chemical phase separation and crystallinity in Zr and Hf silicate and Si oxyntride alloys.

4.2 Introduction

Transition metal (TM) and lanthanide series rare earth (RE) oxides are being considered as alternative gate dielectrics for advanced semiconductor devices. The electronic states at the conduction band edges of these oxide dielectrics play a significant role in their performance and reliability of high-k gate stacks for Si complementary metal oxide semiconductor (CMOS) devices. This chapter presents spectroscopic studies that identify the contribution of TM and RE atom d-states to the conduction band edge electronic structure of nanocrystalline elemental and complex oxides, and non-crystalline TM silicate and TM Si oxynitride alloys. These studies are extended to include intrinsic bonding defects at well.

The first two sections of this chapter address respectively with the band edge electronic states in nanocrystalline TM/RE elemental, and TM/RE complex oxides. These have been studied primarily by two complementary spectroscopic techniques: i) x-ray absorption spectroscopy (XAS), in particular XANES,[1] x-ray absorption near edge spectroscopy to distinguish it from EXAFS, extended x-ray absorption fine structure in which x-ray energies extend well beyond the range of electronic transitions that terminate in conduction band states, and ii) vacuum ultra-violet spectroscopic ellipsometry, VUV SE.[2] These measurements have been complemented by other spectroscopic techniques as well including photoconductivity (PC),[3] and Fourier transform infra red spectroscopy (FTIR).

The next section of the chapter deals with intrinsic bonding defects, initially in the elemental oxides ZrO_2 and HfO_2, and then extended to complex oxides as well. Spectroscopic measurements, XANES and VUV SE, and PC, are used to first identify localized *defect states* approximately 0.6±0.2 eV below the conduction band edges of HfO_2 and ZrO_2.[2,3] This state is assigned to a grain- boundary bonding distortion. A second intrinsic

defect state has also been identified by XANES and VUV SE. It is localized within the band gap of ZrO_2, and approximately 4.2±0.15 eV above the valence band edge, or equivalently, 1.4±0.15 eV below the conduction band edge and is assigned to an oxygen atom vacancy[4]. There is no experimental evidence for a defect state lower in the band gaps of HfO_2 and ZrO_2, at ~3.3 eV above the valence band edge, that has been predicted by theoretical studies of hydrogen incorporation in semiconductors and insulators.[5] This section of the chapter includes results of electrical measurements that reveal the grain-boundary, and oxygen atom vacancy defects.

The final portion of this chapter addresses non-crystalline silicate alloys, where the emphasis is on the chemically stability of these films at the temperatures required for process integration into device structures. This chapter discusses non-crystalline Zr and Hf silicate pseudo-binary and pseudo-ternary alloys. It identifies ways in which chemical phase separation, CPS, and crystallization of the TM oxide chemically-separated phases may be effectively eliminated in pseudo-ternary alloys such as $Zr(Hf)O_2$-SiO_2-Si_3N_4, provided that alloy compositions are controlled within relatively narrow limits. Proceeding in this way, it is possible to extend EOT scaling to about 0.8 nm, while retaining the ability to use polycrystalline Si, or Si-Ge gate electrodes.

4.3 Experimental methods

The thin film samples for these studies were prepared by deposition techniques summarized in Ref. 1. These include remote plasma-assisted chemical vapor deposition (RPECVD) for the TM elemental oxides, and reactive evaporation for the TM elemental and TM/RE complex oxides. These TM/RE oxide films are either nanocrystalline as-deposited, or have been annealed at relatively low temperatures, up to 500°C in inert ambients sufficient

to release water, OH or hydrocarbons that impede the formation of nanocrystallites. Nanocrystallinity has been confirmed for these, or similarly prepared samples, by x-ray and/or electron diffraction, and/or infra-red absorption.

XAS measurements were made at the National Synchrotron Light Source (NSLS) at Brookhaven National Laboratory (BNL), and the Stanford Synchrotron Research Laboratory (SSRL) at the Stanford Linear Accelerator Center (SLAC). The SE, XPS, FTIR, HRTEM and XRD measurements were made on conventional and advanced.

4.4 Experimental results and discussion

4.4.1 TM elemental oxides

In presenting and discussing the XANES results, a distinction is made between i) *crystal field* (C-F) d-state term splittings in *highly symmetric* bonding environments which preserve the two-and three-fold degeneracies of the respective E_g and T_{2g} d-states, and ii) *Jahn-Teller* (J-T) d-state term-splittings, which are also a C-F splitting, but in *lower symmetry distorted environments* that remove the respective E_g and T_{2g} d-state degeneracies, either partially, or completely.[6] The J-T designation is used to emphasize a contributing mechanism for these bonding distortions.

To clarify the differences been C-F d-state splittings that preserve E_g and T_{2g} d-state degeneracies and J-T term splitting that remove these degeneracies, XANES spectra are presented for Zr silicate alloys as-deposited and after a 900°C anneal in Ar. C-F splittings in two-fold degenerate E_g and three-fold degenerate T_{2g} states are observed in as-deposited non-crystalline Zr and Hf silicate alloy thin films, and representative O K_1 edge spectra for Zr silicate alloys with ~30% and 60% ZrO_2 are presented in Fig. 1(a) and 1(b). There is no evidence in the absorption spectra, or in the derivative of the 30% alloy spectrum (or 60%

alloy, spectrum, not shown) for any additional d-state splittings indicative of a removal of the E_g d-state degeneracy. However after a 900°C inert ambient anneal in Ar, the O K_1 spectrum in Fig. 1(b) for the 60% alloy displays changes in the lower energy 4d-state in spectral line-width and energy (an ~0.5 eV *red-shift*) with respect to the as-deposited film in Fig. 1(a) that are indicative of d-state degeneracy removal. This is attributed to chemical phase separation (CPS) of this alloy into i) crystalline ZrO_2 with a J-T bonding distortion, and ii) non-crystalline SiO_2.[1] Bonding changes in pseudo-binary Zr silicate films, and in pseudo-ternary Zr and Hf Si oxynitrides will be addressed in more detail in section 4.

J-T term splittings are now addressed for nanocrystalline films of the group IVB TM oxides, TiO_2, and ZrO_2 and HfO_2. The bonding coordination of Ti is 6-fold in TiO_2, while it is typically 8- (and sometimes 7-) fold in ZrO_2 and HfO_2. This difference is responsible for qualitative differences between the corresponding spectra of i) TiO_2, and ii) ZrO_2 and HfO_2. Figures 2(a), (b) and (c) display respectively, in (a) the Ti $L_{2,3}$ XANES spectrum, (b) L_3 edge spectrum of TiO_2, and (c) the O K_1 edge spectrum. The $L_{2,3}$ spectrum is *intra-atomic* with transitions originating in occupied and spin-orbit split Ti 2p levels, and terminating in empty Ti 3d and 4s states. The separation between *equivalent features* the L_3 and L_2 features is the 2p state spin-orbit splitting. There are three features in the L_3 and L_2 spectra, the two lower energy ones are associated with transitions to 3d states, and show additional J-T term splittings, and the third and broader feature is associated with the 4s state. Figure 2(b) displays five distinct d-state features in the L_3 spectrum, consistent with a complete removal of T_{2g} (or $d_{5/2}$), and E_g (or $d_{3/2}$) degeneracies. The lower energy T_{2g} triplet displays two freatures with equal splittings of 0.75±0.3 eV, and the higher energy E_g doublet has a splitting of 0.8±0.2 eV. The 3d-state splitting between the average T_{2g} and E_g energies is

2.2±0.2 eV. Differences between the L_3 and L_2 spectra are due to symmetry-driven matrix element effects, and are beyond the scope of this review.

Figure 2(c) displays the O K_1 spectrum for TiO_2. Only two 3d state features are evident, and their energy separation is 2.7±0.1 eV. This 3d state separation is larger than *empty* 3d state splitting by ~0.5 eV. There is no evidence for any J-T term splitting of these d-state features in the O K_1 spectrum, or in a numerical differentiation of that spectrum. The final states in the O K_1 spectrum are molecular orbital anti-bonding O 2p states that are mixed with the Ti 3d and 4s states. The energy d-state differences with respect to the L_3 edge reflect this mixing, and are a result of solid state, band structure effects.

The XANES spectra are now compared with the conduction band edge spectra obtained from the VUV SE studies.[2] Figures 3(a) and (b) display respectively in (a) the imaginary part of the complex constant, ε_2, where $\varepsilon_c = \varepsilon_1+i\varepsilon_2$, and in (b) the absorption constant, α. Differentiation of the ε_2 spectrum indicates five d-state features. Their energies are compared to the five d-state features in the L_3 edge in Fig. 3(c). The slope of this plot is 1.1, and indicates an excellent correspondence between the empty state energies of the L_3 edge, and the d-state energies in the conduction band. The final point evident in a comparison between Fig. 3(b) and Fig. 2(b), is the strong matrix element effects for the d-state transitions. The lowest energy band edge transition at 3.2 eV is very weak in ε_2 and α, and also in the L_3 edge. This means the onset of strong absorption occurs at an energy about 1 eV greater than the threshold absorption. This is reflected in the photoconductivity edge spectrum in Fig. 3(d).

There are important qualitative differences between the corresponding XANES, VUV SE and PC spectra of TiO_2, and both ZrO_2 and HfO_2. These are first illustrated for ZrO_2, and

then summarized more briefly for HfO_2. Figures 4(a) and (b) display respectively in (a) the Zr $M_{2,3}$ spectra for transitions for Zr spin orbit split 3p states to empty Zr 4d and 5s states, and in (b) the O K_1 edge. In contrast to TiO_2, d-state term-splittings are not detectable in the respective XANES $M_{2,3}$ transitions in for ZrO_2 due to the short core hole lifetimes associated with the higher Z values of 40 Zr, and 22 for Ti, but are observable in the ZrO_2 O K_1 spectra through numerical differentiation. The average 4d state splitting for ZrO_2 has been obtained by deconvolving the spectra in Fig. 4(a), and is 2.3±0.2 eV. After differentiation, the average d-state splittings in the O K_1 edge in Fig. 4(b) are 3.3±0.2 eV. The differences between these energy separations are attributed to differences for transitions to empty atomic states in the $M_{2,3}$ edge, and molecular orbital states for the O K_1 edge.

Figures 5(a), (b) and (c) are respectively (a) ε_2, (b) α and (c) the PC response for ZrO_2. Three 4d-state features are evident in both ε_2 and α, the two E_g states, and lowest T_{2g} state. Their energy separations are in good quantitative agreement with the corresponding separations in the O K_1 edge. In ε_2, the E_g splitting is 0.9±0.2 eV, and the energy separation between the lower E_g state and the lowest T_{2g} state is 2.3±0.2 eV, compared with 1.0±0.2 eV, and 2.6±0.3 eV in the O K_1 edge. The threshold for strong absorption is correlated with the first d-state feature in α, and in the PC spectrum. This threshold energy defines an effective optical band gap of ~ 5.6±0.1 eV. Weak features at energies below this effective optical band gap, and extending to about 5.0 eV are addressed in the section r that deals with intrinsic defect states.

The core hole lifetime in HfO_2 for 4p to 5d and 6s transitions is shorter than it is for ZrO_2, since Z has increased to 70. The $N_{2,3}$ spectra show a single 5d state feature with no structure that can be extracted by differentiation. Figures 6(a), (b), (c) and (d) display

respectively in (a) O K_1, (b) ε_2, (c) α and (d) PC spectra for HfO_2. Differentiation of the O K_1 spectra yields five d-state energies, the lower two corresponding to the E_g states, and the upper three the T_{2g} states. The E_g separation is 1.0±0.2 eV, and the lower E_g state and the lowest T_{2g} state separation is 3.0±0.3 eV. The average 5d-state splitting is increased to 4.6±0.2 eV, and is larger than the correspond splitting of 2.7±0.1 eV for TiO_2 and 3.3±0.2 eV for ZrO_2, indicating a trend for 3d, 4d, and 5d state mixing with O 2p anti-bonding states.

The separation between E_g features in the ε_2 spectrum is larger than in the OK_1 edge, ~1.4 eV as compared to ~ 1 eV. This may be a matrix element effect since there is a factor of > 6 difference in the values of ε_2 at these d-states energies, compared to a difference of < 2 for the corresponding features in ZrO_2 where the agreement between the E_g splitting between ε_2 is much closer. The effective band gap from α and the PC response is 5.8±0.2 eV, and this band edge correlates with the lowest energy d-state feature. This optical band gap is slightly larger than for ZrO_2, consistent with the 0.3 eV difference in the atomic Zr 4d and Hf 5d states.[7] As in the case of ZrO_2, there is a sub-band gap feature extending to about 5.3-5.4 eV that is addressed in section 5.

The conclusions that is reached from the spectroscopic studies presented for TM elemental oxides are the following: i) as-deposited TM oxides are nanocrystalline as-deposited by remote plasma-assisted chemical vapor deposition or reactive evaporation, and ii) the band edge d-states detected by XANES and/or VUV SE indicate a complete removal of d-state degeneracies which is attributed to a J-T effect. All of our spectroscopic studies were restricted to film thicknesses in excess of about 5 nm. It is possible that films thinner than this may have a non-crystalline or amorphous character. This is issue will not be addressed. However, it is important to recognize that the detection of crystallinity on a scale

of less than 5 nm cannot be determined by convention x-ray diffraction, XRD, and other approaches such as XANES, EXAFS, and high resolution transmission electron microscopy, HRTEM, are required to detect nanocrsytallinity on a smaller scale, e.g., the 2 nm scale that is present in as-deposited films.

4.4.2 TM/RE complex oxides

Conduction band edge d-states are compared for three different classes of complex or pseudo-binary oxides: i) mixed tetravalent - trivalent ZrO_2-Y_2O_3 alloys, ii) tetravalent $Zr(Hf)O_2$-TiO_2 alloys, and iii) trivalent La scandate and aluminate. Low Y_2O_3 content cubic ZrO_2-Y_2O_3 alloys display two crystal-field split 4d-features in O K_1 spectra. Alloys with higher Y_2O_3 content, as well as $Zr(Hf)O_2$-TiO_2 alloys display increased d-state multiplicity. O K_1 spectra of perovskite-structured $LaScO_3$ and $LaAlO_3$ indicate Jahn-Teller (J-T) d-state term-splittings with contributions from both trivalent atomic species.

Figure 7 indicates O K_1 edge spectra for (a) ZrO_2, (b) and (c) ZrO_2 alloyed with 18.5 and 27.5% Y_2O_3, and (d) and (e) cubic and bixbyite Y_2O_3. Consistent with 8-fold coordination of both Y and Zr, the lowest energy 4d-state features in (a) to (d) are assigned to doubly-degenerate $4d_{3/2}$ (E_g) states, and the higher energy features to triply degenerate $4d_{5/2}$ (T_{2g}) states. The coordination of Y is 6-fold in trace (e), and the order of the 4d states is reversed. Differentiation of spectra indicates symmetric $4d_{3/2}$ and $4d_{5/2}$ features in (b), (c) and (d); i.e., no degeneracy removal, but departures from symmetry indicative of removal of d-state degeneracies in (a), and (e). Degeneracy removal in (a) and (e) is attributed to J-T term-splittings associated with distorted local bonding of Zr atoms in (a), and Y atoms in (e). $M_{2,3}$ spectra for Y from 300 and 330 eV, and Zr from 330 and 370 eV are in Fig. 8, in 8(a) ZrO_2, 8(b) and (c) alloys of ZrO_2 with 18.5 and 27.5% Y_2O_3, and 8(d) bixbyite Y_2O_3. Features

marked by dashed lines are transitions to Y and Zr 4s states; other features terminate in 3d states. $M_{2,3}$ transitions are intra-atomic, originating at spin-orbit split Y or Zr $3p_{3/2}$ and $3p_{1/2}$ core states, and terminating, respectively in Y or Zr 4d and 5s states. Three features are evident in the Y and Zr M_3 and M_2 features; energy differences between corresponding pairs are ~31 eV, essentially the same as the respective 3p core states differences. The Y, Zr d-state features are too broad to reveal J-T term splittings in the spectra of ZrO_2, or bixbyite Y_2O_3, even though these are evident in the respective O K_1 spectra.

Results in Fig. 7(a) for O K_1 edges indicate significant changes in bonding associated by O-atom vacancies; i.e., as an additional band edge feature centered at ~ 530.5 eV. The end-member traces in (a) for ZrO_2, and (d) and (e) for two different crystalline forms of Y_2O_3 all indicate features in the O K_1 spectra indicative of O-atom vacancies. At this time it is important to recognize that the spectra in (a) and (e), for ZrO_2 and bixbyite Y_2O_3 are not dependent on O-atom vacancies even though they are present. In contrast, the cubic form of Y_2O_3 is stabilized by these vacancies, as are the two Y_2O_3-ZrO_2 alloys in traces (b) and (c).

Figure 9(a) includes in (a) O K_1 edge spectra of (a) $(HfO_2)_{0.5}(TiO_2)_{0.5}$ and (b) $(ZrO_2)_{0.5}(TiO_2)_{0.5}$. The $(HfO_2)_{0.5}(TiO_2)_{0.5}$O K_1 spectra has three d-state features. The lowest energy feature is assigned to a TiO_2 3d state, the middle features to mixed TiO_2 3d/HfO_2 5d, states, and the highest features to a HfO_2 5d state. Differentiation of the spectrum in Fig. 9(a) indicates symmetric line shapes with no additional d-state features. This is consistent with a random alloy of 6-fold coordinated Ti, and either 6 or 8-fold coordinated Hf. In contrast other studies indicate a compound phase for $ZrTiO_4$ with 6-fold coordination for both Ti and Zr.[8] The O K1 spectrum for $ZrTiO_4$ is consistent with a compound in which both the Zr and Ti atoms are 6-fold coordinated, and are in distorted octahedral bonding arrangements. The

Ti L_3 spectra for both $(HfO_2)_x(TiO_2)_{1-x}$ and $(ZrO_2)_x(TiO_2)_{1-x}$ display essentially the same five 3d-state features of TiO_2. This is consistent with d-state degeneracy removal for Ti atoms in a distorted octahedral bonding environment in both titanates, the $(HfO_2)_{0.5}(TiO_2)_{0.5}$ alloy and the stoichiometric $ZrTiO_4$ compound.

Figure 10 displays O K_1 spectra: (c) as-deposited $LaAlO_3$ and $LaScO_3$: (b) as-deposited and (c) annealed at 1000°C. The $LaAlO_3$ spectrum displays two features assigned to Al 3p states at ~531.5 and 534 eV, as well as features at 535.5 and 537.5 eV assigned to La 5d states. The $LaScO_3$ spectra indicate both Sc 3d features, and L 5d. The differences between the as-deposited and 1000C annealed samples are the spectral line widths of these d-state features. Figure 10(d) displays the Sc L_3 spectra for $LaScO_3$, as-deposited and annealed at 1000°C. Difference between these films are again in the respective spectral line-widths of the J-T term split features.

Figures 11(a) and (b) display respectively the photoconductive response for $LaAlO_3$ and $LaScO_3$. The extrapolated edge features at ~4.7 and 5.5 eV are assigned to the Al 2p states. Since the energy difference between these two features is much smaller than the two features identified in the O K_1 edge, the edge at 4.7 eV is assigned to the lower energy Al feature in the O K_1 edge, at ~531.5 eV. This assignment is consistent with other assignments made for features in O K_1 spectra, and features in e2 and/or PC spectra as for example for ZrO_2 and HfO_2 as discussed in section 3. Three extrapolated edge features are evident in the $LaScO_3$ spectrum. Based on studies of Sc_2O_3 in Ref. 9, the lowest energy band gap in this material is ~ 4.6 eV, and the same as the lowest energy feature for Sc_2O_3. The onset of strong absorption in Sc_2O_3 occurs at ~ 6 eV. This relationship between band edge spectra in

elemental oxides, such as TiO_2 and Sc_2O_3, and complex oxides in which they are a constituent elemental oxide is well known.[10]

Qualitative and quantitative differences in O K_1 *inter-atomic* M-O transitions, and L_3, M_3 and N_3 intra-atomic have been presented for three different groups of complex oxides: those composed of (a) tetra- and tri-valent transition metal (TM) and/or rare earth (RE) atom oxides, (b) two TM tertravalent oxides, and (c) TM and RE oxides, or Al oxide. In addition, matrix element effects must be considered in the determination of conduction band offset energies between complex oxides, and Si or other semiconductors. These effects can different for all three classes of complex oxides, so considerable care must be taken in combining optical band edge data with valence band edge energy differences obtained from either UV or X-ray photoemission studies.

4.4.3 Intrinsic defect states

The next sections deals with intrinsic bonding defects. Spectroscopic measurements, including XANES and VUV SE, complemented by photoconductivity, PC, are used to first identify localized *defect states* approximately 0.6±0.2 eV below the conduction band edges of HfO_2 and ZrO_2.[2,3] A second defect state has also been identified; it is localized within the band gap of ZrO_2, and approximately 4.2±0.15 eV above the valence band edge, or equivalently, 1.4±0.15 eV below the conduction band edge. Based on model electronic structure calculations, the conduction band edge defects are assigned to states localized at grain boundaries between the nanocrystallites (hereafter GBDs),[1] and the defect states deeper in the gap at about 1.4±0.15 eV below the conduction band edge are assigned to oxygen atom vacancies (hereafter OVDs)[4].

Figures 5(a) and (c), respectively indicate (a) the absorption constant, α, for

nanocrystalline ZrO_2 thin films as a function of photon energy as derived from spectroscopic ellipsometry measurements, and (c) the square root of the photoconductivity (PC) response versus photon energy. Qualitatively similar results have been obtained for nanocrystalline HfO_2 films. The onset of the stronger PC response is defined by a linear extrapolation (solid line) to 5.6 eV in Fig. 5(c), and is effectively at a similar extrapolation of the band edge absorption in Fig. 5(a). Each of the spectra shows an addition feature at lower photon energies that extrapolates to an energy of ~ 5 eV in the PC response in Fig. 5(c) (dashed line), and to a similar energy for α versus photon energy in Fig. 15(a). These lower energy band edge spectral features are assigned to grain-boundary defect states that are an *inherent* aspect of the nanocrystallinity.

The O K_1 edge spectra for nanocrystalline ZrO_2 thin films for two different post deposition anneals in inert ambients at 500°C and 800°C are displayed in Fig. 12(a). The strong features centered at ~532.5 eV and 535.5 eV are due to mixing of the O 2p anti-bonding states with Zr E_g ($4d_{3/2}$) and T_{2g} ($4d_{5/2}$) states, respectively. Differentiation of these features identify the energies of the respective - effect doublet and triplet term-split states.[6] Figure 12(a) includes an expanded view of the leading edge of these spectra: the sample annealed at 500°C does not display any distinct spectral feature in this regime, whereas the one annealed at 800°C displays a feature at ~530.5 eV that is also present in $(ZrO_2)_{1-x}(Y_2O_3)_x$ *cubic-zirconia* thin film samples for x in the range from 0.15 to 0.25, as indicated in Fig. 12(b). This spectral feature is ~2 eV below the first $4d_{3/2}$ (E_g) feature of the respective O K_1 spectra. This spectral feature is assigned to O-atom vacancies[4]. This is confirmed by the absorption edge determination for a bulk crystal of *cubic zirconia*.

Figure 12(c) displays the absorption edge spectrum for a bulk *cubic zirconia* crystal

$[(ZrO_2)_{0.905}(Y_2O_3)_{0.095}]$. The strong sub-band gap absorption with a threshold of ~ 4.2 eV is assigned to the O-atom vacancy, and is excellent agreement with the calculations of the Robertson group.[4] It is important to recognize that the energy of the feature in the O K_1 edges in Figs. 12(a) and (b) to O-vacancies is consistent with the energy of the spectral feature in Fig. 12(c). This feature at 4.2 eV in Fig. 11(c) is 2.0±0.2 eV below the band edge $4d_{3/2}$ (E_g) feature that is obtained by differentiation of the spectrum in Fig. 12(c). This is essentially

Figure 13 indicates an energy level diagram that includes a Si substrate, a thin SiO_2 interfacial oxide, and then a thicker film of either ZrO_2 and HfO_2. Defect state energies with the band gap of ZrO_2, that are essentially the same for HfO_2 are indicated. The energy of the grain-boundary defect has been estimated from model calculations described in Ref. 4; the energy of the O-atom vacancy comes from the Robertson group,[4] and the energy of the H-defect from the universal alignment model of Van de Walle in Ref. 5.

The electrical activity of these defects has been observed in studies by the IMEC group and their collaborators that are summarized in Ref. 11, and by our group at NC State as well. Bulk traps ~0.5 to 0.8 eV below the high-k conduction band have been reported for injection from n-type Si, through thin SiO_2 layers (~1 to 10 nm) into thicker ZrO_2/HfO_2 films.[11] A hole trap ~0.26 eV above the valence band edge was extracted from C-V data for gate electron injection into in the ZrO_2 MOSCAPs.[11] Similar results have been obtained by us in J-V data for n-Si substrate electron injection in MOSCAPS with stacked SiO_2-ZrO_2, and SiO_2-HfO_2 dielectrics. We have also found an interface trap at ~0.3 eV above the Si valence band edge in C-V traces for gate e-injection in SiO_2-HfO_2 MOSCAPs. The energy of the interface trap relative to the HfO_2 valence band is 4.2±0.2 eV, agreeing with theory[4] and

cathodoluminescence measurements. Our studies and those in Ref. 1, do not indicate an electronically active defect associated with H.[5]

To the best our knowledge this combined spectroscopic and theory/modeling of intrinsic defects in nanocrystalline HfO_2 and ZrO_2, coupled with device studies, represents the first unambiguous assignment for electronically-active defects in high-k gate stacks. The energies of these defects relative to the forbidden energy gap in Si also explain differences in bias temperature instabilities, BTIs, in NMOS and PMOS FETs, and present a significant obstacle for integration of HfO_2/ZrO_2 dielectrics into scaled Si CMOS.[12]

The results presented in this paper, combined with discussions in Ref. 4, make it highly unlikely than any nano-crystalline transition metal or lanthanide series rare earth atom elemental or complex oxide can be integrated into scaled CMOS devices. Combinations of defect states associated with fixed charge, band edge grain boundary defects, and oxygen atom vacancies, as well as defect states associated with hydrogen,[1,4,5,12] will introduce sufficient quantities of defects to prevent devices from displaying targeted performance and/or reliability metrics. In contrast, Zr or Hf Si oxynitride films with approximately equal concentrations of SiO_2, Si_3N_4 and ZrO_2 or HfO_2 will remain non-crystalline after annealing to at least 1100°C, and offer engineering solutions for high performance devices with EOTs to ~0.7 to 0.8 nm, and mobile devices with EOTs to ~ 1.5 nm.

4.4.4 Zr silicate and oxynitride alloys

Figures 14(a) and (b) present FTIR results for Zr silicate alloys with ZrO_2 fractions, x, equal to 0.23 and 0.5.[13] The feature at ~950 cm^{-1} in Figs. 14(a) for the as-deposited films is assigned to a terminal $Si\text{-}O^{1-}$ group, an indicator of network disruption by addition of the ionic ZrO_2 elemental oxide into the more covalently-bonded SiO_2 *host* network. The broader

Si-O bond-stretching feature in Fig. 14(b) is assigned to the SiO_4^{4-} molecular ion, and indicates *complete network disruption* at this composition. There are changes in FTIR spectral features in Figs. 14(a) and (b) between the as-deposited films and films annealed at 900°C. These indicate CPS into SiO_2 and ZrO_2. Separation is confirmed by HRTEM imaging.[14] Spectral features change gradually over the entire range of annealing temperatures, but not with a well-defined activation energy as in an Arhenius plot. Comparisons between the kinetics for the CPS in the silicate alloys, and the CPS for thin film silicon suboxide, SiO_x, x~1, into non-crystalline SiO_2 and crystalline Si indicate similar kinetics. This is used to infer a similar mechanism to that in Ref. 15 for the CPS of TM silicate thin films.

The corresponding XRD spectra (not shown in this chapter) indicate no detectable crystallization, except for the x = 0.5 sample after a 900°C anneal. The FTIR spectra for a Zr silicate alloy with x = 0.61 in which there is network inversion, are consistent with the SiO_4^{4-} molecular ion as-deposited, and CPS into non-crystalline SiO_2 and crystalline ZrO_2 after a 900°C anneal.

Figures 15(a) and 15(c) display FTIR results for two pseudo-ternary $Zr(Hf)O_2$-SiO_2-Si_3N_4 alloys, and Figs. 15(b) and 15(d) include derivative XPS O 1s core level spectra for the same alloys. Spectra in Figs. 15(a) and 15(b) are for an alloy with Si_3N_4 alloy, ~25% Si_3N_4, ~45% SiO_2 and ~30% ZrO_2. Concentrations are accurate to ±5% in these ternary alloys. The FTIR and XPS spectra indicate CPS. In the FTIR spectrum there are non-crystalline SiO_2 features at ~1050 cm^{-1} and 800 cm^{-1}, and a nanocrystalline ZrO_2 feature at ~450 cm^{-1}. In the XPS there are two spectral features after a 1000°C anneal. XAS studies of the O K_1 and N K_1

edges of this alloy composition indicate a loss of bonded nitrogen for annealing temperatures greater than ~750°C.

Spectra in Figs. 15(c) and 15(d) are for an alloy with approximately equal concentrations, ~45%, of Si_3N_4 and SiO_2, and a ZrO_2 concentration of at least 10%. After annealing, the FTIR indicates weak Si-O features which are more $SiO4^{4-}$ ion-like than SiO_2 network-like and a non-crystalline ZrO_2 feature. This is supported by derivative XPS that shows a single dominant feature at an energy that significantly different than either non-crystalline SiO_2 or ZrO_2, and closer in energy to the feature in as-deposited Zr silicate with 50% ZrO_2 therefore with SiO_4^{4-} molecular ions as well. The single O 1s XPS feature is also consistent with studies of the O K_1 edge which indicate no detectable changes between as-deposited films, and those annealed at 500, 750 and 1000°C.

The experimental studies have benefited from the extension of bond constraint theory (BCT) originally developed to explain glass formation,[16] and extended compositional stability of Na, Ca and Al silicates,[17] to transition metal silicates, including $Zr(Hf)O_2$ and $Y(La)_2O_3$. This application of BCT demonstrated that i) all group IVB and IIIB transition metal (TM) silicates are *over-constrained* upon deposition, with the number of constraints per atom exceeding the network dimensionality of three, and havin a *significant break-up* of the SiO_2 network, which is a precursor state to chemical phase separation (CPS) into non-crystalline SiO_2, and a nanocrystalline TM oxide second phase, and ii) the Zr(Hf) silicon oxynitride alloys are also *unstable* against CPS and crystallization of a TM oxide phase if the Si_3N_4 concentration, y, is smaller than the SiO_2 concentration, 1-x-y, independent of the $Zr(Hf)O_2$ concentration, x, but iv) if $1-x-y \approx x \approx 0.3$ to 0.35, and $y \approx 0.33$ to 0.4, then CPS and

$Zr(Hf)O_2$ crystallization are suppressed by *chemical self-organizations* resulting in stable bonding arrangements that are effectively defect free.[18]

Combinations of FTIR and XPS are used to demonstrate that there are changes in chemical bonding in Zr and Hf silicate alloys that occur with annealing temperatures (in inert ambients) in excess of deposition temperatures of 300°C, and that the rate of bonding changes increases dramatically for annealing temperatures > 800°C with CPS and crystallization of the TM oxide readily evident after 900°C annealing. Similar observations hold for Zr Si oxynitride alloys with low Si_3N_4 compositions, y, in the range of 0.1 to 0.25. Changes in these alloys were also tracked by XANES, in particular the O K_1 and N K_1 edge spectra. In addition to CPS and ZrO_2 crystallization, the XANES and XPS indicate decomposition with release of N.

FTIR, XPS and XANES studies of Zr silicate alloys in which the Si_3N_4 concentration y~0.4, and is greater than x and 1-x-y, each equal to ~0.3, indicated changes in chemical bonding indicative of a chemical self organization that i) prevented CPS, ii) reduced bond-strain by encapsulation Zr-O-Si bonding groups within a Si_3N_4 matrix, thereby preventing percolation of bond-strain throughout the entire film.

Chemical phase separation has been identified by changes in the C-V characteristics of Zr silicate and Zr Si oxynitride thin film dielectrics as well.[19] In marked contrast, the C-V and I-V characteristics of films with Zr Si oxynitride gate dielectrics that have about the same composition as those described in Figs. 15(c) and 15(d), exhibit ideal behavior with dielectric constants in the range of 8 to at least 10. This means that if the relative concentrations of SiO_2, Si_3N_4 and $Zr(Hf)O_2$ are controlled within narrow limits in *pseudo-ternary* non-crystalline Zr/Hf Si oxynitrides with high Si_3N_4 content; e.g.,

$(Hf(Zr)O_2)_{\sim 0.3}(Si_3N_4)_{\sim 0.4}(SiO_2)_{\sim 0.3}$, then chemical phase separation (CPS) and crystallization are completely suppressed by *chemical self-organizations* which relieve local bond-strain,[18] resulting in gate dielectrics extend EOT scaling to ~0.7-0.8 nm.

4.5 Conclusions

The conclusions that is reached from the spectroscopic studies presented for TM elemental oxides are the following: i) as-deposited TM oxides are nanocrystalline as-deposited by remote plasma-assisted chemical vapor deposition or reactive evaporation, and ii) the band edge d-states detected by XANES and/or VUV SE indicate a complete removal of d-state degeneracies which is attributed to a J-T effect. All of our spectroscopic studies were restricted to film thicknesses in excess of about 5 nm. It is possible that films thinner than this may have a non-crystalline or amorphous character. This is issue will not be addressed. However, it is important to recognize that the detection of crystallinity on a scale of less than 5 nm cannot be determined by convention x-ray diffraction, XRD, and other approaches such as XANES, EXAFS, and high resolution transmission electron microscopy, HRTEM, are required to detect nanocrsytallinity on a smaller scale, e.g., the 2 nm scale that is present in as-deposited films.

Qualitative and quantitative differences in O K_1 *inter-atomic* M-O transitions, and L_3, M_3 and N_3 intra-atomic have been presented for three different groups of complex oxides: those composed of (a) tetra- and tri-valent transition metal (TM) and/or rare earth (RE) atom oxides, (b) two TM tetravalent oxides, and (c) TM and RE oxides, or Al oxide. In addition, matrix element effects must be considered in the determination of conduction band offset energies between complex oxides, and Si or other semiconductors. These effects can different for all three classes of complex oxides, so considerable care must be taken in

combining optical band edge data with valence band edge energy differences obtained from either UV or X-ray photoemission studies.

To the best our knowledge this combined spectroscopic and theory/modeling of intrinsic defects in nanocrystalline HfO_2 and ZrO_2, coupled with device studies, represents the first unambiguous assignment for electronically-active defects in high-k gate stacks. The energies of these defects relative to the forbidden energy gap in Si also explain differences in bias temperature instabilities, BTIs, in NMOS and PMOS FETs, and present a significant obstacle for integration of HfO_2/ZrO_2 dielectrics into scaled Si CMOS.[12]

Chemical phase separation has been identified by changes in the C-V characteristics of Zr silicate and Zr Si oxynitride thin film dielectrics as well.[18] In marked contrast, the C-V and I-V characteristics of films with Zr Si oxynitride gate dielectrics that have about the same composition as those described in Figs. 15(c) and 15(d), exhibit ideal behavior with dielectric constants in the range of 8 to at least 10. This means that if the relative concentrations of SiO_2, Si_3N_4 and $Zr(Hf)O_2$ are controlled within narrow limits in *pseudo-ternary* non-crystalline Zr/Hf Si oxynitrides with high Si_3N_4 content; e.g., $(Hf(Zr)O_2)_{\sim 0.3}(Si_3N_4)_{\sim 0.4}(SiO_2)_{\sim 0.3}$, then chemical phase separation (CPS) and crystallization are completely suppressed by *chemical self-organizations* which relieve local bond-strain, resulting in gate dielectrics that have the potential to extend EOT scaling to ~0.7-0.8 nm.

Finally, The results presented in this paper, combined with discussions in Ref. 4, make it highly unlikely than any nano-crystalline transition metal or lanthanide series rare earth atom elemental or complex oxide can be integrated into scaled CMOS devices. Combinations of defect states associated with fixed charge, band edge grain boundary defects, and oxygen atom vacancies, as well as defect states associated with hydrogen,[1,4,5,12]

will introduce sufficient quantities of defects to prevent devices from displaying targeted performance and/or reliability metrics. In contrast, Zr or Hf Si oxynitride films with approximately equal concentrations of SiO_2, Si_3N_4 and ZrO_2 or HfO_2 will remain non-crystalline after annealing to at least 1100°C, and offer engineering solutions for high performance devices with EOTs to ~0.7 to 0.8 nm, and mobile devices with EOTs to ~ 1.5 nm.

4.6 Acknowledgements

The research reported in this article is supported by contracts from the Office of Naval Research (ONR) and the Semiconductor Research Corporation (SRC).

4.7 References

[1] G. Lucovsky, et al. IEEE Trans. on Material and Device Reliability **5**. 65 (2005).

[2] S. Zollner and D. Tyrioso, and B.R. Rogers and S. Zollner, unpublished.

[3] V.V. Afanas'ev and A. Stesmans, Appl. Phys. Lett. **80**, 1957 (2002); V.V. Afanas'ev, et al., Appl. Phys. Lett. **85**, 5917 (2004).

[4] J. Robertson, et al. IEEE Trans. on Material and Device Reliability **5**. 84 (2005).

[5] C.R. Van de Walle, Nature **423**, 636 (2003).

[6] F.A. Cotton and G. Wilkinson, *Advanced Inorganic Chemistry 3rd Ed.* (Wiley Interscience, New York, 1972), Chap. 20.

[7] W.A. Harrision, *Elementary Electronic Structure* (World Scientific Publishing, Singapore, 1999), Back-cover Table.

[8] Hem, B.K, et al., J. Chem. Thermodynamics **30**, 2001, pp. 165-178.

[9] H.H. Tippins, J. Phys. Chem. Solids **27**, 1069 (1966).

[10] P.A. Cox, *Transition Metal Oxides* (Oxford Science Publications, Oxford, 1992), Chapter 2.

[11] J-L Autran, D. Munteanu and M. Housa, in *High-k Dielectrics* (IOP, Bristol, 2004), Chap. 3.4

[12] J.C. Lee and K. Onishi, in Ref. 4, Chap. 5.3

[13] G.B Rayner, D. Kang, and G. Lucovsky, J. Vac. Sci. Technol. B **21**, 17483 (2003).

[14] G.B Rayner , D. Kang, and G. Lucovsky, J. Non-cryst. Solids **338**, 151 (2004).

[15] B.J. Hinds, F. Wang, D.M. Wolfe, C.L. Hinkle and G. Lucovsky, J. Vac. Sci. Technol. **B 16**, 2171 (1998).

[16] J.C. Phillips, J.Non-Cryst. Solids **34**, 153 (1979): **43** 37 (1981).

[17] R. Kerner and J.C. Phillips, Solid State Commun. 117, **47** (2001).

[18] P. Boolchand, in *Phase Transitions and Self-Organization in Electronic and Molecular Networks* (Kluwer Academic, New York, 2001) p. 65.

[19] Byunsun Ju, Ph.D. Dissertation, Department of Materials Science and Engineering, North Carolina State University, July 2005.

Figure Captions

Figure 4.1: O K_1 edge spectrum and derivative for noncrystalline Zr silicate 30% alloy as-deposited. (b) O K_1 edges for 60% alloy, as-deposited and after a 900°C anneal which results in chemical phase separation into SiO_2 and nano-crystalline ZrO_2.

Figure 4.2: X-ray absorption near edge spectra for TiO_2: (a) the Ti $L_{2,3}$ edge, (b) the L_3 edge spectrum, (c) the O K_1 edge spectrum.

Figure 4.3: Band edge spectra for TiO_2: (a) the imaginary part of the complex constant, ε_2, where $\varepsilon_c = \varepsilon_1+i\varepsilon_2$, (b) the absorption constant, α, (c) comparison between the five d-state features in the L_3 edge, and in ε_2, and (d) the photoconductivity response.

Figure 4.4: X-ray absorption near edge spectra for ZrO_2: (a) the Zr $M_{2,3}$ spectra, and (b) the O K_1 edge spectrum.

Figure 4.5: Band edge spectra for ZrO_2: (a) the imaginary part of the complex constant, ε_2, where $\varepsilon_c = \varepsilon_1+i\varepsilon_2$, (b) the absorption constant, α, and (c) the photoconductivity response.

Figure 4.6: X-ray absorption near edge spectra for HfO_2: (a) the O K_1 edge spectrum, (b) the imaginary part of the complex constant, ε_2, where $\varepsilon_c = \varepsilon_1+i\varepsilon_2$, (c) the absorption constant, α, and (d) the photoconductivity response.

Figure 4.7: O K_1 edge spectra for: (a) ZrO_2, (b) and (c) ZrO_2 alloyed with 18.5 and 27.5% Y_2O_3, and (d) and (e) cubic and bixbyite Y_2O_3.

Figure 4.8: $M_{2,3}$ spectra for (a) ZrO_2, (b) and (c) alloys of ZrO_2 with 18.5 and 27.5% Y_2O_3, and (d) bixbyite Y_2O_3. Features marked by dashed lines are transitions to Y and Zr 4s states. All other features terminate in 3d states.

Figure 4.9: X-ray absorption near edge spectra for Zr and Hf titanate alloys: O K_1 edge spectra of (a) a $(HfO_2)_{0.5}(TiO_2)_{0.5}$ alloy and (b) the stoichiometric compound $ZrTiO_4$ or equivalently $(ZrO_2)_{0.5}(TiO_2)_{0.5}$.

Figure 4.10: O K_1 spectra: (a) $LaAlO_3$, and $LaScO_3$: (b) O K_1 as-deposited and (b) ObK_1 annealed at 1000°C, (d) Sc L_3 spectra as-deposited, and (e) Sc L_3 spectra annealed at 1000°C.

Figure 4.11: Photoconductive response spectra for: (a) $LaAlO_3$, and (b) $LaScO_3$.

Figure 4.12: O K_1 spectra, with expanded view of the leading edge of these spectra: (a) ZrO_2 and (b) an alloy of ZrO_2 with 18.5 Y_2O_3, and (c) the absorption edge spectrum, α, for a bulk cubic zirconia crystal $[(ZrO_2)_{0.905}(Y_2O_3)_{0.095}]$.

Figure 4.13: An energy level diagram that includes a Si substrate, a thin SiO_2 interfacial oxide, and a thicker film of either ZrO_2 and HfO_2. Defect state energies within the band gap of ZrO_2 are indicated for a grain boundary defect, an O-atom vacancy, and a H-defect.

Figure 4.14: Fourier transform infra red absorbance spectra for Zr silicate alloys with ZrO_2 fractions, x, equal to (a) 0.23 and (b) 0.5.

Figure 4.15: FTIR results for two pseudo-ternary $Zr(Hf)O_2$-SiO_2-Si_3N_4 alloys in (a) and (c), and include derivative XPS O 1s core level spectra for the same alloys in (b) and (d).

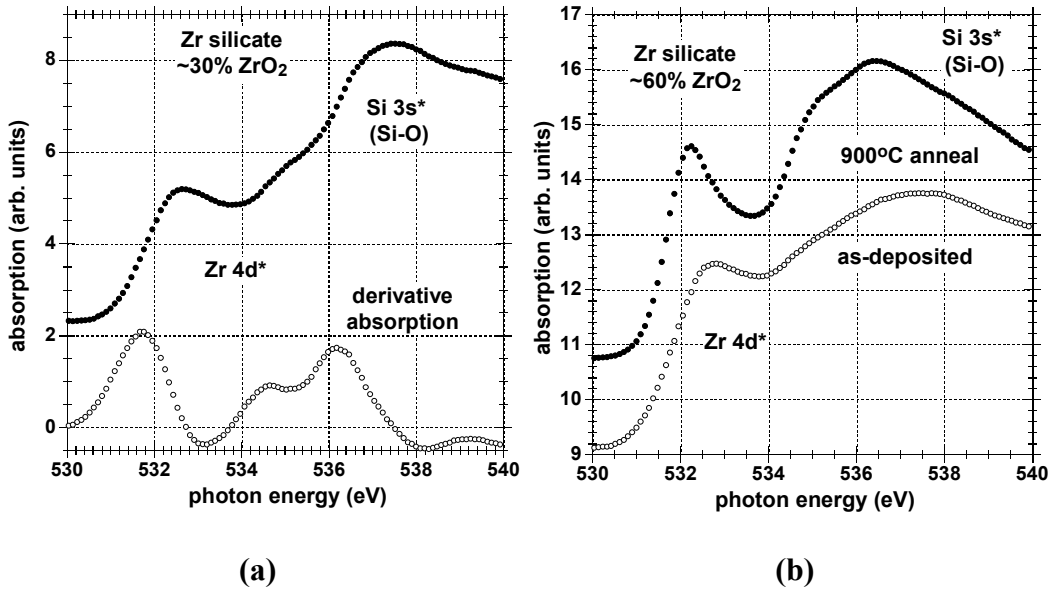

Figure 4.1: O K_1 edge spectrum and derivative for noncrystalline Zr silicate 30% alloy as-deposited. (b) O K_1 edges for 60% alloy, as-deposited and after a 900°C anneal which results in chemical phase separation into SiO_2 and nano-crystalline ZrO_2.

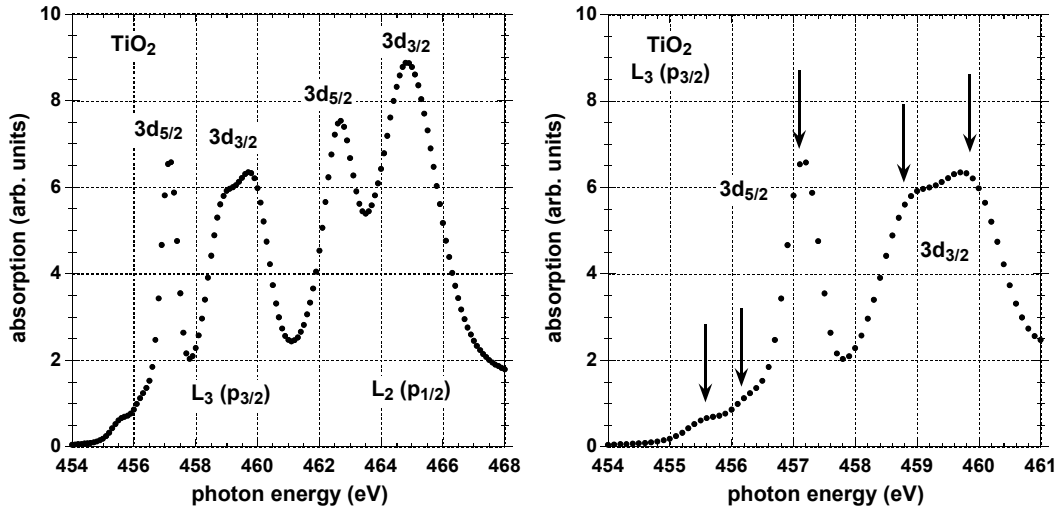

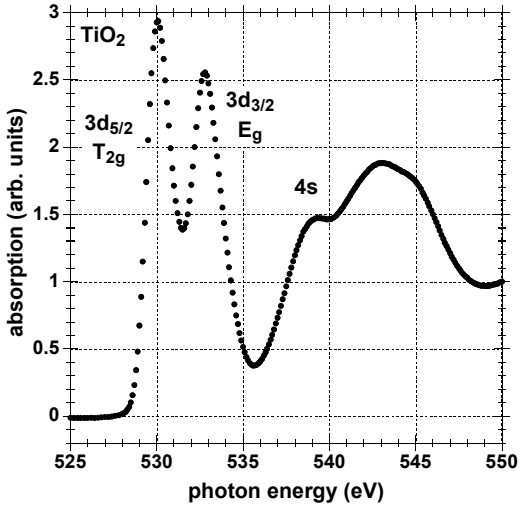

Figure 4.2: X-ray absorption near edge spectra for TiO_2: (a) the Ti $L_{2,3}$ edge, (b) the L_3 edge spectrum, (c) the O K_1 edge spectrum.

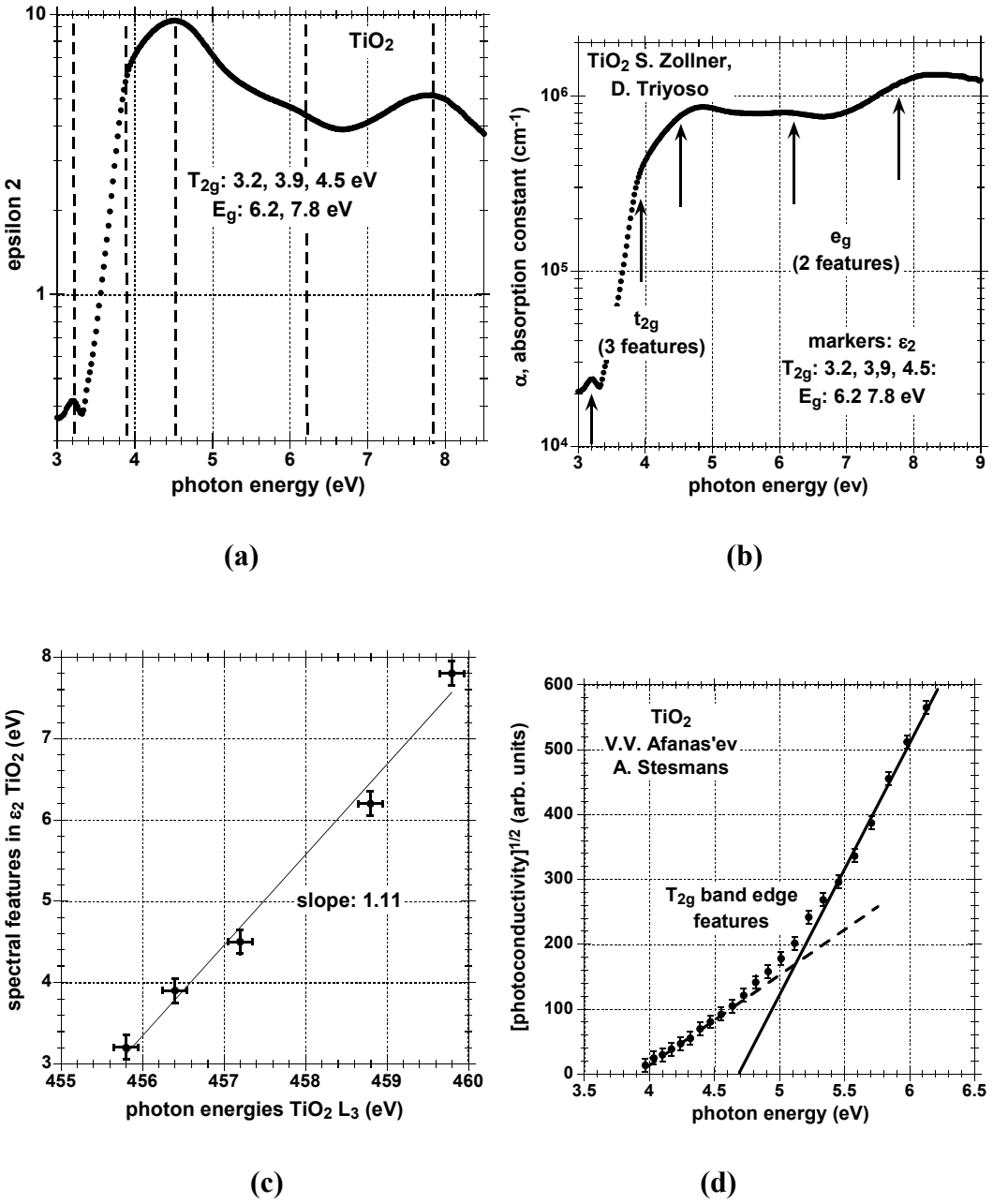

Figure 4.3: Band edge spectra for TiO_2: (a) the imaginary part of the complex constant, ε_2, where $\varepsilon_c = \varepsilon_1 + i\varepsilon_2$, (b) the absorption constant, α, (c) comparison between the five d-state features in the L_3 edge, and in ε_2, and (d) the photoconductivity response.

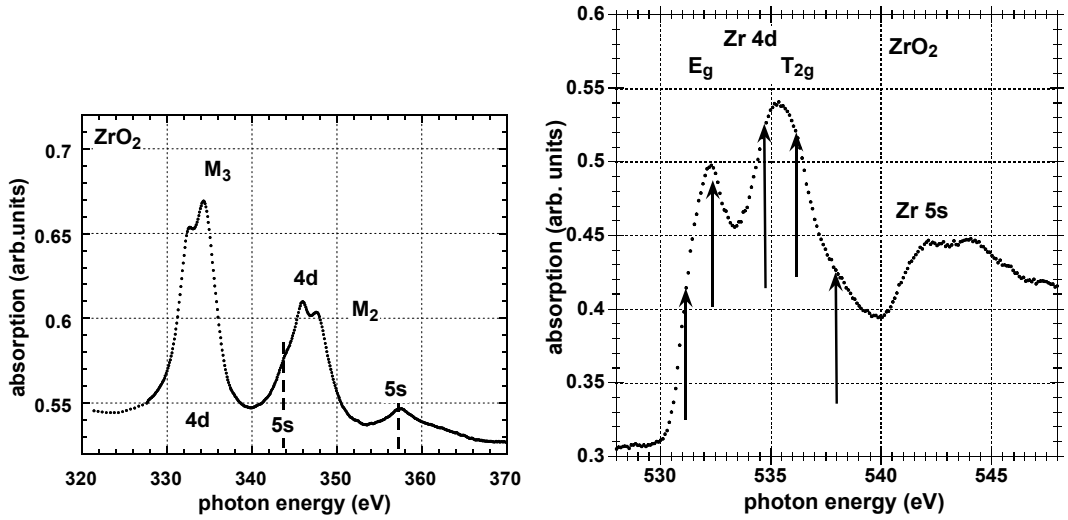

(a) **(b)**

Figure 4.4: X-ray absorption near edge spectra for ZrO_2: (a) the Zr $M_{2,3}$ spectra, and (b) the O K_1 edge spectrum.

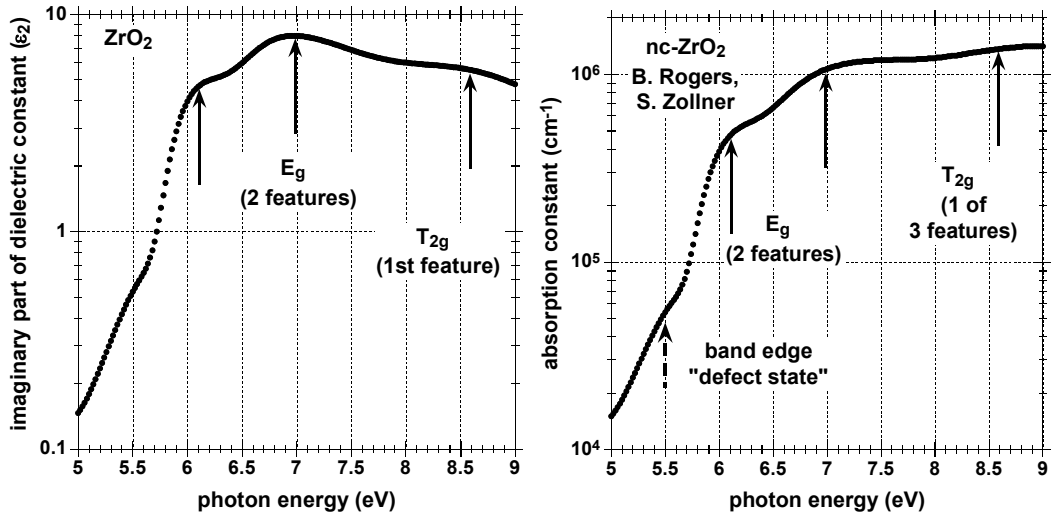

(a) **(b)**

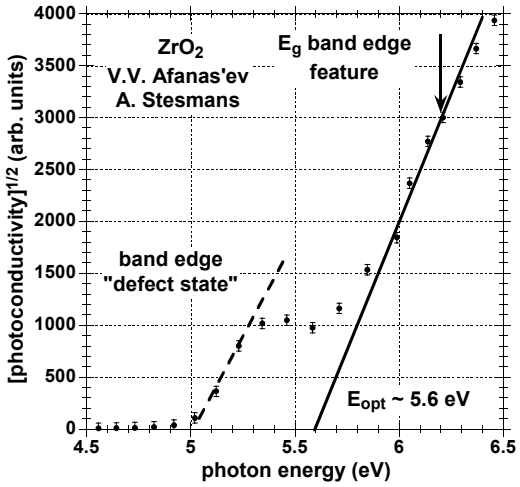

(c)

Figure 4.5: Band edge spectra for ZrO_2: (a) the imaginary part of the complex constant, ε_2, where $\varepsilon_c = \varepsilon_1 + i\varepsilon_2$, (b) the absorption constant, α, and (c) the photoconductivity response.

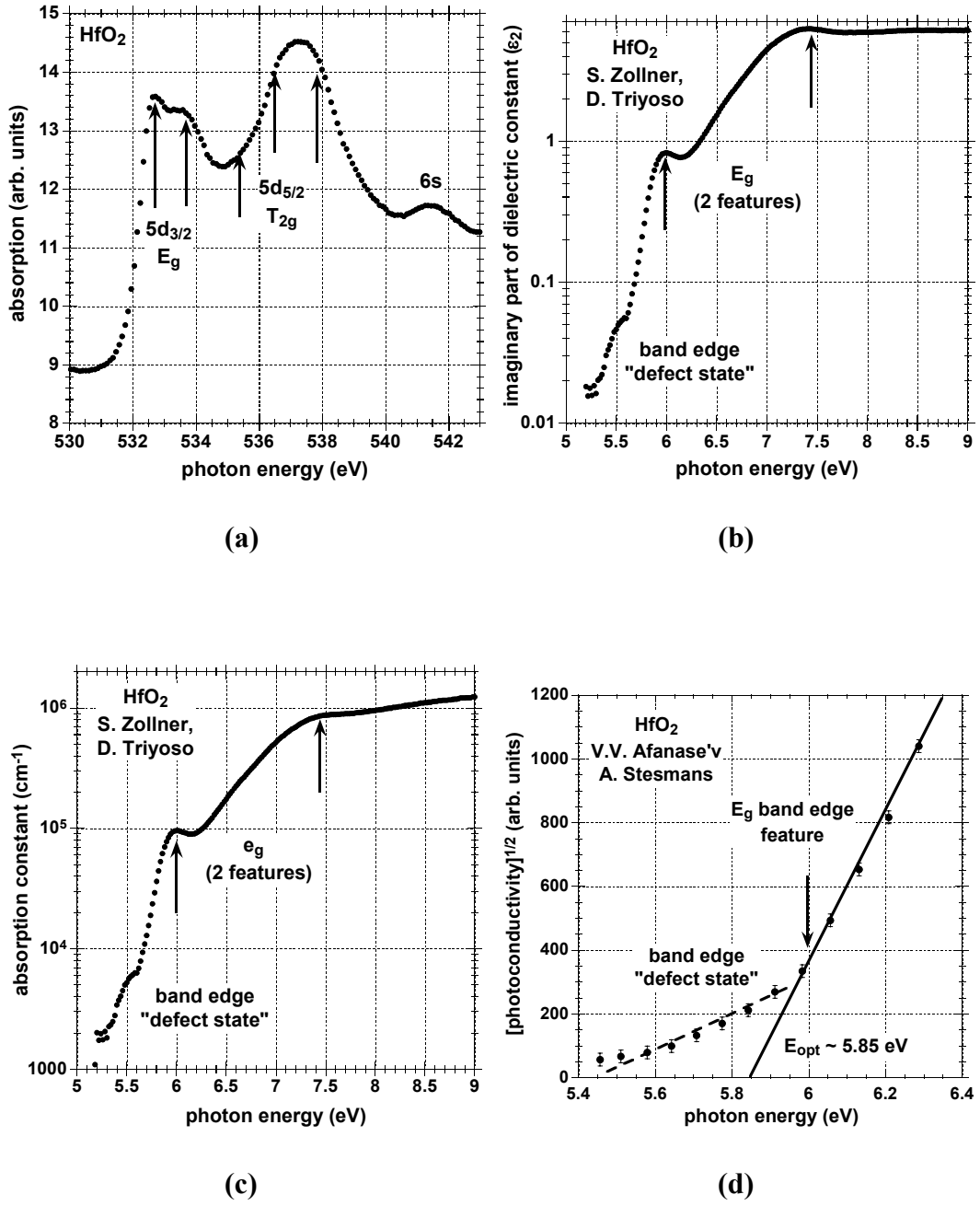

Figure 4.6: X-ray absorption near edge spectra for HfO_2: (a) the O K_1 edge spectrum, (b) the imaginary part of the complex constant, ε_2, where $\varepsilon_c = \varepsilon_1 + i\varepsilon_2$, (c) the absorption constant, α, and (d) the photoconductivity response.

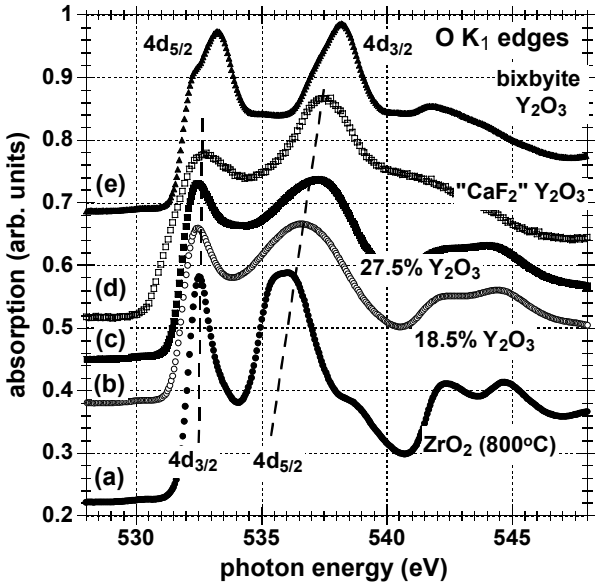

Figure 4.7: O K_1 edge spectra for: (a) ZrO_2, (b) and (c) ZrO_2 alloyed with 18.5 and 27.5% Y_2O_3, and (d) and (e) cubic and bixbyite Y_2O_3.

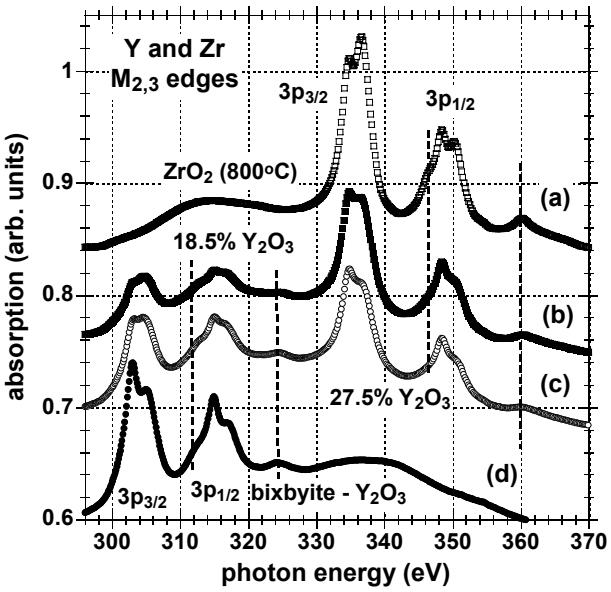

Figure 4.8: $M_{2,3}$ spectra for (a) ZrO_2, (b) and (c) alloys of ZrO_2 with 18.5 and 27.5% Y_2O_3, and (d) bixbyite Y_2O_3. Features marked by dashed lines are transitions to Y and Zr 4s states. All other features terminate in 3d states.

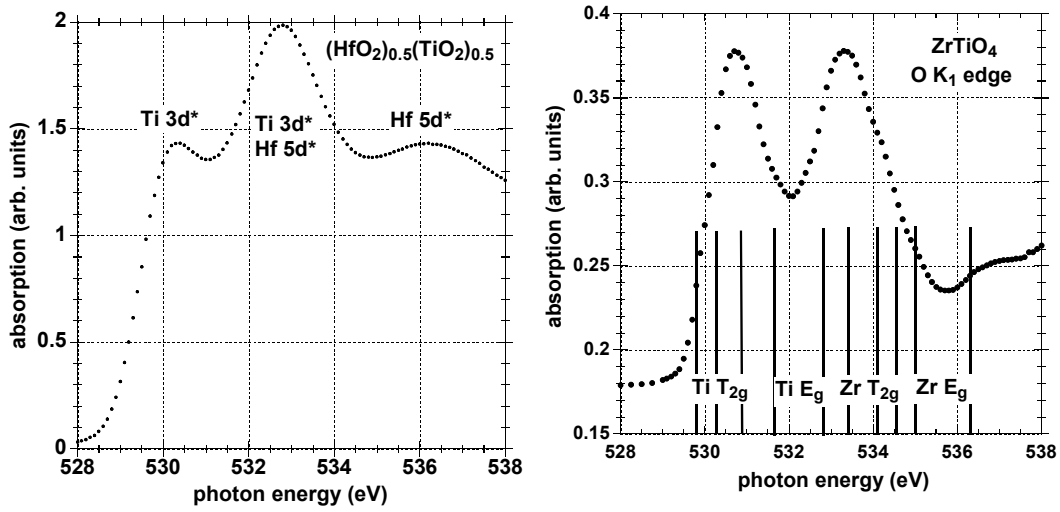

Figure 4.9: X-ray absorption near edge spectra for Zr and Hf titanate alloys: O K_1 edge spectra of (a) a $(HfO_2)_{0.5}(TiO_2)_{0.5}$ alloy and (b) the stoichiometric compound $ZrTiO_4$ or equivalently $(ZrO_2)_{0.5}(TiO_2)_{0.5}$.

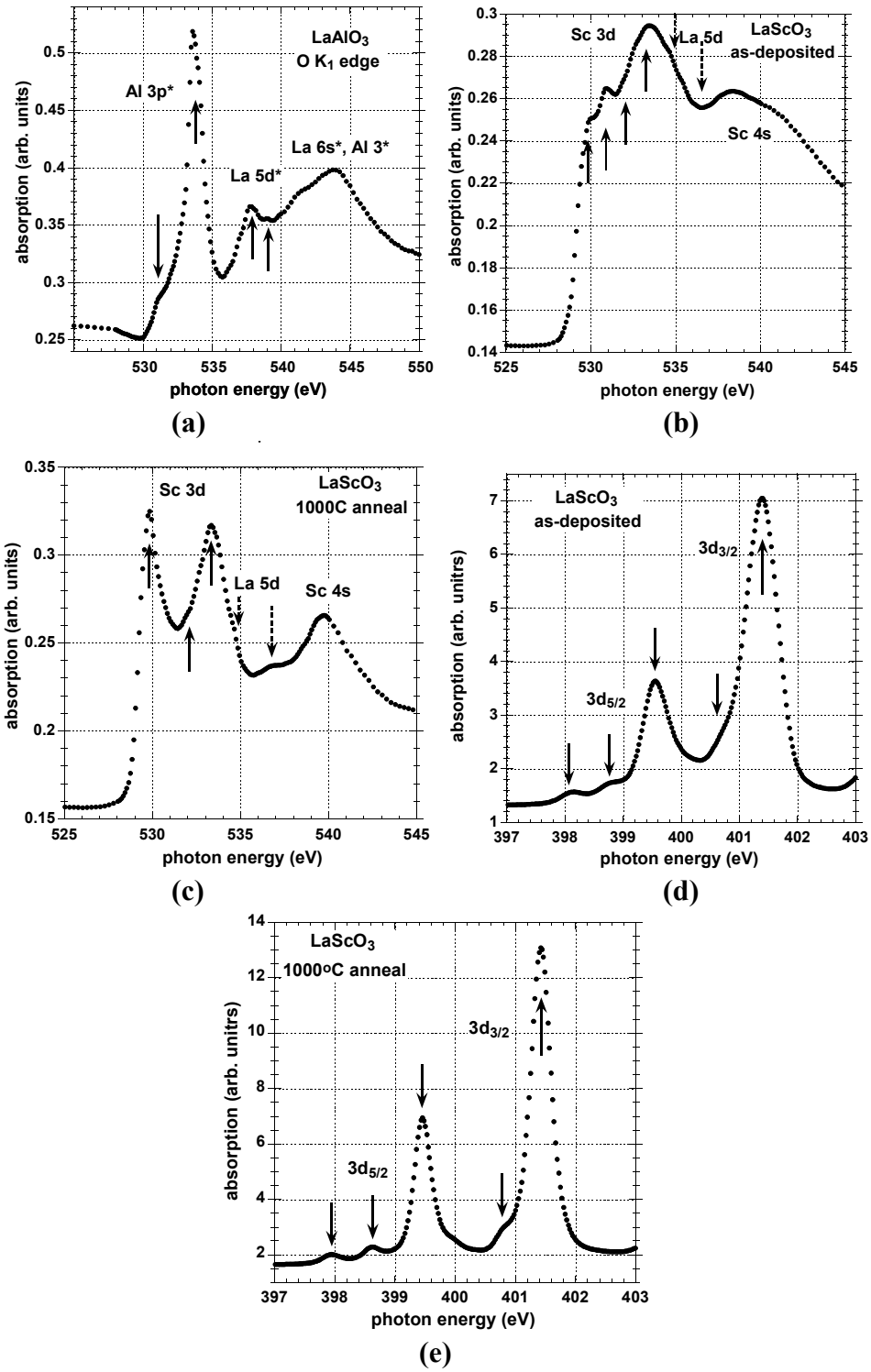

Figure 4.10: O K_1 spectra: (a) $LaAlO_3$, and $LaScO_3$: (b) O K_1 as-deposited and (b) OK_1 annealed at 1000°C, (d) Sc L_3 spectra as-deposited, and (e) Sc L_3 spectra annealed at 1000°C.

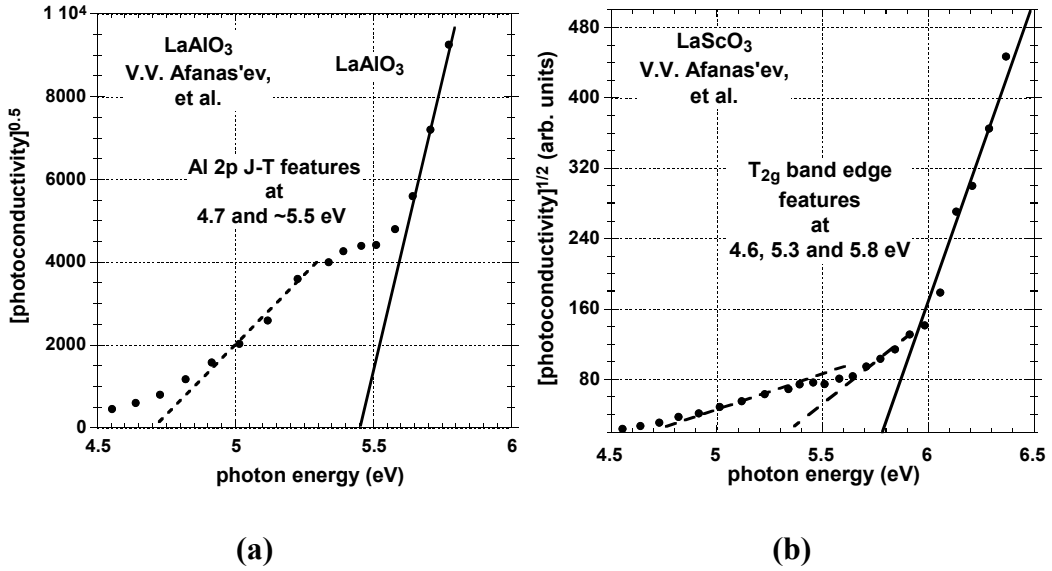

Figure 4.11: Photoconductive response spectra for: (a) $LaAlO_3$, and (b) $LaScO_3$.

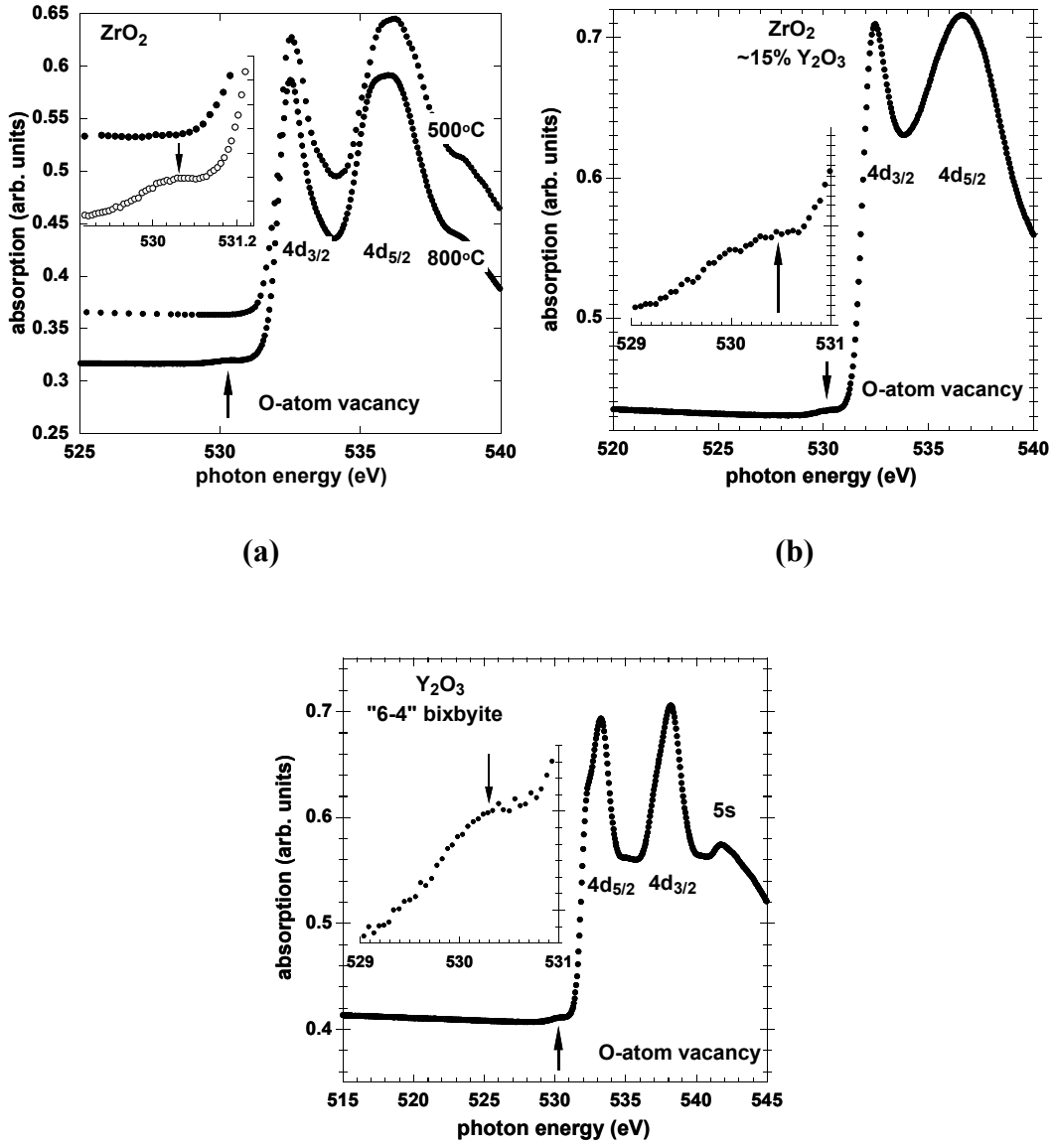

Figure 4.12: O K_1 spectra, with expanded view of the leading edge of these spectra: (a) ZrO_2 and (b) an alloy of ZrO_2 with 18.5 Y_2O_3, and (c) the absorption edge spectrum, α, for a bulk cubic zirconia crystal $[(ZrO_2)_{0.905}(Y_2O_3)_{0.095}]$.

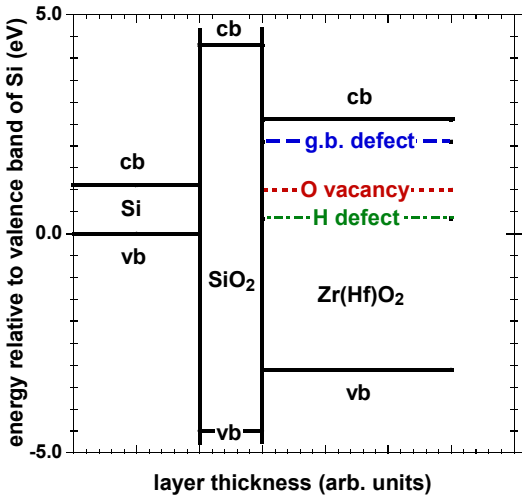

(a)

Figure 4.13: An energy level diagram that includes a Si substrate, a thin SiO_2 interfacial oxide, and a thicker film of either ZrO_2 and HfO_2. Defect state energies within the band gap of ZrO_2 are indicated for a grain boundary defect, an O-atom vacancy, and a H-defect.

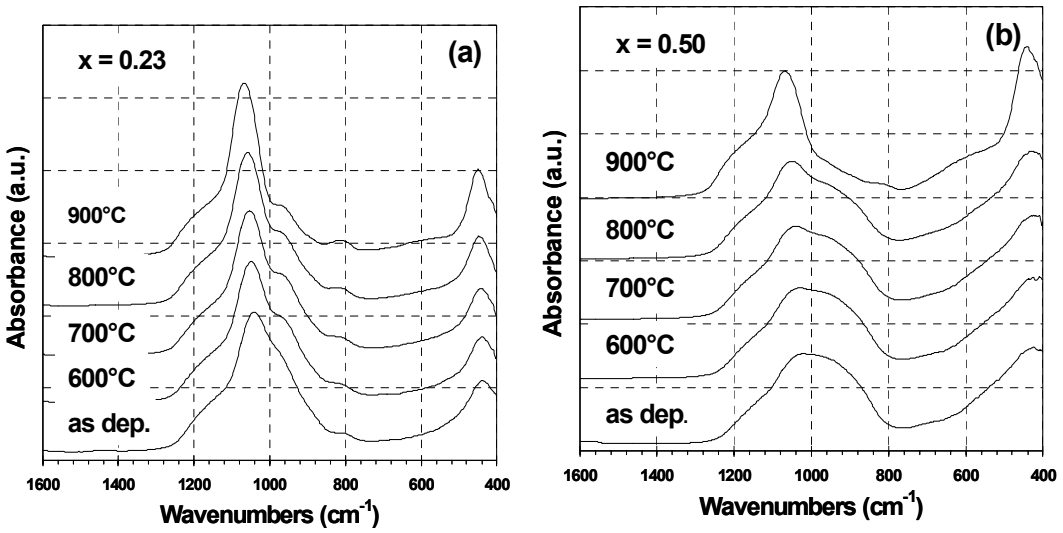

(a) **(b)**

Figure 4.14: Fourier transform infra red absorbance spectra for Zr silicate alloys with ZrO_2 fractions, x, equal to (a) 0.23 and (b) 0.5.

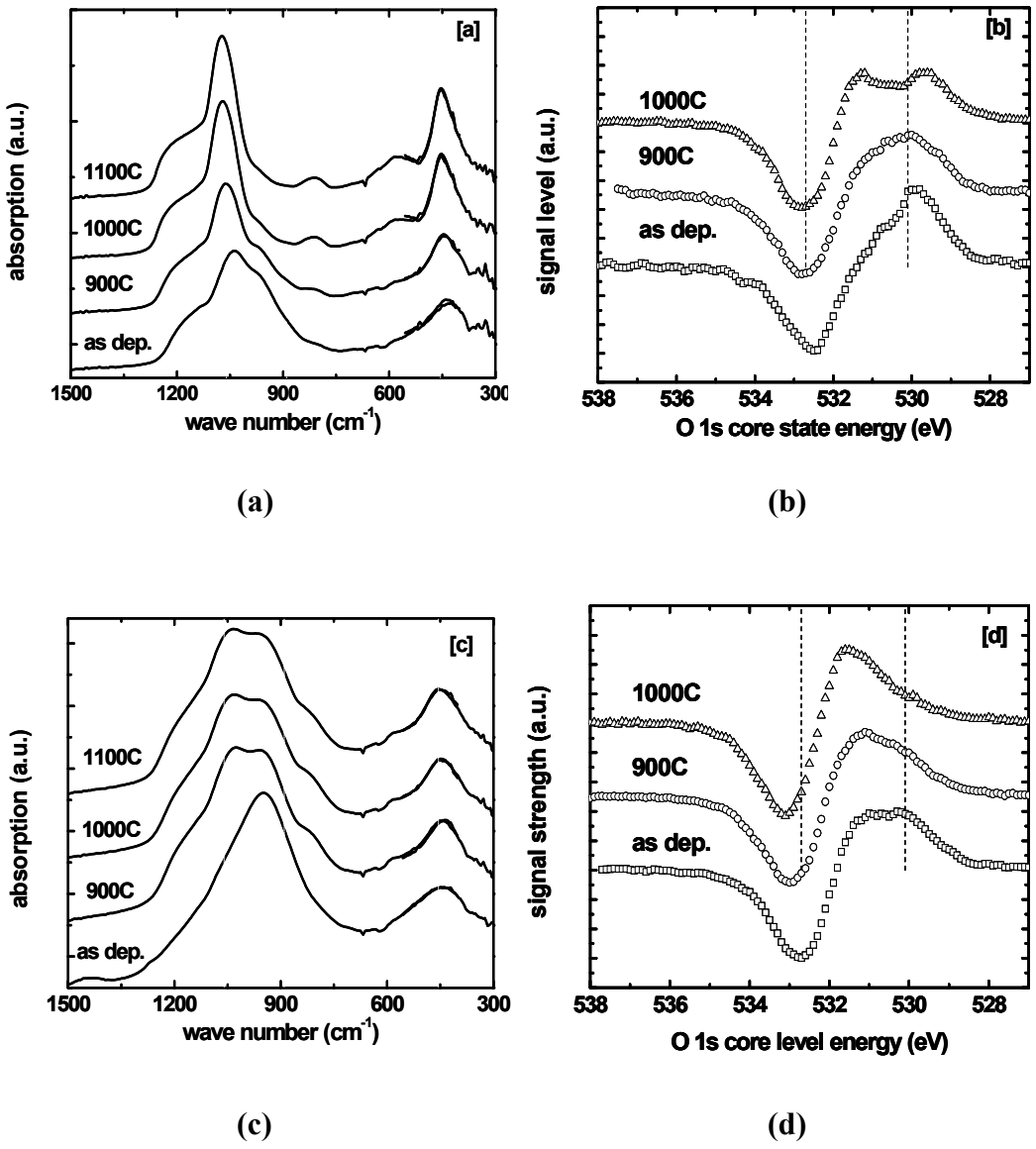

Figure 4.15: FTIR results for two pseudo-ternary $Zr(Hf)O_2$-SiO_2-Si_3N_4 alloys in (a) and (c), and include derivative XPS O 1s core level spectra for the same alloys in (b) and (d).

5. Electronic Properties of the $Zr–ZrO_2–SiO_2–Si(100)$ gate stack structure

C.C. Fulton
Department of Materials Science and Engineering,
North Carolina State University
Raleigh, NC 27695-7907

G. Lucovsky and R.J. Nemanich
Department of Physics
North Carolina State University
Raleigh, NC 27695-7907

Manuscript to be submitted to:

Journal of Applied Physics
Aug 2005.

5. Electronic Properties of the $Zr–ZrO_2–SiO_2–Si(100)$ gate stack structure

5.1 Abstract

The interface electronic structure of a layered $Zr–ZrO_2–SiO_2–Si(100)$ system was studied with x-ray ($h\upsilon$=1254eV) and ultraviolet ($h\upsilon$=21.2eV) photoemission spectroscopy. *In-situ* growth and characterization allow the structures to be deposited and studied in a stepwise manner without risk of contamination. This study discusses the electronic properties including electron affinities and work functions, valence band maxima, band bending in the Si and internal fields in a layered high-κ gate stack. With this information the band allignments can be reconstructed and compared to predictions by the interface induced gap states (IFIGS) model and the Schottky-Mott or electron affinity model. The Schottky models presume that aligning the vacuum levels of two materials will give electronic barrier height for a heterojunction but interface bonding can contribute to charge transfer across the interface, forming a dipole and altering the barrier heights. The band offsets and vacuum levels are independently measured thereby determining the deviation from the vacuum level alignment models. The valence band offsets at the $Si–SiO_2$, $SiO_2–ZrO_2$ and $ZrO_2–Zr$ are found to be: 4.4±0.1, 0.67±0.24 and 4.9±0.44 eV, respectively. For these same interfaces the deviation from the Schottky-Mott or electron affinity model are determined to be: 0.2±0.14, -1.43±0.29 and 1.3±0.39 eV for those interfaces, respectively.

5.2 Introduction

The planned scaling of integrated circuit devices involves a reduction of the gate insulator thickness to obtain the targeted capacitance and sheet charge density in the channel. As the gate dielectric thickness is reduced below 2 nm, direct tunneling between the gate and channel becomes significant, leading to increased power consumption. As an alternative to reducing the physical thickness of the gate oxide, the dielectric constant could be increased. This would allow the desired increase in capacitance with a physically thicker layer, resulting in both a reduced tunneling current and an increase in sheet charge density. With devices based on conventional silicon oxides and oxynitrides approaching their physical limits, the exploration of alternative materials has gained significant momentum.[1]

The fundamental criteria for a gate dielectric include: barrier heights that will effectively block both electrons and holes, chemical stability in contact with both the silicon substrate and the gate material, and a low density of interface electronic states. Zirconium oxide, with its large bandgap of ~5.7 eV and dielectric constant of ~25, is of particular interest as a gate dielectric.[7,2,3] Moreover, the ZrO_2–Si band offsets have been predicted to be favorable for blocking both holes and electrons.[4]

Integrating a transition metal (TM) oxide in place of SiO_2 is a complex process. The deposition of TM oxides on Si often results in an interfacial SiO_x layer which, although it can lower the interface state density and improve device characteristics, must be carefully controlled as it has a much lower dielectric constant than the TM oxide and can significantly limit the minimum achievable effective oxide thickness (EOT). It is also desirable to replace the heavily doped poly-Si with a metal as the gate material. While poly-Si can be appropriately doped for both *n*- and *p*-type devices, it still exhibits a significant depletion width to terminate the field

applied to the device gate. This depletion width also contributes to the total EOT in a device, and replacing the poly-Si with a metal with a much shorter depletion width becomes necessary for aggressively scaled devices.[5] Any metal to be used as a gate material must be chemically stable when in contact with a TM oxide. Additionally, the metal and its characteristic work function must be chosen appropriately for *n*- and *p*-type devices. Thus, the integration of high-κ dielectric materials into a device is a much more complex process than that for a thermal oxide or even a deposited oxynitride.

The internal interfaces of the gate stack will significantly affect the performance of the devices. Chemical bonding occurs at these interfaces and the charge transfer across these bonds can result in an interface dipole.[4,6] In addition, dangling bonds and defects at the interface can contribute to this charge transfer which may lead to internal fields in the gate stack. The Schottky-Mott model for metal–semiconductor junctions and, by extension, the electron affinity model for semiconductor–semiconductor junctions are based on the alignment of the vacuum level of the two materials.[7] While it is evident that these models are based on a highly idealized interface, the advantage is that the barrier heights and band offsets can be estimated from measurable quantities (i.e., work functions and/or electron affinities). Alternatively, the band alignment has been described with non-specific heuristic approaches such as the charge neutrality model discussed extensively by Robertson, Peacock and Mönch.[4,8,9]

In essence, the difference between the values predicted by the vacuum level alignment models and the charge neutrality model represents an interface dipole which contributes a potential step at the interface. This dipole is related to the polarity of the interface bonding and the net charge transfer across that interface.

In this research in-situ photoelectron spectroscopy has been employed to directly and independently measure the band alignment at each interface in the gate stack structure. The techniques allow direct measurement of the valence band offsets for semiconducting and/or dielectric layers. While for metal-dielectric interfaces, the techniques will determine the offset between the metal Fermi level and the dielectric valence band.

In order to determine the dipole at each interface, it is necessary to determine the metal work function and/or the electron affinity of the dielectric or semiconductor. For semiconductors and dielectrics, the determination of the electron affinity requires knowledge of the band gap. Independent measurement of the valence band maximum and the vacuum level of each material at an interface allows expression of the conduction band offset as the difference in electron affinities plus an additional term that is ascribed to the contribution from the interface dipole ($\phi_{CBO} = (\chi_1 - \chi_2) \pm \Delta$). This additional term Δ can either increase or decrease the band offset depending on the specific chemistry at the interface in question. Similarly for a metal-semiconductor (or a metal-dielectric) interface, the contact potential as defined by the Schottky-Mott model will also be corrected with an additional term to accommodate the contribution from the interface dipole ($\phi_{bh} = (\Phi_M - \chi) \pm \Delta$). Where ϕ_{bh} is the conduction band barrier height, Φ_M is the metal work function and χ is the semiconductor or oxide electron affinity. In the experiments presented here, all values are measured, and only the band gap of the semiconductor or dielectric is required to determine the conduction band alignment.

The basic approach of these studies is to employ in-situ deposition and characterization to fabricate thin film structures that approximate a gate stack and to use photoemission to characterize the development of the electronic properties in a stepwise manner. Through the combined x-ray and ultraviolet photoemission measurements we are able to determine the band

alignment, the metal work functions and the electron affinities in each layer as well as the band bending in the Si substrate, and the presence of internal fields in the dielectric layers. By comparison with the appropriate Schottky-Mott and electron affinity models, the interface dipole can be deduced for each interface.

5.3 Experiment

All experiments were performed on 25mm diameter, *n*-type, 0.05-0.1 ohm-cm (3×10^{18} to 1×10^{17} cm^{-3} phosphorous), Si (100) wafers. These wafers were loaded into a UHV integrated growth and analysis system which includes a linear UHV transfer system interconnecting 16 different process and characterization chambers. Four of these chambers were employed in this study for steps including: plasma oxidation, reactive deposition of ZrO_2, electron beam deposition of Zr metal, X-ray photoemission spectroscopy (XPS), and ultra violet photoemission spectroscopy (UPS).

An initial oxygen plasma exposure was employed to remove residual hydrocarbon contamination and to form the thin (0.5 nm) oxide buffer layer. Zirconium oxide thin films were grown by electron beam evaporation of zirconium metal in an O_2 ambient followed by a 30s remote oxygen plasma exposure to ensure complete oxidation. The samples were then *in-situ* annealed to 500°C for five minutes to remove excess oxygen that has been observed in other studies.[10,11] Metal layers were electron beam evaporated in vacuum. After each process step the films were analyzed with XPS and UPS to observe trends in the electronic properties.

Formation of the initial SiO_2 buffer layer and the post-high-κ oxidation step were performed in a remote plasma-enhanced chemical vapor deposition (RPECVD) chamber with a base pressure of $5 \cdot 10^{-9}$ Torr. Remote plasma exposures took place with the sample at room temperature, with a gas flow of 10 standard cubic centimeters per minute (sccm) of O_2 and 50

sccm of He and an operating pressure of 60 mTorr. To minimize ion damage from the plasma the substrate is located ~20 cm downstream of the discharge region in which the plasma was excited by 20 watts RF power.

The zirconium oxide was deposited with the substrate at room temperature in a UHV chamber with a base pressure of $8 \cdot 10^{-10}$ Torr by electron beam evaporation of Zr metal at a rate of ~0.05 nm/s (measured by a quartz crystal oscillator) in an ambient of 2×10^{-6} Torr O_2. The pressure of research-grade O_2 was regulated using a precision leak valve and a turbo molecular pump (TMP). Following the oxide deposition, samples were exposed to a remote oxygen plasma (same conditions and time as used for the initial buffer layer) and vacuum annealed to 500°C for five minutes.

The approximate oxide film thickness can be deduced from the thickness of the deposited metal layer using the molar densities and the molar masses of the TM and its oxide. This analysis gives a ratio of 1.5 : 1 for the thickness of a ZrO_2 film formed from Zr metal. The estimated film thicknesses discussed here are calculated accordingly and assume complete oxidation of the deposited TM layer. A second method for determining the thickness of thin films by XPS has been described by Shallenberger *et al.*[12] The molar density thicknesses were corroborated by the relative intensity changes of the Si bulk peak from the Si 2p core level spectra, as a function of film thickness.

In this research, ultraviolet photoemission spectra were obtained using a He discharge lamp primarily generating the He I line at 21.2 eV in a chamber with an operating pressure of $3 \cdot 10^{-9}$ Torr. A VSW 50mm mean radius hemispherical analyzer and VSW HAC300 were operated with a pass energy of 10 eV, resulting in an electron energy resolution of 0.1 eV. A negative 4.00 V bias was applied to the sample to assure that the photoelectrons can overcome

the analyzer work function. All photoemission spectra are presented in binding energy relative to the system Fermi level and the electron spectrometer has been calibrated by defining the Fermi edge of an *in-situ* deposited Au film as zero binding energy.

Ultraviolet photoemission spectroscopy probes to a depth of 0.5 to 1.0 nm. Features in the spectrum are a reflection of the valence band density of states. The valence band maximum (VBM) can be determined with respect to the system Fermi level which will correspond to the Fermi level in the bulk of the Si. Since the band bending and internal fields can be determined from XPS, then the actual valence band offset (VBO) can be determined for the upper most layer with respect to the lower layers and the Si VBM. The high binding energy cut-off of the valence band spectrum represents the vacuum level at the surface. The vacuum level with respect to the Fermi level (i.e. the work function) is determined from the photon energy minus the binding energy of the vacuum cut-off. For the case of an semiconductor or dielectric layer, the conduction band position and the electron affinity can be determined with knowledge of the band gap.

X-ray photoemission spectra were obtained at a pressure of $2 \cdot 10^{-9}$ Torr using the 1253.6eV Mg *K*α or the 1486.6 eV Al *K*α line from a VG Microtech (now Thermo Electron Corp) XR3 dual anode source and a VG Microtech Clam II electron analyzer. The resolution of the analyzer was determined from the full width at half maximum (FWHM) of a gold 4f 7/2 spectral peak to be approximately 1.0 eV; however, through curve fitting, the centroid of spectral peaks can be resolved to ±0.1 eV. Observation windows were set around the Si 2p, O 1s and Zr 3d core level binding energies to record shifts.

For gate structures limited to a total thickness of ~ 4nm, X-ray photoemission can probe the entire gate stack including the silicon substrate. Since the depletion width of moderately

doped (~10^{17} cm^{-3}) Si is much greater than the sampling depth of XPS, we can assume that the Si 2p XPS core level associated with the Si substrate indicates the binding energy of states at the Si-dielectric interface. Thus, changes in the binding energy of this feature will accurately indicate changes in the band bending in the Si. Additionally, changes in the Si band bending are typically associated with the development of an internal field in the dielectric.

As layers are added to the gate stack, spectroscopic shifts are observed in the core level spectra of the underlying dielectric, which can be attributed to a field in the oxide. If there is an internal field in the layer, the potential of the atoms will change across the thickness of the films and the binding energy detected in the XPS core levels will be shifted to reflect this change. For a thin layer the presence of a field would result in the XPS peak to be shifted by an amount equal to one half of the potential change across the layer. Here we assume that the x-rays excite photoemission uniformly across the layer, the photoelectrons are not attenuated, and the potential changes linearly across the layer. In this case the spectral centroid will correspond to the binding energy of the atoms at the center of the layer. For example, for an SiO_2 layer with an internal field that would result in a one volt change in potential we would expect the centroid of the core level peaks to be shifted by 0.5 eV, an amount representative of the potential at the center of the film.

While uniform excitation from the x-ray source is a reasonable approximation, the probability of a photoelectron escaping the layer depends exponentially on the depth from which the photoelectron was emitted. Consequently, the observed core level spectra becomes the weighted average of the photoemission from all atoms between the two interfaces of the layer. Thus, if a potential exists across a layer, then the centroid position of the core level spectrum will reflect the potential at a position displaced from the center of the layer towards the outer surface.

The following describes our approach to account for this effect and to determine the total potential across a given layer from the measured shift of a core level peak. We assume that the layer thickness and the photoelectron attenuation are known. The photoelectron signal intensity, *I*, will be attenuated for increased depths in the film. The intensity from any thickness is given by:

$$I = I_0 e^{\frac{-z}{\lambda}} \tag{1}$$

Where I_0 is the signal intensity for the atoms at the surface, z is the depth from which the photoelectron originates and λ is the photoelectron inelastic mean free path. The electron mean free path is an energy-dependent function that has been approximated by a power law expression: $\lambda = kE^p$.[13] Ashley and Tung have tabulated data for the parameters k and p (both experiment and theory) for electron energies that are in the range considered here (400-2000 eV).[14] The electron inelastic mean free path in an SiO_2 film for an electron kinetic energy of 1150 eV (i.e. Si 2p core level) is found to be ~3.2 nm (k=0.218, p=0.706).

Assuming that λ is constant in the energy range over which the core level spectra are observed to shift (~1 eV) we can then determine the depth, Z_{av}, that will represent the centroid binding energy of the observed photoelectron spectrum which is given by:

$$Z_{av} = \frac{\int_{z_1}^{0} f(z)w(z)dz}{\int_{z_1}^{0} w(z)dz} \tag{2}$$

where z_1 is the thickness of the layer, and the functions *f(z)* and *g(z)* are of the form:

$$f(z) = z \text{ and } w(z) = e^{\frac{-z}{\lambda}} \tag{3}$$

Substituting the values appropriate for the Si 2p core level peak from Ashley *et al*. and the calculated electron mean free path into Equation 2, the weighted average depth is then given by:

$$Z_{av} = \frac{3.2\left[1 - e^{\frac{-z_1}{3.2}}\left(\frac{z_1}{3.2} + 1\right)\right]}{1 - e^{\frac{-z_1}{3.2}}} \tag{4}$$

where z_1 is the thickness of the layer in nm and 3.2 is the calculated electron mean free path, also in nm.

The observed centroid of the core level spectrum corresponds to the binding energy of a photoelectron emitted from a depth of Z_{av}; thus if there exists a potential across a layer from which photoelectrons are extracted then the centroid of the core level spectrum will be shifted in energy by the potential at the depth Z_{av}. For example: if an SiO_2 layer is 1.0 nm thick then Equation 4 indicates that the Z_{av} = 0.4 nm and if the potential across the layer is 1.0 V then the observed spectral centroid would be shifted 0.6 eV from the zero potential condition. The observed shift is related to the total potential across the layer by:

$$V_{tot} = \frac{V_{observed}}{1 - Z_{av}} = \frac{0.6V}{1 - 0.4} = 1.0V \tag{5}$$

We deduce that an observed shift of 0.6 eV in a 1.0 nm thick layer corresponds to a total potential across the layer of 1.0 V. In this way, it is possible to correlate an observed core level shifts from a thin film of known thickness to a total potential across the layer.

5.4 Results

With stepwise growth and *in-situ* characterization, changes in the electronic structure can be observed layer-by-layer as the gate stack structure is formed. In the following sections the results are described from each layer in the structure beginning with the 0.5 nm SiO_2 buffer layer. A summary of the experimental results is presented in Table 1.

5.4.1 0.5 nm SiO_2

Figure 1 presents the XPS Si 2p core level spectrum for 0.5 nm SiO_2 on n-Si. Fitting of the Si 2p spectral features indicates the substrate-related feature at a binding energy of 99.6 eV and the Si–O bonded feature from the SiO_2 buffer layer at 103.3 eV.

Ultraviolet photoemission spectroscopy yields a plot which reflects features of the total density of states of the SiO_2 valence band. As in all of the photoemission spectra the zero energy reference is the bulk Fermi level of the system. Figure 2 shows the valence band spectrum for 0.5 nm SiO_2 on n-Si. The lower binding energy (front) edge of the spectrum represents the VBM and the higher binding energy (back) edge represents the vacuum level. By fitting the front of the spectrum (using a linear fit through the point of maximum slope), we find that the VBM of the SiO_2 is 5.2 eV with respect to the substrate Fermi level. Fitting of the vacuum cut-off is completed in a similar way. The data indicates the vacuum cut-off at 16.6 eV below E_F.

5.4.2 1.0 nm ZrO_2

In-situ XPS and UPS measurements are repeated after deposition of 1.0 nm ZrO_2 (Figures 3 and 4). Shifts in the bulk Si 2p core level (~99 eV) are ascribed to changes in Si substrate band bending, and shifts in the oxide-bonded Si 2p core level (~103 eV) from the interfacial SiO_2 indicate a field in the oxide. Figure 3 shows the Si 2p core level spectrum both before and after ZrO_2 deposition. With deposition of the high-κ material the core level position for Si in the substrate is unchanged at 99.6 eV (to within the experimental error of ±0.1 eV), and with the deposition of the high-κ material, the SiO_2 related peak is shifted 0.2 eV lower in binding energy to 103.1 eV. A spectrum was also obtained for the Zr 3d doublet core level which indicated a Zr 3d 5/2 peak at a binding energy of 183.0 eV.

Ultraviolet photoemission probes only the top-most layer (ZrO_2 in this case) and the scan shown in Figure 4 indicates features of the valence band total density of states versus binding energy. Fitting the VBM and vacuum level as shown in Figure 4, the two features are found at 4.2 and 17.7 eV, respectively.

5.4.3 1.0 nm Zr metal

Shifts are observed in the core level peaks with the deposition of 1.0 nm of Zr onto the oxide gate stack. The Si 2p core level again gives insight into band bending and the field in the SiO_2 layer. After Zr deposition the Si substrate core level (Figure 5) is shifted 0.2 eV higher in binding energy (to 99.8 eV), indicating a downward change in band bending of 0.2 eV. The Si core level from SiO_2 shows a larger 0.5 eV shift to higher binding energy to 103.6 eV. This shift is opposite in direction when compared to the shift seen with ZrO_2 deposition and again indicates a field in the SiO_2 but one with an opposite sign.

The Zr 3d core level doublet (Figure 6) can be used to obtain information about the field in the ZrO_2 layer. The core levels of Zr metal and ZrO_2 overlap somewhat and require a deconvolution to separate the contributions from oxide related (higher binding energy) from the metal related (lower binding energy) peaks. The deconvoluted oxide related Zr 3d core level indicated a shift to higher binding energy of 0.3 eV (to 183.3 eV) when compared to the deposited ZrO_2.

Valence band spectra of metallic films display emission that extends to the Fermi level of the system (zero binding energy) as shown in Figure 7. The vacuum level cut-off of the Zr metal spectrum is found to be 17.1 eV.

5.5 Discussion

We now discuss the results from each layer in the structure beginning with the 0.5 nm SiO_2 buffer layer and apply the analysis that was described above to determine the band offsets, internal fields and interface dipoles. A summary of the deduced results is presented in Table 2.

5.5.1 0.5 nm SiO_2

In an effort to determine the band bending of the initial oxidized surface, we had previously measured the VBM and Si 2p core level of a clean, hydrogen-terminated Si(100) surface.[15] For a wafer of the same specification as those used in this study, we find the Si VBM to be 0.8 eV below the Fermi level, and the Si 2p core level at 99.6 eV. This results in an energy difference between the Si 2p core level and the VBM of ΔE=98.8± 0.1eV, a value similar to that of other reports.[16,17]

From the study noted above and our measurement of the Si 2p bulk core level at 99.6 eV below the Si E_F, we determine that the Si VBM is 0.8 eV below E_F or that the Fermi level is 0.3 eV below the Si CBM. This is a reasonable value (within ±0.1 eV) for n-type Si doped to the mid-10^{17} cm^{-3} range. The results indicate that to within the measurement error of ±0.1 eV that the Si underlying the 0.5 nm SiO_2 interface layer has flat bands.

From the UPS measured position of the oxide VBM and the knowledge of the Fermi level position within the Si gap the VBO for a 0.5 nm SiO_2 film on Si is determined to be 4.4±0.1 eV (VBO = 5.2±0.1 – 0.8 = 4.4±0.1 eV).

The electron affinity of the SiO_2 buffer is determined from the photon energy used to excite the valence band spectrum (21.2 eV), the measured width of the UPS spectrum (i.e. the vacuum level – VBM), and the reported band gap (9.0 eV). The electron affinity is determined from the expression: $\chi = h\nu - W - E_g$. In this case, using a bandgap for SiO_2 of 9.0 eV we find

that χ = 21.2 – 11.4±0.14 – 9.0 = 0.8±0.14 eV. Determining the electron affinity requires knowledge of the bandgap which has not been measured in this study and are taken from literature sources. Consequently, the electron affinities reported will vary with the particular literature value for the dielectric bandgap.

With the band bending information from XPS, the deduced VBO and the electron affinity, a schematic band diagram can be constructed (Figure 8). Note that the VBO is determined independently from the vacuum level. In these experiments the Si vacuum level has not been measured and the electron affinity of 4.1 eV is from literature, as are the values for the oxide bandgaps.[18] In these measurements the alignment of the vacuum levels has been determined independently and the deviation from the electron affinity rule, that is, the difference in vacuum levels of the two materials is then ascribed to an interface dipole. In this case the dipole is Δ = 0.2±0.14 eV. For SiO_2 on Si the dipole effectively increases the barrier for electrons in the Si conduction band.

5.5.2 1.0 nm ZrO_2

Following the ZrO_2 deposition, the binding energy of the Si 2p substrate core level position is unchanged; from this we conclude that, to within ±0.1 eV, the Si bands are flat as they were with the 0.5 nm SiO_2 layer. Using Equation 4 with z_1=*0.5* nm, we find that the centroid of the shifted SiO_2 feature is representative of the field at a depth of 0.2 nm. When corrected for the exponential dependence of the electron escape probability, we find that the 0.2±0.1 eV shift in the SiO_2 related Si 2p core level corresponds to a 0.33±0.17 V potential across the SiO_2 layer.

A potential across the SiO_2 layer can alter the observed band offset for ZrO_2 with respect to the Si E_F. Therefore, the VBO of the ZrO_2 relative to the Si VBM can then be corrected to a zero potential case, and we find that the VBO = 4.2±0.1 – 0.8 + 0.33±0.17 = 3.73±0.19 eV.

Using the same procedure as described above for SiO_2 the electron affinity of ZrO_2 is found to be $\chi = 21.2 - 13.5 \pm 0.14 - 5.7 = 2.0 \pm 0.14$ eV where the bandgap was assumed to be 5.7 eV.

With the information gained from the XPS and UPS measurements the schematic band diagram can be constructed which now includes the 1.0 nm ZrO_2 layer (Figure 9). The band offset has been determined independently of the electron affinities and the interface dipole is found to be $\Delta = -1.43 \pm 0.29$ eV.

The field in the SiO_2 layer and the measured flat bands may seem inconsistent, however, the band bending would be at or near to the 0.1 eV experimental uncertainty. In fact, in other measurements of ZrO_2 on 0.5 nm SiO_2 on different Si substrates we have have detected band bending ~0.1 eV, but this again is at the limits of the experimental error. The results shown here are from a single experiment and are not an average of multiple data sets.

Miyazaki *et al* have published results for the system of ZrO_2–SiO_2–Si(100) which was grown by the alternative method of oxygen annealing a deposited ZrO_2 film on Si to grow a subcutaneous SiO_2 layer.[19] They have reported that this method leads to the incorporation of a few atomic percent Zr in the layer. Their published VBO with respect to Si for the subcutaneous SiO_2 is 4.35 eV, slightly lower than our measured 4.4 eV. The band offset reported for ZrO_2 on SiO_2 of 1.2 eV is larger than our result of 0.67 eV. When the method of growth is considered it is possible that the composition of the interfacial layer is different from our remote plasma grown films. The interfaces may not be as well defined and a composition gradient may exist distorting the perceived valence band offset.

5.5.3 1.0 nm Zr metal

After deposition of the Zr layer the SiO_2 related component of the Si 2p core level spectra is shifted 0.5±0.1 eV higher in binding energy. However, previously the shift after deposition of

ZrO_2 was 0.2±0.1 eV to lower binding energy. The net change is then 0.3±0.1 eV from the initial (SiO_2 buffer layer) flat band condition.

In this analysis we are assuming a stacked structure Zr–ZrO_2–SiO_2–Si where the layers are well defined and their interaction is localized at the interfaces. In keeping with this layered model the interpretation of the core level shifts must take into consideration the shifts of each underlying layer. For instance, if the Si substrate core level is shifted 0.2±0.1 eV due to band bending and the SiO_2 layer on top is shifted 0.3 eV then this is a net observed shift of the SiO_2 layer of 0.1±0.1 eV. This net shift of 0.1 eV in the SiO_2 Si 2p core level can then be used determine the total potential across the SiO_2 layer, where we find it to be 0.17±0.17 V.

To determine the potential across the ZrO_2 layer we must first consider the contribution from the band bending and the potential across the SiO_2. The band bending was determined to be 0.2±0.1 eV, and the potential across the SiO_2 layer was found to be 0.17±0.17 V, which results in a total shift due to the underlying layers of 0.37±0.19 eV. Thus, the potential across the high-κ layer is less than the experimental error of ±0.19 eV and the entire shift in the electronic structure can be ascribed to the band bending and the potentials in the underlying layers. The valence band spectrum displays emission extending to the Fermi energy, indicating metallic character. The metal work function can then be determined from the binding energy of the vacuum cut-off and the photon energy. The Zr metal work function is found to be Φ_M = 21.2 – 17.1±0.14 = 4.1±0.14 eV which is similar to other reports.[20,21]

Figure 10 presents the final band alignment as deduced for this layered structure. The interface dipole for the Zr–ZrO_2 interface is again determined from the measured work functions, electron affinities and internal potential, and a value of Δ = 1.3±0.4 eV is determined. The Si work function is 4.1 + 0.3 = 4.4 eV, which is slightly larger than the measured 4.1 eV work

function of Zr. However, the results indicate the presence of an internal field causing downward band bending in the Si, a 0.17 V potential across the SiO_2 and a potential in the ZrO_2 layer that is below our detection limits. We expect that a potential due to a work function mismatch would manifest as core level shifts in the high-k layer as well as the SiO_2, however, the magnitude of the observed shifts should scale with the relative dielectric constants meaning that the voltage drop across ZrO_2 would be perhaps a factor of 5 smaller (κ=20) than that in SiO_2. The 0.17 V potential across the SiO_2 layer would correspond with a potential across the ZrO_2 of ~0.033 V, well below our experimental sensitivity of ±0.1 eV.

5.5.4 Interface Dipoles and Band Alignment

Our findings suggest that while the electron affinity model works well for predominantly covalent materials such as SiO_2 on Si (Δ = 0.2 eV), it is not well suited for more ionic materials like ZrO_2, (e.g. the SiO_2–ZrO_2 system where Δ = -1.43 eV). Similarly the Schottky-Mott model of metal semiconductor interfaces fails to predict the ZrO_2–Zr interface band alignment the deviation Δ = -1.3 eV. Evidently, aligning vacuum levels across an interface is insufficient to predict the band alignments in the Zr–ZrO_2–SiO_2–Si system.

Robertson and Mönch have extended the metal induced gap states (MIGS) model to include semiconductor–semiconductor and semiconductor–dielectric interfaces.[22,23] They have given this generalized model the more general name of interface induced gap states (IFIGS). Rather than using the surface vacuum level as the reference level, the IFIGS model utilizes the branch point of the surface states, also termed the charge neutrality level (CNL). The model presumes that every semiconductor and insulator material will exhibit surface states that are both valence- and conduction- band-like. The CNL defines the energy at which their character

changes from valence- to conduction-band-like. The CNL is the highest occupied state in the gap, which is not unlike a Fermi level of the intrinsic gap states.

The IFIGS model suggests that charge will transfer across a metal–semiconductor interface to align the metal Fermi level and the semiconductor CNL. Similarly for a semiconductor–dielectric interface, charge will transfer and tend to align the CNLs. Another view is that the charge transfer across the interface is due to chemical bonding.[6] The charge that is transferred across these bonds establishes an interface dipole that can alter the barrier height. The polarity of the bonds can then be related to the difference in the electronegativities of the two materials in contact.

Mönch has recently combined the physical IFIGS model and the chemical electronegativity approach to approximate the valence band offset of an ideal heterostructure with:

$$\Delta E_V = \Phi^p_{bp,a} - \Phi^p_{bp,b} + D_X (X_a - X_b) \tag{6}$$

where Φ^p_{bp} is the branch-point energy of material *a* or *b* relative to the VBM. The values X_a and X_b are the corresponding electronegativities and D_X is a slope parameter determined by the density of states and the extension of the IFIGS at the branch-point. In this approach insulators are considered as wide bandgap semiconductors and Equation 6 applies equally to dielectric–dielectric interfaces.

The Schottky barrier height for a semiconductor–metal interface is given by a similar equation:

$$\Phi_{ms} = \Phi^p_{bp} - S_X (X_m - X_s) \tag{7}$$

where Φ_{bp}^{p} is the branch point energy of the semiconductor, S_X is a slope parameter and X_m and X_a are the electronegativities of the metal and semiconductor respectively. The slope parameter S_X is given by:

$$S_X = \frac{0.86}{1 + 0.1(\varepsilon_\infty - 1)^2} \tag{9}$$

where ε_∞ is the optical dielectric constant and the units of S_X are eV/Miedema electronegativity unit.

Mönch asserts that the electric-dipole term $D_X(X_a\text{-}X_b)$ from Equation 6 can be neglected because the electronegativities of atoms constituting the group-IV semiconductors and the III-V, II-VI, and I-III-IV_2 compounds only differ by up to about 10%. Thus Equation 6 reduces to simply the difference in the branch-point energies:

$$\Delta E_V = \Phi_{bp,a}^{p} - \Phi_{bp,b}^{p} \tag{8}$$

Experimental results have indicated a linear dependence of the valence-band offsets, ΔE_V, on the branch point energy Φ_{bp}^{p}. Consequently, Equation 8 has been modified with an empirical slope parameter and becomes:

$$\Delta E_V = \varphi_{VBO}\left[\Phi_{bp,a}^{p} - \Phi_{bp,b}^{p}\right] \tag{10}$$

where the slope parameter φ_{VBO} has been experimentally found to range between 1.14 and 1.23.

Contained in Table 3 are parameters for the materials of interest in this study. The Si branch-point energy is the value calculated by Tersoff while the others are from Mönch.[24,23] Using the parameters in Table 3 along with Equations 8, 9 and 10, the predicted band alignments can be determined. For comparison, the calculated and experimental results are listed in Table 4. It is important to note that the IFIGS model intrinsically accounts for the interface bonding and interface dipoles. Our approach is to compare the experimentally determined band offsets with

the prediction of the IFIGS model. The observed difference in the vacuum levels (Δ) is then presented as a correction to the electron affinity or Shottky–Mott models.

Using the Tersoff value for the Si branch-point energy (0.36 eV) and the Mönch value for SiO_2 (3.99 eV) to calculate the valence band offset we find that calculation (4.46 eV) and experiment (4.4 eV) differ by only 0.06 eV.

The branch-point energy predicted for ZrO_2 have ranged from 3.2 eV as reported by Mönch to values of 3.3 or 3.6 eV from Peacock and Robertson.[23,8,4] Taking the average of these values gives a branch point energy of 3.36 eV above E_V. Using this value with Equation 10 and the slope parameter of 1.17 as given by Mönch the calculated offset for the SiO_2–ZrO_2 interface is 0.73 eV. This is essentially consistent with the experiment al value of 0.67 eV.

To calculate the *p*-type barrier height for the ZrO_2–Zr interface Equation 7 is used along with 3.36 eV as the branch point energy and the Miedema electronegativities and slope parameter as listed in Table 3.[25] A *p*-type barrier of 4.03 eV which corresponds to an *n*-type barrier of 1.67 eV assuming a 5.7 eV bandgap for ZrO_2. The calculated value is larger than the observed conduction band barrier of 0.8 eV and we consider possible sources of the deviation from the model. The branch-point energy of 3.36 eV gave good agreement for the SiO_2–ZrO_2 interface so we presume that the value is appropriate. The slope parameter may be a source of error as its dependence on the optical dielectric constant has been empirically determined. Additionally, the optical dielectric constant from Robertson (Table 1) may be inappropriate for a ZrO_2 thin film.[4] As an exercise we calculate the slope parameter from the observed Zr–ZrO_2 Schottky barrier of 0.8 eV and find that if $S_X = 0.65$ the IFIGS model would be consistent with measurements.

It is also likely that the simplistic view of the interface, with a well defined ZrO_2 on one side and Zr on the other, is unrealistic. Taking a somewhat more complex view of the interface, one that presumes the presence of bridging oxygen, can effectively increases the electronegativity difference used to calculate the barrier height in Equation 8. This view increases the electronegativity of a ZrO_2–O cluster to 6.57 on the Miedema scale. Recalculating the Schottky barrier at the interface with a ZrO_2–O cluster on one side and Zr on the other gives a barrier of 1.04 eV, within our experimental error for the measured barrier height of ±0.44 eV. It is possible that the true source of the deviation some combination of the simplified view of the interface structure and some variation in the Schottky pinning parameter.

The intriguing point is that the large dipoles that exist at the ZrO_2 interfaces are opposite in sign and nearly equal in magnitude. The sum of the interface dipoles across the entire gate stack nearly cancel suggesting that an I-V measurement of this gate stack would show only a small dipole contribution, and the resulting flat band measurement would nearly agree with the original Schottky-Mott model.

5.6 Conclusions

In this study *in-situ* deposition and photoemission spectroscopy have been employed to characterize a potential p-MOS gate stack in a stepwise manner, determining valence band offsets, vacuum levels, internal fields and changes in band bending after each deposition step. The results from this sequential growth and characterization technique allow us to calculate, for each interface, the deviation of the electronic barrier heights as determined from the alignment of the material vacuum levels. This deviation, or interface dipole, is thought to result from charge transfer across the interface. The observed band alignment has been compared to an interface-induced gap states model as presented by Robertson and Mönch.[4,23] This model incorporates the

predicted band structure and a dipole contribution due to the chemical potential across the interface. The IFIGS model provides agreement with our results for both the Si–SiO_2 and the SiO_2–ZrO_2 interface. The discrepancy of the model and experiment for the ZrO_2–Zr interface may be attributable to a more refined value of the Schottky pinning parameter or to a more complex interface structure. Most interesting is the finding that across the completed gate stack, the sum of the interface dipoles is nearly zero, suggesting that electrical measurements would find barrier heights reasonably close to those predicted by the Schottky-Mott model and would not be sensitive to the dipoles at the individual interfaces or to the actual band alignment.

5.7 Acknowledgements

This work is supported through the Semiconductor Research Corporation, NCSU Front End Process Center, Office of Naval Research and the Air Force Office of Scientific Research.

5.8 References

[1] G. D. Wilk, R. M. Wallace, J.M. Anthony, J. Appl. Phys. **89**, 5243 (2001)

[2] J. P. Chang, Y.-S. Lin, S. Berger, A. Kepten, R. Bloom, S. Levy, J. Vac. Sci. Technol. B **19**, 2137 (2001)

[3] E. P. Gusev, E. Cartier, D. A. Buchanan, M. Gribelyuk, M. Copel, H. Okorn-Schmidt, C. D'Emic, Microelec. Eng. **59**, 341 (2001)

[4] J. Robertson, J. Vac. Sci. Technol. B **18**,1785, (2000)

[5] Semiconductor Industry Association, *International Technology Roadmap for Semiconductors*, 2003 ed. (SEMATECH, 2003)

[6] C.B. Duke, C. Mailhiot, J. Vac. Sci. Technol. B **3**, 1170 (1985)

[7] J. Bardeen, Phys. Rev. **71**, 717 (1947)

[8] P.W. Peacock, J. Robertson, J. Appl. Phys. **92**, 4712 (2002)

[9] W. Mönch, J. Appl. Phys. **80**, 5076, (1996)

[10] A. Fissel, J. Dabrowski, and H.J. Osten, J. Appl. Phys. **91**, 8986, (2002)

[11] C. C. Fulton, G. Lucovsky, R. J. Nemanich, Appl. Phys. Lett. **84**, 580 (2004)

[12] J.R. Shallenberger, D.A. Cole, Proceedings of 12th Conference on Ion Implantation Technology, (1998)

[13] M.P. Seah, W.A. Dench, Surf. Interface. Anal. **1**, 2 (1979)

[14] J.C. Ashley, C.J, Tung, Surf. Interface. Anal. **4**, 52 (1982)

[15] C. Fulton, G. Lucovsky, R. J. Nemanich, J. Vac. Sci. Technol. B. **20**, 1726 (2002)

[16] A. C. Tuan, T. C. Kaspar, T. Droubay, J. W. Rogers Jr., S. A. Chambers, Appl. Phys. Lett. **83**, 3734 (2003)

[17] J.W. Keister, J.E. Rowe, J.J Kolodziej, H. Niimi, T.E. Madey, G. Lucovsky, J. Vac. Sci. Technol. B **17**, 1831 (1999)

[18] S.M. Sze, *VLSI Technology*, 2nd ed. (McGraw-Hill Book Co. New York, 1988)

[19] S. Miyazaki, M. Narasaki, M. Ogasawara, M. Hirose, Sol. Stat. Elec. **46**, 1679 (2002)

[20] H. B. Michaelson, IBM J. Res. Dev. **22**, 72 (1978)

[21] V. Misra, G.P. Heuss, H. Zhong, Appl. Phys. Lett. **78**, 4166 (2001)

[22] J. Robertson, Eur. Phys. J. Appl. Phys. **28**, 265, (2004)

[23] W. Mönch, Appl. Phys. Lett. **86**, 122101, (2005)

[24] J. Tersoff, Surf. Sci. 168, **275** (1986)

[25] A.R. Miedema, P.F. de Chatel, F.R. de Boer, Physica B. **100**, 1 (1980)

Table 5.1: Tabulated x-ray and ultraviolet photoemission features after each deposition step. Values are in binding energy (eV) relative to the Si E_F with an error of ±0.1 eV.

Process Step	*0.5 nm SiO_2*	*1.0 nm ZrO_2*	*1.0 nm Zr*
Si 2p (Bulk)	99.6	99.6	99.8
Si 2p (SiO_2)	103.3	103.1	103.6
Zr 3d (ZrO_2)	n/a	183.0	183.3
Zr 3d (metal)	n/a	n/a	179.4
VBM	5.2	4.2	0.0
$\mathbf{E_{Vac}}$	16.6	17.7	17.1

Table 5.2: Tabulated electronic structure for the Si–SiO_2–ZrO_2–Zr system including band bending, internal potentials, VBOs, electron affinities and interface dipoles. The VBO includes band bending and internal fields. The conduction band offset (CBO) assumes a bandgap (9.0 eV for SiO_2 and 5.7 eV for ZrO_2).

Process Step	0.5 nm SiO_2	1.0 nm ZrO_2	1.0 nm Zr
Band Bending	0.0±0.1	0.0±0.1	0.2±0.1
Potential (SiO_2)	n/a	-0.33±0.17	0.17±0.17
Potential (ZrO_2)	n/a	n/a	0.0±0.1
VBO (wrt Si)	4.4±0.1	3.73±0.19	n/a
CBO (wrt Si)	3.5±0.1	0.87±0.19	n/a
χ / Φ_M	0.8±0.14	2.0±0.14	4.1±0.14
Dipole (Δ)	0.2±0.14	-1.43±0.29	1.3±0.39

Table 5.3: Tabulated values of the bandgap, slope parameter φ_{VBO}, the branch point energy Φ_{bp}, the Miedema electronegativity X, the optical dielectric constant ε_∞, and the calculated slope parameter S_X.

Material	E_G (eV)	φ_{VBO}[a]	Φ_{bp} (eV)	X (Miedema)[c]	ε_∞[d]	S_X (eV/Miedema)
Si	1.1	n/a	0.36[b]	4.70	12	n/a
SiO_2	9.0	1.23	3.99	6.42	2.25	0.74
ZrO_2	5.7	1.17	3.36	5.76	4.80	0.35
Zr	n/a	n/a	n/a	3.40	n/a	n/a

[a]See Ref 23
[b]See Ref 24
[c]See Ref 25
[d]See Ref 4

Table 5.4: Calculated barrier heights from the IFIGS model, the electron affinity (Schottky–Mott) model and a comparison with measured values. CBO values presume bandgaps as listed in Table 3.

Interface	*IFIGS VBO*	*EA/S-M VBO*	*Measured VBO*	*IFIGS CBO*	*EA/S-M CBO*	*Measured CBO*
Si–SiO_2	4.46	4.6	4.4±0.1	3.44	3.3	3.5±0.1
SiO_2–ZrO_2	0.73	2.1	0.67±0.24	2.57	1.2	2.63±0.24
ZrO_2–Zr	4.03	3.6	4.90±0.44	1.67	2.1	0.80±0.44

Figure Captions

Figure 5.1:
The Si 2p XPS core level spectra of 0.5 nm SiO_2 on n-Si (100). The feature at 99.6 eV shows Si-Si bonding that is attributed to Si in the substrate and the feature at 103.3 eV is attributed to Si-O bonding in SiO_2.

Figure 5.2:
The UPS valence band spectrum of 0.5 nm SiO_2 on n-Si. The VBM (5.2 eV) and the cut-off due to the vacuum level (16.6 eV) are indicated.

Figure 5.3:
The Si 2p XPS core level spectra before (grey) and after (black) deposition of 1.0 nm ZrO_2. After deposition the substrate related peak is unchanged and the oxide related peak is shifted 0.2 eV lower in binding energy.

Figure 5.4:
The UPS valence band spectrum of 1.0 nm ZrO_2. The VBM (4.2 eV) and the vacuum level (17.7 eV) are indicated.

Figure 5.5:
The Si 2p XPS core level spectra before (grey) and after (black) deposition of 1.0 nm of Zr. After deposition the substrate related peak is shifted 0.2 eV higher in binding energy and the oxide related peak is shifted 0.5 eV lower in binding energy.

Figure 5.6:
The Zr 3d XPS core level spectra before (grey) and after (black) deposition of 1.0 nm Zr metal. After deposition the oxide related 3d 5/2 peak is shifted 0.3 eV higher in binding energy.

Figure 5.7:
The UPS valence band spectrum after deposition of 1.0 nm of Zr on ZrO_2. The emission extends to the Fermi level indicating metallic character and the vacuum cut-off is observed at 17.1 eV.

Figure 5.8:
A schematic band diagram for 0.5nm SiO_2 on n-Si. The band offsets and electron affinities are indicated and an interface dipole of $\Delta = 0.2$ eV is deduced.

Figure 5.9:
A schematic band diagram for 1.0 nm ZrO_2 on 0.5nm SiO_2 on n-Si. The band offsets and electron affinities are indicated as are interface dipoles and a field in the SiO_2 layer.

Figure 5.10:
A schematic band diagram for 1.0 nm Zr metal on 1.0 nm ZrO_2 on 0.5nm SiO_2 on n-Si. The Zr work function of 4.1 eV, the oxide electron affinities and the dipoles at each interface are indicated. Below is the balanced equation for the difference in the Si and Zr work functions

including the dipole contribution from each interface and the potential across the dielectric layers.

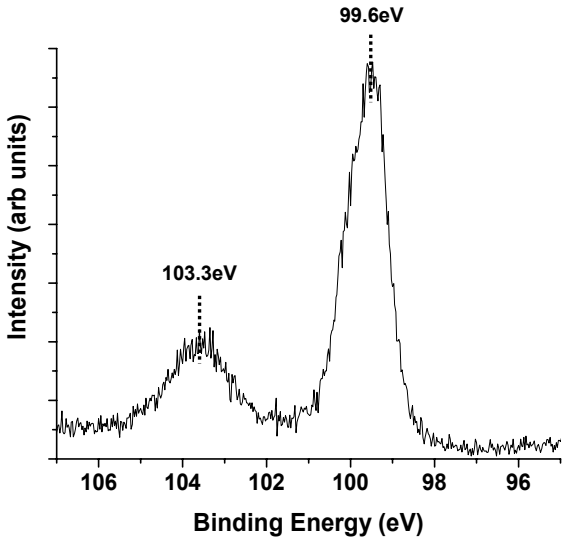

Figure 5.1: The Si 2p XPS core level spectra of 0.5 nm SiO_2 on n-Si (100). The feature at 99.6 eV shows Si-Si bonding that is attributed to Si in the substrate and the feature at 103.3 eV is attributed to Si-O bonding in SiO_2.

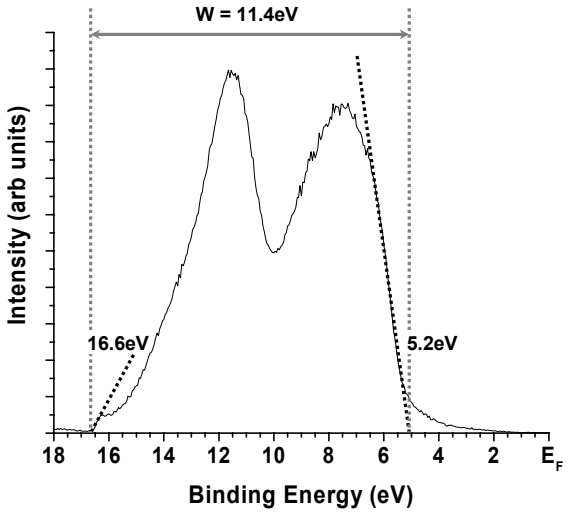

Figure 5.2: The UPS valence band spectrum of 0.5 nm SiO_2 on n-Si. The VBM (5.2 eV) and the cut-off due to the vacuum level (16.6 eV) are indicated.

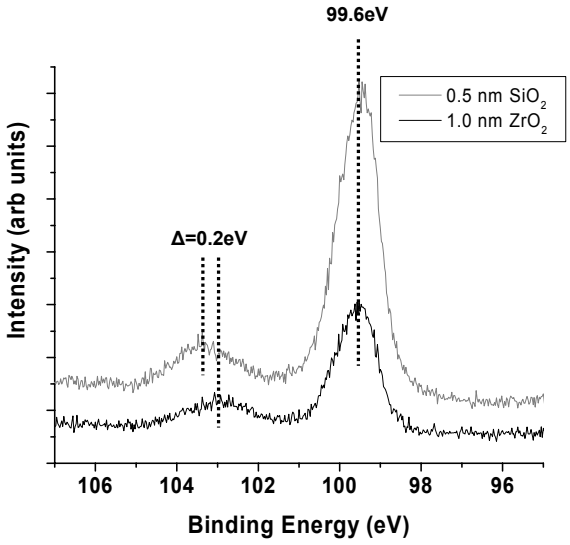

Figure 5.3: The Si 2p XPS core level spectra before (grey) and after (black) deposition of 1.0 nm ZrO_2. After deposition the substrate related peak is unchanged and the oxide related peak is shifted 0.2 eV lower in binding energy.

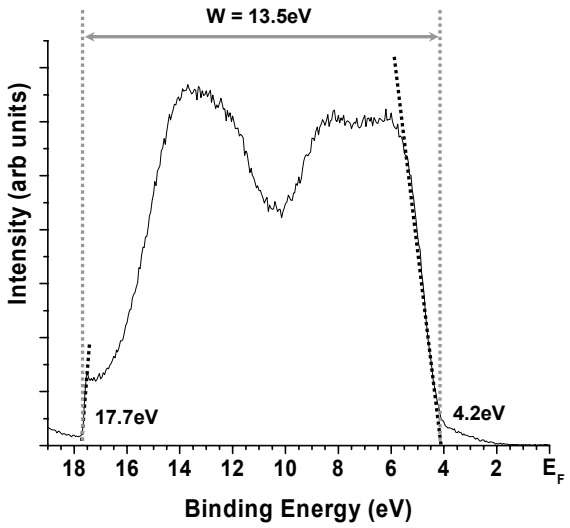

Figure 5.4: The UPS valence band spectrum of 1.0 nm ZrO2. The VBM (4.2 eV) and the vacuum level (17.7 eV) are indicated.

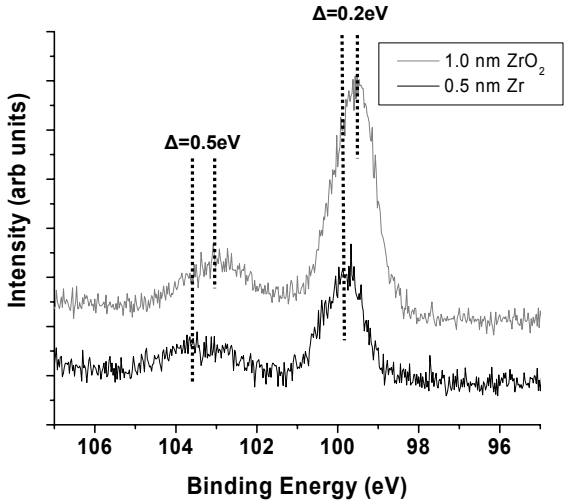

Figure 5.5: The Si 2p XPS core level spectra before (grey) and after (black) deposition of 1.0 nm of Zr. After deposition the substrate related peak is shifted 0.2 eV higher in binding energy and the oxide related peak is shifted 0.5 eV lower in binding energy.

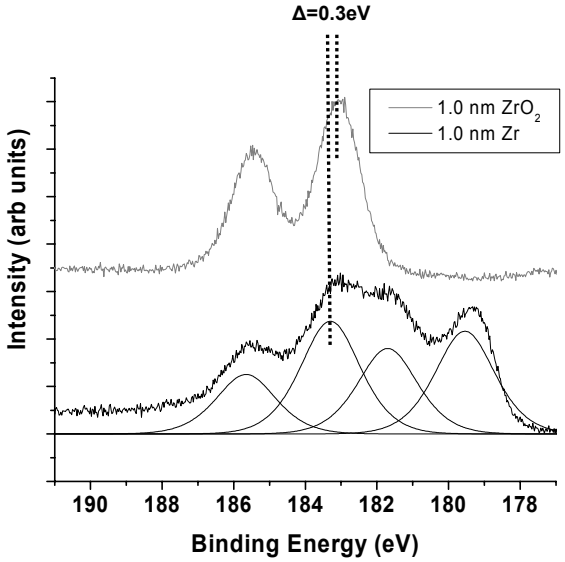

Figure 5.6: The Zr 3d XPS core level spectra before (grey) and after (black) deposition of 1.0 nm Zr metal. After deposition the oxide related 3d 5/2 peak is shifted 0.3 eV higher in binding energy.

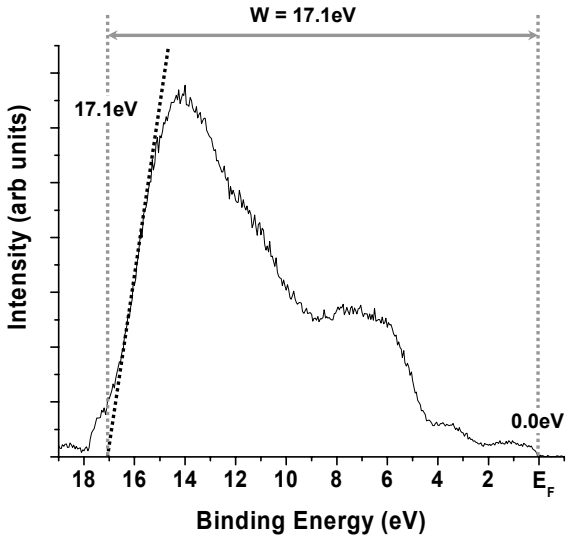

Figure 5.7: The UPS valence band spectrum after deposition of 1.0 nm of Zr on ZrO_2. The emission extends to the Fermi level indicating metallic character and the vacuum cut-off is observed at 17.1 eV.

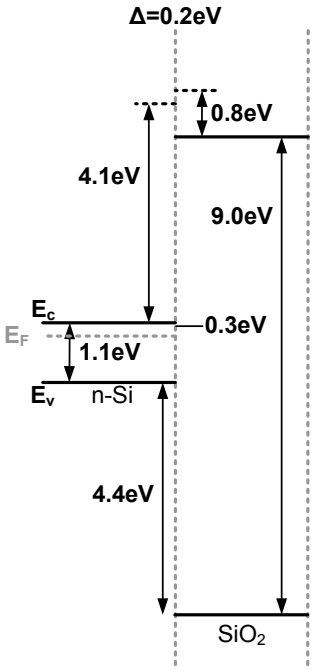

Figure 5.8: A schematic band diagram for 0.5nm SiO_2 on n-Si. The band offsets and electron affinities are indicated and an interface dipole of $\Delta = 0.2$ eV is deduced.

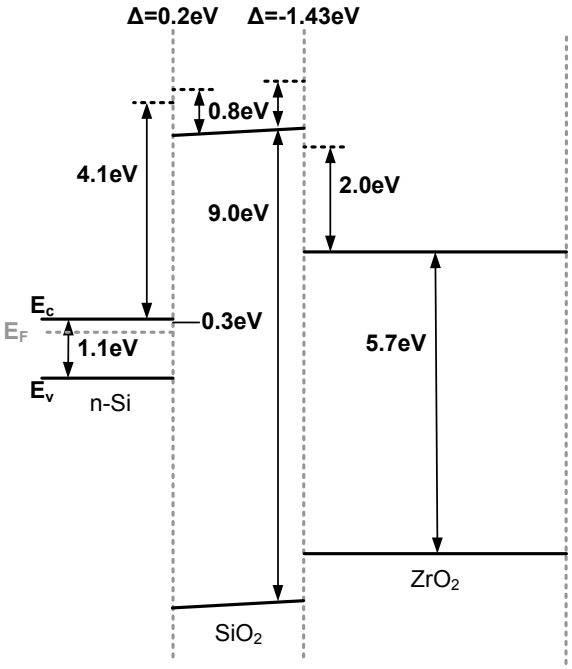

Figure 5.9: A schematic band diagram for 1.0 nm ZrO_2 on 0.5nm SiO_2 on n-Si. The band offsets and electron affinities are indicated as are interface dipoles and a field in the SiO_2 layer.

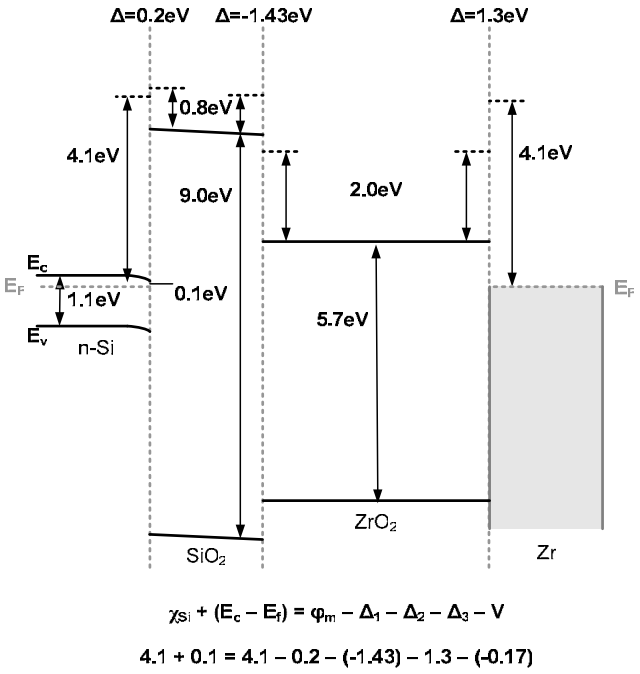

Figure 5.10: A schematic band diagram for 1.0 nm Zr metal on 1.0 nm ZrO_2 on 0.5nm SiO_2 on n-Si. The Zr work function of 4.1 eV, the oxide electron affinities and the dipoles at each interface are indicated. Below is the balanced equation for the difference in the Si and Zr work functions including the dipole contribution from each interface and the potential across the dielectric layers.

6. Summary and Future Work

C.C. Fulton
Department of Materials Science and Engineering
North Carolina State University
Raleigh, North Carolina 27695-7907

6. Summary and Future Work

6.1 Summary

Thermally grown silicon oxide, SiO_2, has enabled much of the metal–oxide–semiconductor (MOS) technology that is ubiquitous in today's world. This amorphous oxide has been a staple of the semiconductor industry for many years and, while the devices have become orders of magnitude smaller and faster over the last 40 years, the materials used to make those devices are relatively unchanged. Typically the dimensions of logic devices are reduced to improve performance, but as the physical dimensions shrink—in particular the thickness of the gate dielectric—quantum mechanical tunneling becomes a significant problem. A possible solution to this would be to replace the gate dielectric (typically SiO_2) with some other material with a larger relative permittivity, but the task of identifying a suitable replacement dielectric for high-performance, low-power devices is a complex one. Transition-metal oxides—Zr and Hf in particular—have received much attention because of their large dielectric constants and relatively large bandgaps.

It is also desirable to replace the heavily doped poly-Si with a metal as the gate material because, while poly-Si can be appropriately doped for both *n*- and *p*-type devices, it still requires some finite depletion width to terminate a field applied to the device gate. This depletion width contributes to the total effective oxide thickness in a device, and replacing the poly-Si with a metal with zero depletion width becomes necessary for aggressively scaled devices. Any metal to be used as a gate material must be chemically stable and have a low defect density when in contact with a TM oxide. Additionally, the metal and its characteristic work function must be chosen appropriately for *n*- and *p*-type devices. Thus, the integration of high-κ gate stacks into a device is a much more complex process than that

for a thermal oxide or even a deposited oxynitride. Understanding barrier heights and the interface chemistry that influences them is critical for choosing a suitable replacement dielectric.

Photoemission spectroscopy has been used to address the interface stability of ZrO_2 with respect to a Si substrate. We have addressed three issues: 1) the development of the band offsets and electronic structure during the low temperature (T<300°C) growth processes, 2) variations in the band structure as effected by process conditions and annealing (T<700°C) and 3) the interface stability of Zr oxide films at high temperatures (T>700°C). Annealing the as-grown films to 600°C results in a ~2 eV shift of the ZrO_2–Si band alignment, resulting in a band offset that is favorable to devices and in agreement with predictions and with other experiments. We have proposed that the as-grown films contain excess oxygen resulting in a charge transfer from the Si substrate to the internal (ZrO_2–SiO_2) interface and that annealing to 600°C is sufficient to drive off this oxygen. Further annealing to 900°C, in the presence of excess Si at the surface, results in decomposition of the oxide to form $ZrSi_2$.

We then expanded on the low temperature instability noted earlier in the study of ZrO_2 on Si. Titanium, zirconium and hafnium oxides were deposited on ultra-thin (~0.5 nm) SiO_2 buffer layers and metastable states have been identified which give rise to large changes in the band alignments with respect to the Si substrate. This results in a potential across the interfacial SiO_2 layer, significant band bending and large shifts of the high-κ valence band. The magnitude of the shift differs for the three materials and is dependant on both the SiO_2 buffer layer thickness and annealing temperature. We have proposed a model where the magnitude of the observed shift is related to the oxygen solubility in the high-κ materials and

where excess oxygen accumulates near the high-κ–SiO_2 interface providing electronic states that are available to electrons that tunnel from the substrate.

Also discussed is the band edge electronic structure of 1) nanocrystalline elemental and complex oxide high-κ dielectrics, and 2) non-crystalline Zr and Hf silicates and Si oxynitride alloys. The experimental approach includes X-ray absorption spectroscopy, photoconductivity, and visible/vacuum ultra-violet and spectroscopic ellipsometry (SE). These measurements are complemented by Fourier transform infra-red absorption, x-ray photoelectron spectroscopy, high resolution transmission electron microscopy, and x-ray diffraction. Three issues are highlighted: Jahn-Teller term-splittings that remove band edge d-state degeneracies in nanocrystalline films, intrinsic bonding defects in ZrO_2 and HfO_2, and chemical phase separation and crystallinity in Zr and Hf silicate and Si oxynitride alloys.

Finally, we have characterized the electronic properties of a candidate gate stack including electron affinities and work functions, valence band maxima, band bending in the Si and fields in the oxide layers. With this information the band offsets can be constructed and also determine the deviation from the Schottky-Mott (or electron affinity) model at each interface. These models presume that the conduction band alignment is determined from aligning the vacuum levels of two materials. Interface bonding and defect states can contribute to charge transfer across the interface, forming a dipole and altering the barrier heights. Independently measuring band offsets and vacuum levels allows the deviation from these vacuum level models to be determined. That deviation can then be presented as an additional constant, Δ, the interface dipole, and discuss this dipole in terms of likely interface bonding.

6.2 Future Work

Photoelectron spectroscopy is a powerful technique for investigating both the chemical and electronic properties of surfaces and interfaces. This work has been a systematic study of the interface properties of high-κ dielectric and metal gate materials which have been deposited *in-situ* to form structures that approximate a device gate stack.

The analysis, outlined in Chapter 5, for determining the interface dipoles should be applied to other dielectric-metal combinations. A larger data set that includes high and low work function metals could improve the understanding of interfacial chemistry and how it can influence the electronic structure of a gate stack. In particular, less reactive, high work function metals should be studied where the charge transfer across the interface bonds should be lower. It would be helpful to include studies not only on high-κ dielectrics but also on SiO_2 films. Along with the spectroscopy results, comparing the effective barrier heights as measured by C-V curves could prove especially helpful in understanding the behavior of these systems and whether observed charges are bulk- or interface-related.

The model used to understand the interface electronic structure predicts the observed band alignment for both the Si–SiO_2 and the SiO_2–ZrO_2 interface but deviates significantly for the ZrO_2–Zr interface. The presented view of the interface is a simplistic one, that only considers the charge transfer in the first layer of atoms on either side of an interface. This model could be refined to give a more realistic prediction of the interface dipoles.

The work on alloy oxide films as begun in Chapter 4 should be continued to further understand the role of the Jahn-Teller split states and how they effect electrical characteristics in MOS devices. Preliminary measurements have been completed to characterize the O vacancy state in the ZrO_2–Y_2O_3 alloys. Understanding the fundamental

issues may allow an engineered gate stack to achieve the desired performance gains. From a technological view, the SiO_2–Si_3N_4–ZrO_2 system is interesting as it appears some compositions can inhibit phase separation. Again, applying the analysis as in Chapter 5 may prove interesting for this system.